Catastrophic Optical Damage in High-Power AlGaInP Diode Lasers

Von der Fakultät für Ingenieurwissenschaften der

Universität Duisburg-Essen

UNIVERSITÄT
DUISBURG
ESSEN

zur Erlangung des akademischen Grades eines

Doktors der Ingenieurwissenschaften

Doktor-Ingenieur (Dr.-Ing.)

genehmigte Dissertation

von

Marwan BOU SANAYEH

aus dem Libanon

Acknowledgment

Table of Contents

Chapter 1

Introduction

Laser diodes have many advantages over other types of lasers in terms of cost, size, efficiency, reliability, range of available wavelengths, and tunability. More than two decades have passed since the first continuous wave (cw) operation in red-emitting lasers was observed in laboratories **[1][2]**. Since then, AlGaInP red-emitting lasers have been in continuous development. Nowadays, red lasers are being used in several commercial applications, such as printing technologies, laser displays, disk recorders, and medical therapies.

The first visible AlGaInP lasers emitted light around 670 nm **[1]**. Especially in disk recording, the reduced wavelength reduces the spot size and increases the recording density of optical disc memories by 1.5 times compared with conventional IR-emitting AlGaAs lasers. Another recent application is photodynamic therapy (PDT) for localized cancer treatment. The PDT procedure usually has fewer undesirable side-effects than chemotherapy, potentially offering cancer patient a greater chance for recovery and better quality of life during treatment **[3]**.
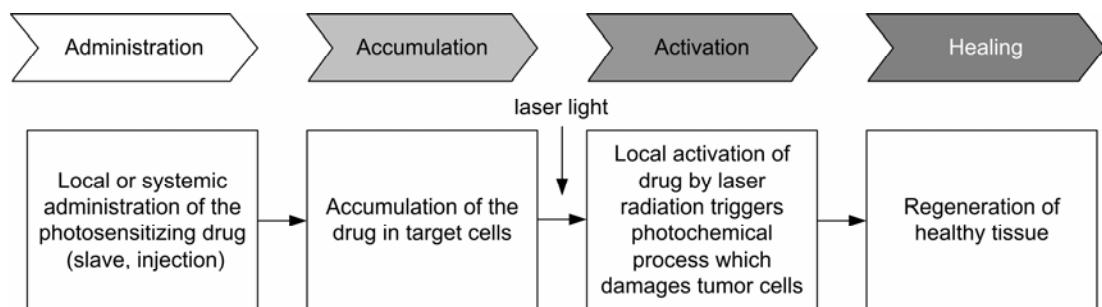
Fig.1.1.1. Treatment sequence of photodynamic therapy [3].

PDT utilizes the combined action of light and photosensitizing drug, as shown in Fig. 1.1.1. In PDT, the red wavelength presents the advantage of increased penetration depth in tissue compared to wavelengths of most commonly available lasers for clinical studies. In addition, several new photosensitizers have an absorption band between 630 nm and 690 nm. Hence, the development of high-power red diode lasers provides a cost effective alternative to existing lasers for use in PDT [3].
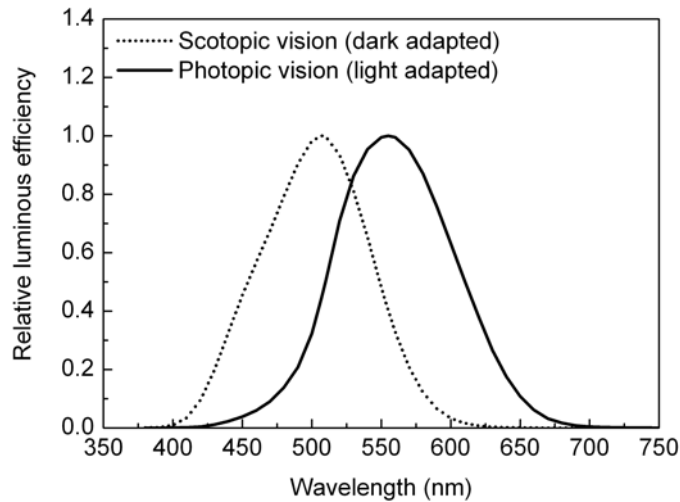
Fig.1.1.2. CIE spectral luminous efficiency functions for scotopic and photopic vision [4].

AlGaInP lasers operating at a wavelength above 650 nm usually have better efficiency then lasers operating below it. Nevertheless, around 630 nm, the sensitivity of the human eye is about a factor of eight greater than that near 670 nm. Figure 1.1.2 displays the International Commission on Illumination (CIE) spectral luminous efficiency functions of scotopic (dark adapted) and photopic (light adapted) vision [4]. This high visibility may be an important safety aspect, for instance for use in hand-held devices [5]. More interestingly, short-wavelength AlGaInP lasers offer a better potential in new applications that require red emission, like in laser projection, where the red color is essential to complete the RGB spectrum. Due to the decreased human eye sensitivity with increasing wavelength in the red spectral range, the longer the wavelength the more power is required to reach the same luminous efficiency. This becomes important when such projectors are to be integrated in pocket devices, such as mobile phones, PDAs, etc., where battery lifetime is a critical issue.

1.1 Motivation

Semiconductor lasers are basically made of a gain section between two facets. When a laser is driven into higher output powers, the facet regions absorb light, hence making the facets hot, and provoking a "thermal runaway" system and eventually irreversible laser destruction. This effect is called catastrophic optical damage (COD) and it is characterized by a sudden drop in the output power at a certain maximum injection current.

COD causes a serious reliability problem in AlGaInP lasers and is the ultimate limiting effect for high-power applications. The use of such lasers in sensitive applications like photodynamic therapy demands outstanding high-power performance and long-term reliability of many thousand hours. In the past two decades, several studies have been performed to improve the COD level in different laser material, especially in IR-emitters, such as AlGaAs, InGaAsP/InGaP, and Al-free InGaAs/InGaP. Recent developments include proper facet passivation to reduce surface oxidation [6], quantum-well intermixing near the facets to decrease absorption there [7][8], and current-blocking to reduce surface recombination at the mirrors [9][10]. In addition, it has been revealed by electroluminescence [11], electron beam induced current (EBIC) [12], and especially transmission electron microscopy (TEM) [11]-[14] that during COD, dark line defects (DLDs) develop from the output facet into the laser as dislocations and dislocation networks. The first analysis by Henry et al. [13] demonstrated that COD is due to local melting caused by excessive heating as a result of nonradiative recombination, and that <110>DLDs result from the propagation of a molten zone confined to the active region. Similarly, Ueda [14] explained it as caused by strong optical absorption at the facet or at intrinsic crystal defects, subsequent melting of the crystal, and propagation of the molten region into the laser during operation leaving a re-crystallized region after cooling. Only a decade later, Park et al. [11] were able with high-resolution TEM analysis to determine the nature of the DLDs in Al-free InGaAs/InGaP double quantum well 980 nm lasers as having a highly nonradiative polycrystalline nature. However, the dynamics of the COD effect were never analyzed in detail. On top of that, COD in AlGaInP lasers has hardly been researched in the past [15].

The increasing importance of extracting more and more power out of AlGaInP lasers has not only driven the need to improve all their characteristics, but also triggered the desire to better understand the causes behind their failure modes. In this thesis, a complete study of the COD effect in AlGaInP lasers including the investigation of its induced defects and the analysis of its temperature dynamics is presented. Moreover, based on those analyses, possible solutions for COD level improvement are discussed.

1.2 Thesis overview

The first half of chapter 2 introduces the properties and design of the AlGaInP lasers used in this study, including the basics of the AlGaInP material system, AlGaInP laser structure and epitaxy design, facet coating, and laser mounting techniques. In the second half of this chapter, the basic laser relations and characterization are presented. This includes the electro-optical characterization, temperature dependence, thermal resistance, spatial emission and internal parameters extraction.

In chapter 3, the degradation and aging mechanisms in high-power AlGaInP lasers are introduced. First, the fabrication of a high-power laser lifetime testing facility which was used to study those mechanisms, including the COD effect, is presented. Moreover, the influence of the most important degradation parameters on aging is discussed in this chapter.

Chapter 4 presents the investigation of dark line defects induced by COD in AlGaInP high-power lasers. The localization of the defects inside the resonator by micro-photoluminescence mapping and focused ion beam microscopy analysis is demonstrated. Results from different high-power laser designs, including, broad-area lasers, laser bars, and tapered lasers are compared.

In chapter 5, the COD temperature dynamics are analyzed. Micro-Raman spectroscopy and real-time thermal imaging are used for this purpose. Moreover, temperature-power analysis and an introduction to the critical temperature approach complement those analyses.

Chapter 6 discusses the influence of design parameters and possible solutions to improve the COD level in AlGaInP lasers. First, the influence of chip design on COD is presented. Second, the importance of facet passivation and its effect on COD is demonstrated. Finally, low-absorption facets design techniques for COD improvement including current-blocking near the facet regions and non-absorbing mirrors by quantum well intermixing are described.

To conclude, the results of this study are summarized in chapter 7.

Chapter 2

AlGaInP laser properties and design

AlGaInP was shown to be the most suitable material candidate for lasers operating in the red spectral range. For the AlGaInP material system, which is latticed matched to GaAs, metalorganic vapor-phase epitaxy (MOVPE) is the dominant crystal growth technique used for the fabrication of high-quality lasers [16]. In this chapter, the basic principles of the AlGaInP system are reviewed. Moreover, an introduction to the different commercial laser design structures used in this study is presented. Some fabrication parameters for low- and high-power operation are also discussed. Finally, the AlGaInP laser characterization methodology is described.

2.1 The AlGaInP material system

Three decades have passed since the AlGaInP system was first discussed in 1978 [17]. The ternary $In_yGa_{1-y}P$ system has a direct energy gap over most of its composition range. At y ~ 0.48, the material is latticed matched to GaAs (lattice constant = 5.653 Å), which is therefore the preferred substrate. In the case of these covalent semiconductors, the substitution of Ga by Al hardly produces any change of the lattice constant, as is also observed in the AlGaAs system [5]. Hence, with the indium constant fixed at around 0.48, Ga may partially be replaced by Al to provide various bandgaps within the $(Al_xGa_{1-x})_{0.52}In_{0.48}P$ system, while maintaining a fixed lattice constant that matches the GaAs substrate.

The bandgap energies of the $(Al_xGa_{1-x})_{0.5}In_{0.5}P$ system have been determined by various methods [18], yielding slightly different results. A commonly accepted relation at room temperature is $E_{g\Gamma} = (1.900 + 0.61x)\,\text{eV}$ and $E_{gX} = (2.204 + 0.085x)\,\text{eV}$

for the direct and indirect bandgaps variation with composition, respectively **[19]**. These values indicate that the Γ-X crossover takes place for x = 0.58, corresponding to an energy of 2.25 eV or a wavelength of 550 nm, as illustrated in Fig. 2.1.1.
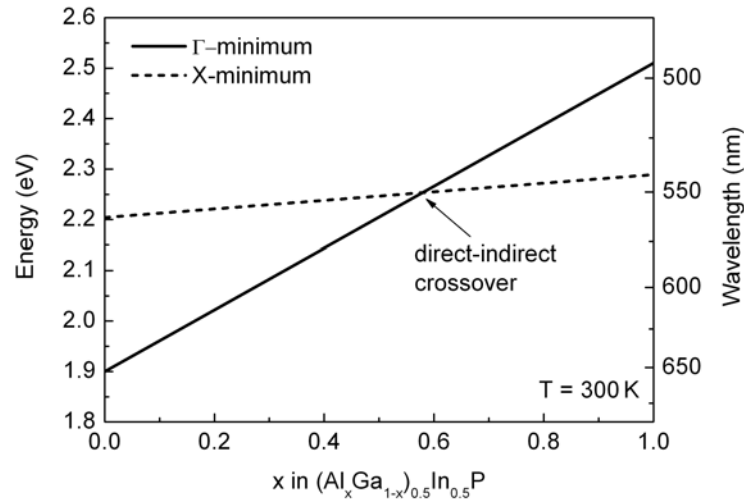
Fig. 2.1.1. Bandgap energy vs. alloy composition x at room temperature for the Γ and X bands of $(Al_xGa_{1-x})_{0.5}In_{0.5}P$ according to [18].
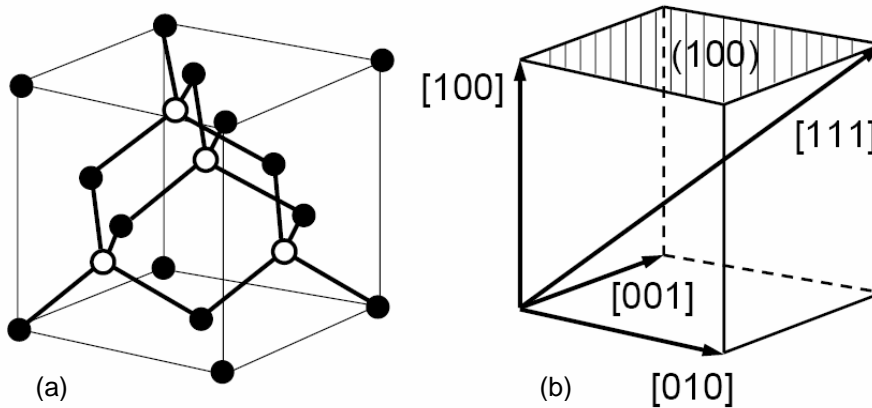
Fig. 2.1.2. (a) Cubic unit cell of the zinc blend structure. The open spheres represent group III atoms (In, Al, Ga) and the full spheres group V atoms (P). The lines represent the tetrahedral bonds between atoms of the unit cell. (b) The Miller indices for various directions in the cubic lattice [20].

Like most other III-V semiconductor materials, AlGaInP crystallizes into a cubic zinc blend structure as shown in Fig. 2.1.2. However, an important property of the InGaP and AlGaInP material systems is ordering. Due to the different covalent radii of Ga and In, there is a driving force for an arrangement of these atoms that deviates from a random distribution on the group-III lattice. This arrangement is known as the $CuPt_B$ ordering and leads to alternating preferential occupation of (111)B planes by Ga and In **[21]**.

Whether the material will be ordered or not depends essentially on the MOVPE growth conditions and the orientation of the substrate. Many groups use misoriented substrates to disorder the material. Other experiments also showed that to reduce the effect of ordering, and also the tendency of oxygen incorporation, growing at high temperatures of around 750 °C can be helpful [21]. Figure 2.1.3 shows transmission electron microscopy (TEM) images of an ordered vs. a disordered AlGaInP material. The disordering was achieved by substrate misorientation.
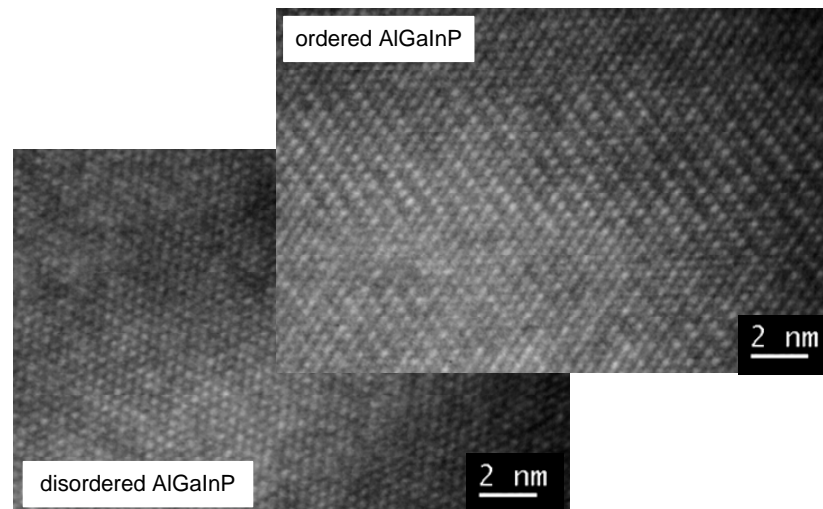
Fig. 2.1.3. TEM images of an ordered vs. disordered AlGaInP material. In the ordered material, the Ga and In order themselves in one crystal line direction.

Using disordered AlGaInP material for semiconductor lasers presents the advantage that lasers emitting at shorter wavelengths are more easily obtained by using disordered material. This is due to the fact that the bandgap of ordered material is smaller compared to the disordered one [22]. Moreover, due to this reason, it is important in AlGaInP lasers to have disordered barriers, so that the bandgap difference between them and the QWs is as high as possible, in order to reduce the carrier leakage. Carrier leakage presents a real reliability problem in AlGaInP devices and will be discussed in the next sections and chapters. On the other hand, a disadvantage of the use of substrate misorientation is that the orientation dependence of the wet-chemical etching processes used, e.g. for ridge etching, will generally lead to a lateral asymmetry of the waveguide, which has an adverse effect on the electro-optical properties of the lasers, especially at high output powers [5]. So care should be taken when processing lasers with misoriented substrates.

2.2 AlGaInP laser structure

2.2.1 Epitaxy
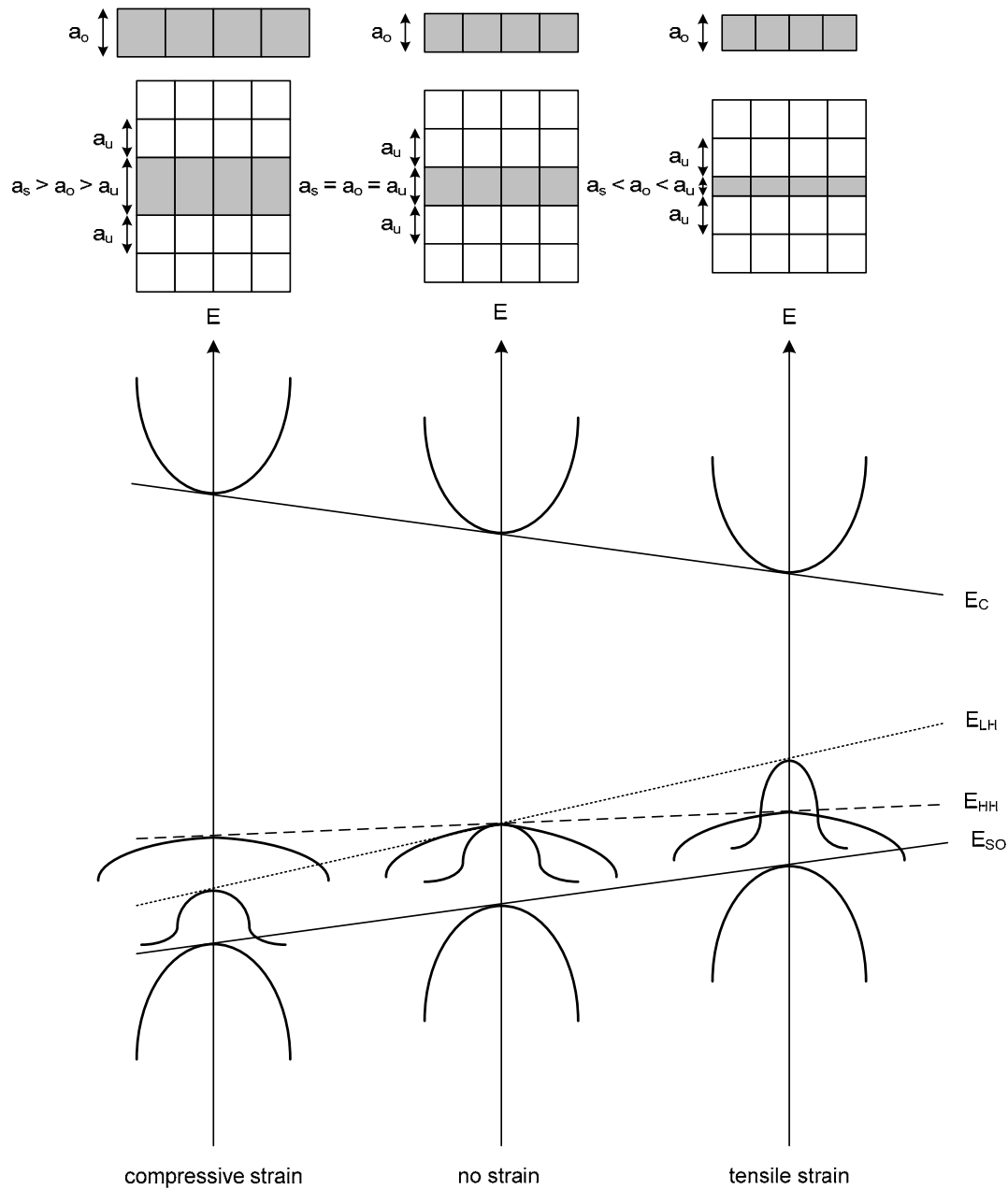
Fig. 2.2.1. Qualitative band energy shifts of the conduction band and three valence bands for biaxial compressive and tensile strain in III-V compound semiconductors. For each case, an illustration of the crystal lattice deformation resulting from the epitaxial growth of a thin layer of material with native lattice constant a_o between two thick layers with lattice constant a_u. Notations: E_C = conduction band, E_{LH} = light-hole band, E_{HH} = heavy-hole band, E_{SO} = split-off band. a_s/a_u: strained/unstrained layer lattice constant [25].

Nowadays, almost all semiconductor lasers are quantum well (QW) lasers. While most of the layers within the heterostructure are lattice matched to the underlying substrate, the active, light-emitting layer usually consist of a single or multiple strained QW structure. In multiple QWs, the net strain accumulates, reducing the maximum allowable strain per single QW. AlGaInP-based devices in particular often use stacks of several QWs to obtain better temperature characteristics [23]. However, the laser threshold in general increases with increasing number of QWs.

The introduction of strain in a typical zinc-blend-type semiconductor splits the degeneracy at the valence band maximum, and separates the heavy-hole (HH) and light-hole (LH) subbands as schematically depicted in Fig. 2.2.1. The lifted degeneracy leads to preferential polarization of the emitted light. For tensile strain, transitions involving the light-holes have the lowest energy leading to TM polarization; for compressive strain, transitions between electrons and heavy-holes lead to TE polarization. In strained layers, the change in the band structure leads to a reduction of the density of states at the edge of the valence band and also the effective mass of electrons and holes, hence resulting in a considerable reduction of threshold current compared to unstrained lasers. The threshold current reduction effect in strained InGaP QWs has already been demonstrated in 1992 by A. Vlaster [24]. Due to those positive effects, strain is nowadays introduced even if the same emission wavelength is, in principle, attainable using unstrained material [21].

For AlGaInP lasers, depending on the desired peak wavelength emission, the InGaP active layer of the lasers is either tensile or compressively strained. Strained layers with a reasonable amount of strain always have thicknesses in the quantum well regime ($\lesssim 10\,\text{nm}$). Strain is defined as $\varepsilon = \dfrac{(a_u - a_s)}{a_u}$, where a_u and a_s are the unstrained and strained lattice constants respectively [25]. Usually, strained layers are designed according to the critical thickness rules defined as the product of strain and the strained layer thickness d_s as $\varepsilon d_s \leq 100 - 200\,\%\text{Å}$, where ε is in % and d_s in Å [5]. This limit is imposed by the necessity of preventing the occurrence of misfit dislocations. In AlGaInP lasers, compressive strain is usually used for long emission wavelengths ($\gtrsim 640\,\text{nm}$) by increasing the In content in the InGaP QW layers. Typical strain values are of the order of 0.5 to 1%. For short emission wavelengths, compressively strained QWs cannot be realized anymore without some disadvantages. Moving to shorter wavelengths and keeping the compressive strain means that the InGaP QWs should become relatively thin. At some point, they reach a limit where the laser's reliability and performance deteriorates due to inhomogeneous broadening along the layer and to a large decrease in the confinement factor. This is why for AlGaInP lasers with emission wavelengths around 630 nm, the InGaP QW layers are grown with tensile strain (TM polarized) by increasing the amount of Ga.

Another solution to shift the wavelength is to grow quaternary AlGaInP QWs instead of ternary strained InGaP QWs, where the wavelength can be controlled by changing the Al content. The introduction of Al, however, can lead to increased oxygen incorporation and stronger aging of the devices.

2.2.2 Layer structure

A standard epitaxy structure of an AlGaInP laser is schematically shown in Fig. 2.2.2. As mentioned before, with an In mole fraction of about 0.5, AlGaInP is lattice matched to GaAs. Low dislocation density GaAs substrates are readily available today. In MOVPE, InP-based material can be grown with high purity and background-doping levels in the range of 10^{14} cm^{-3}. To avoid ordering, the AlGaInP epitaxial layers are grown with a certain misorientation, typically with a tilt angle $> 2°$ from the growth plane.

As shown in Fig. 2.2.2, the InGaP strained QWs are usually sandwiched between AlGaInP/AlGaInP waveguide and cladding layers. This active region can however also be combined with As and P containing layers, such as AlGaAs waveguide and cladding layers.

The operation of a diode laser requires the presence of a pn-junction. For usual applications the lower cladding and waveguide layers are grown n-type on an n-type substrate and the upper cladding and waveguide layers p-type. The GaAs cap, which serves as a current spreading layer is also highly p-doped.

For the n-doping, tellurium (Te) and silicon (Si) are the most widespread dopants, but selenium (Se) has also been used in some MOVPE laboratories [26]. Every dopant has its pros and contras. Te for example is good against ordering as compared to Si; however Si-doped devices have better aging properties. Furthermore, Si has a processing advantage on Te, as its incorporation is less sensitive on the growth temperature.
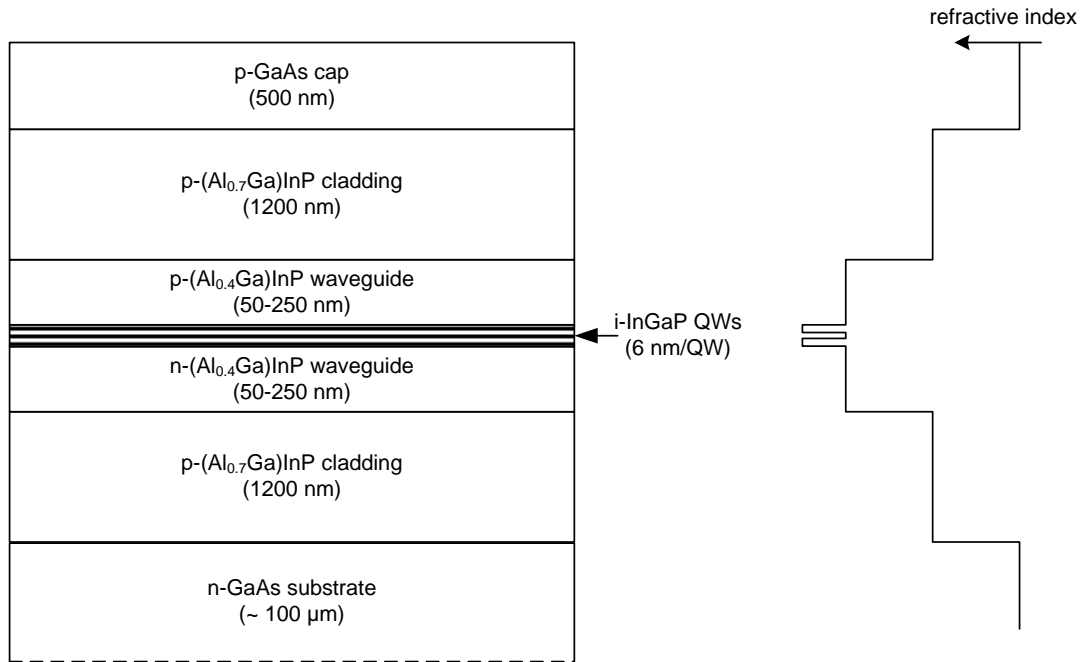
Fig. 2.2.2. Standard AlGaInP epitaxy structure

As for p-doping, zinc (Zn) and magnesium (Mg) are the most common candidates for MOVPE grown AlGaInP material. Beryllium (Be) can also be used as a dopant; however its high toxicity made it unpopular in the recent years. Zn as dopant in Al-GaInP material has the advantage that it leads to reproducible doping levels and it is easy to control. Moreover, it does not cause memory effect problems in the MOVPE reactor [21]. Nevertheless, one major problem of Zn is its re-evaporation, which reduces the incorporation efficiency especially at high temperatures. The doping level of Zn can be increased by reducing the temperature (to around 700 °C) and compromising on the material quality. On the other hand, Mg as dopant has relatively high incorporation efficiency, and diffuses less than Zn. However, this dopant is notorious for transients caused by absorption of the precursor molecules in the stainless steel tubing and on the reactor walls and also for memory effects.

So for AlGaInP, the choice is between two p-type dopants that both have their respective advantages and drawbacks [21].

2.3 AlGaInP laser design

In several applications like hand-held devices, where eye safety is a major issue, low-power lasers are the devices of choice. Moreover, for applications like short distance or chip-to-chip optical communication, low-power lasers are also desired due to their low-cost, low-power consumption, and often due to their ability to operate in single mode. On the other hand, applications where high-power is required include laser projection, and many medical therapies where the ability to focus the light to a small spot of high power density is required. The distinction between low-power and high-power semiconductor lasers is not very well defined. It may depend on the type of laser and the application for which it is designed. Generally speaking, 50 mW (or more) cw power for broad-area multimode lasers and laser arrays are considered to be high-power **[5]**.

2.3.1 Low-power lasers

Low-power AlGaInP lasers can be found in several applications. For example, Al-GaInP low-power vertical cavity surface emitting lasers (VCSELs) are strongly desired for optical data communication via plastic optical fibers with absorption minimum at 650 nm, used in automobiles, air planes, offices, and in computer networks **[25]**. On the other hand, edge-emitting low-power lasers, like ridge lasers, are used in applications like disk data storage systems, and as light sources in standard single mode fibers. Figure 2.3.1 shows a cross-section schematic of a standard AlGaInP ridge laser. Depending on the ridge width, which is usually less than 4 μm, lateral single mode lasing can be achieved.
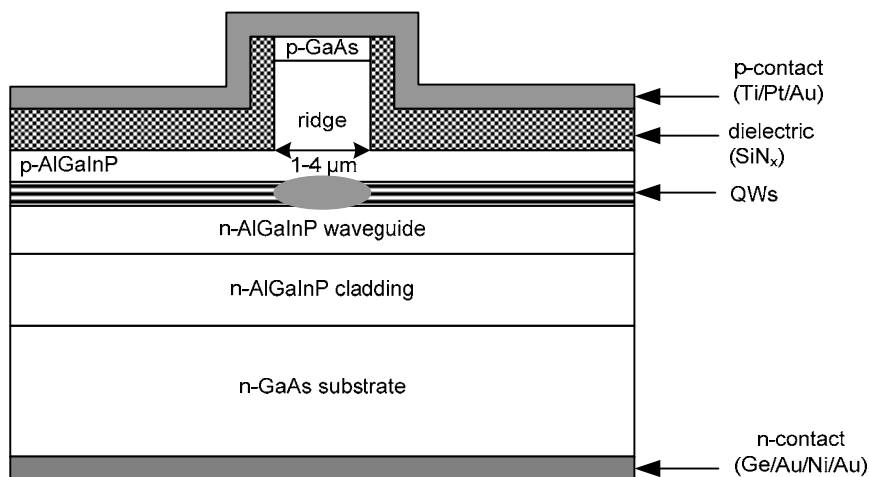
Fig. 2.3.1. Cross-section of a standard low-power AlGaInP ridge laser. The spot under the ridge shows where the lasing is guided.

2.3.2 High-power lasers

Due to the high quality of the semiconductor material, scaling the laser's cavity width and length allows to extract more power out of a resonator. The most common high-power laser design is the broad-area (BA) design. Figure 2.3.2(a) shows a standard AlGaInP BA laser cross-section schematic.

Standard AlGaInP BA lasers used in this study have a resonator length of 1200 µm, a resonator width of 100 µm and a chip width of 500 µm. Figure 2.3.2(b) shows a 3-dimensional schematic of the AlGaInP BA laser structure with a current-blocking region design. This region creates a window of about 30 µm at the facet where no current flows. This reduces the facet temperature and eventually improves the COD level (see chapters 5 and 6).

BA lasers are particularly easy to fabricate. Unlike ridge waveguide lasers which have both current confinement and optical confinement with index-guiding, BA lasers only have current confinement and the lateral waveguide is formed by gain-guiding. This is achieved by defining an active stripe through etching 10 µm wide trenches in the GaAs cap layer and insulating both sides of the stripe with a dielectric, typically SiN_x, SiO_2, or Al_2O_3.
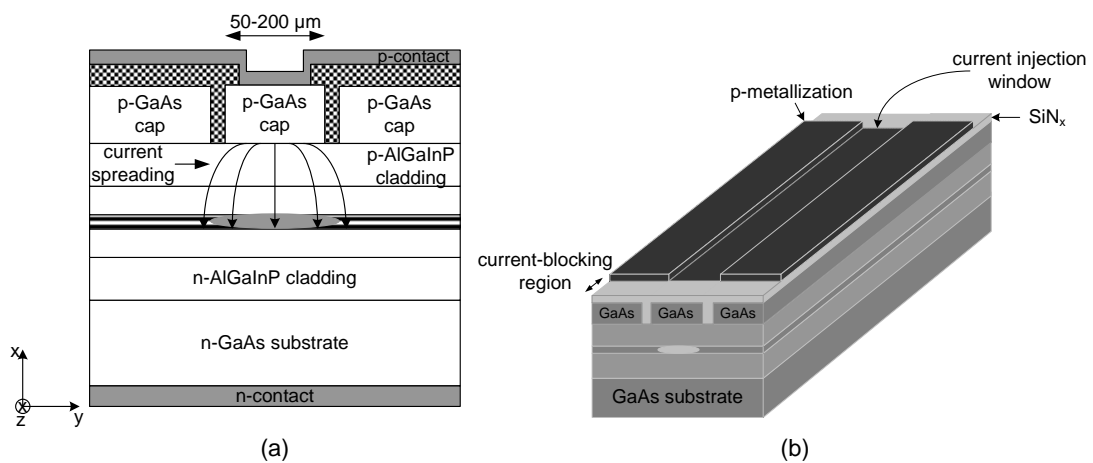
Fig. 2.3.2. (a) Cross-section of a standard high-power AlGaInP BA laser. Current spreading is sketched by arrows. (b) 3-dimensional standard high-power AlGaInP BA laser structure with a current blocking region design.

Current injection occurs inside the stripe (50-200 µm width) and there is no build-in index-guiding. In the lateral y-direction, the current spreads before reaching the active layer. There, injected carriers are furthermore redistributed by diffusion. Roughly speaking, the optical wave will be able to propagate in the z-direction in the region exhibiting positive gain, whereas absorption will take place on both sides of the active stripe. Due to this mechanism, one speaks of gain-guiding (in contrast to index guiding) [28].
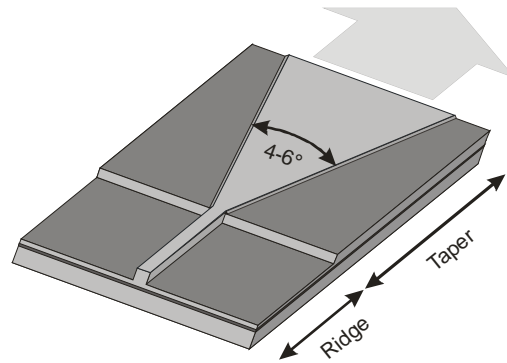
Fig. 2.3.3. Tapered laser design.

High-power BA lasers are multimode lasers. In fact, applications such as PDT usually do not require single mode operation. Some applications, on the other hand, such as laser projection, require both high-power and single mode operation. An intelligent design, namely the tapered laser design, combines both concepts of ridge and BA laser designs. Figure 2.3.3 shows a tapered laser design.

In a tapered laser, single mode index-guiding is achieved by the ridge (injector), and light amplification is attained by the taper (amplifier). Both sections set up an instable resonator. Red output powers ~ 1 W with a beam quality $M^2_{1/e^2} < 2$ have already been achieved. The ridge and the amplifier can have common or separate current injection contacts, depending on the desired working point and application. When working at (relatively) low powers, lower threshold currents and better beam quality can be obtained by separately contacting ridge and amplifier. Furthermore, fast modulation can also be obtained using this configuration. When working at higher powers, a common contact for ridge and amplifier will result in higher differential efficiency, but also a higher threshold current.

2.3.3 High-power laser bars

One of the most common methods to generate more output power from a semiconductor diode laser is to increase the width of the emitting area. However, if the width of a single emitter is increased, filamentation and lateral mode instabilities become increasingly severe. This means that the optical power is no longer distributed homogeneously along the output facet, which most likely will lead to fast degradation of the diode laser. As a matter of fact, the output power of single-stripe BA lasers cannot be enhanced significantly for stripe width exceeding 200 μm **[21]**. A practical way to increase the output power is the monolithic integration of many emitters into one diode laser bar. These emitters are optically and sometimes electrically isolated from each other. Each emitter can be driven at moderate output power, which does not lead to an accelerated degradation of the output facet. By combining the power of all single emitters in the laser bar, very high output powers can be achieved **[21]**.

In high-power laser bars, thermal management, soldering procedure, and heat-sink architecture are a real technological challenge and play an important role to achieve stable high-power operation. Figure 2.3.4 illustrates part of a laser bar cross-section with optically and electrically isolated single BA emitters. Electrical isolation usually serves for single emitter test purposes on unmounted bars. However, as will be seen in section 2.3.5, high-power laser bars are usually mounted p-side down on one heat sink for better heat management, which automatically makes the single emitters electrically connected.
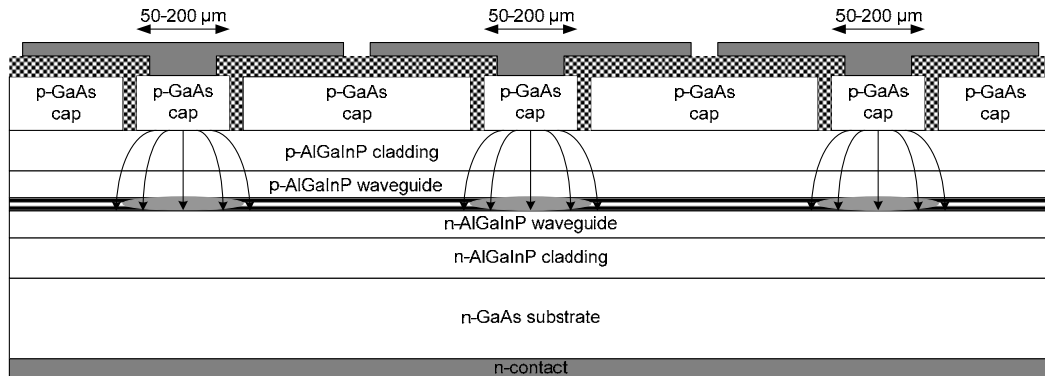
Fig. 2.3.4. Part of a laser bar (here shown with 3 lasers) with optically and electrically isolated single BA emitters based on the BA laser design shown in Fig. 2.3.2.

Since the technology to process single-stripe emitters and diode laser bars is almost identical, the fabrication of diode laser bars means only a change of the mask layout. However, each process step must be carried out on a very high reliability level, due to the high number (5 to 20 single emitters per bar) of single emitters integrated in one bar. A defect of one emitter can be the reason for the failure of the whole bar by current or thermal effects.

2.3.4 Facet coating

In edge-emitting semiconductor lasers, coating the laser facets plays a crucial role in ensuring long-term reliability and stable optical output power. The facets of the lasers are often coated with dielectric materials which serve first as a passivation and protection against external effects such as oxidation, moisture, etc…and second as a modification of the facets reflectivities in order to obtain maximum output power. Figure 2.3.5 illustrates a typical configuration of a front and back facet coated semiconductor laser. The desired facet reflectivities are typically > 90 % for the high-reflection (HR) side and between 5 and 20% for the anti-reflection (AR) side.
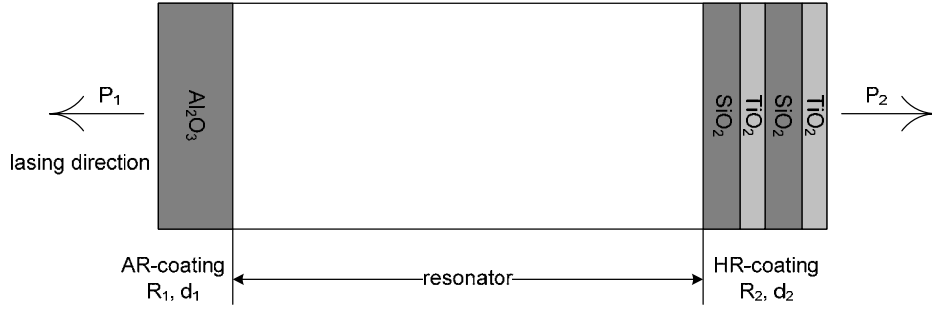
Fig. 2.3.5. Typical facet coating design of edge-emitting lasers. Here Al_2O_3 and SiO_2/TiO_2 are shown as example coating materials for the anti-reflection (AR) and high-reflection (HR) coatings respectively. R_1 and R_2 represent the facet reflectivities, d_1 and d_2 the coating thicknesses, and P_1 and P_2 the output powers from the resonator AR and HR facets, respectively.

The general formula to calculate the reflectivity of a homogeneous plane wave being incident from a bulk semiconductor of refractive index n_{eff} onto a layer of thickness d and refractive index n, and transmitted into air (as is usually the case) is obtained as **[28]**

$$R(n,d) = \frac{(1-n_{eff})^2 \cos^2(nkd) + (\frac{n_{eff}}{n} - n)^2 \sin^2(nkd)}{(1+n_{eff})^2 \cos^2(nkd) + (\frac{n_{eff}}{n} + n)^2 \sin^2(nkd)} \tag{2.1}$$

where $k = 2\pi/\lambda$, λ is the laser's wavelength, and n_{eff} being the effective refractive index for the optical wave traveling in the waveguide between the laser mirrors. Equation (2.1) is a periodic function. With a periodicity in thickness of $\frac{\lambda}{2n}$, R varies between the minimum reflectivity

$$R_{min} = \frac{(n_{eff} - n^2)^2}{(n_{eff} + n^2)^2} \text{ for } d = \frac{\lambda}{4n} + m\frac{\lambda}{2n}, m = 0, 1, \ldots \tag{2.2}$$

and the maximum reflectivity

$$R_{max} = \frac{(1-n_{eff})^2}{(1+n_{eff})^2} \text{ for } d = m\frac{\lambda}{2n}, m = 0, 1, \ldots \tag{2.3}$$

where R_{max} is just equal to the reflectivity of an uncoated facet. In case of $n = \sqrt{neff}$, AR-coating with $R_{min} = 0$ is achieved at a particular wavelength λ and thickness d satisfying the condition in equation (2.2).

Figure 2.3.6(a) shows the calculated reflectivity of the front mirror of a 650 nm Al-GaInP laser as illustrated in Fig. 2.3.5, using one Al_2O_3 AR-coating layer with refractive index n ≈ 1.68. A reflectivity of for example 10 % can be achieved at a layer thickness of around 130 nm or 260 nm. Note that R_{min} in this case cannot reach zero, because the refractive index of Al_2O_3 is fixed.

With an alternating layer stack as for the back facet in Fig. 2.3.5, and thickness of a quarter wave each, i.e. $d_i = \dfrac{\lambda}{4n_i}$, a so-called Bragg reflector is formed, serving as a HR-coating. The concept of a Bragg reflector is that many small reflections can add up to a large net reflection. At the Bragg frequency, the reflections from each discontinuity add up exactly in phase. The maximum reflectivity increases both with an increasing number of layer pairs and with a larger refractive index difference, for example between SiO_2 with n ≈ 1.45 and TiO_2 with n ≈ 2.27. The net reflectivity can be calculated using the transfer matrix theory described in [29].

Figure 2.3.6(b) shows the calculated reflectivities of a Bragg-reflector with two and three pairs of SiO_2/TiO_2 layers. It can be seen that at 650 nm, a reflectivity of about 82 % can be achieved when using two pairs of layers, and increases to 92 % when using three pairs of such layers.
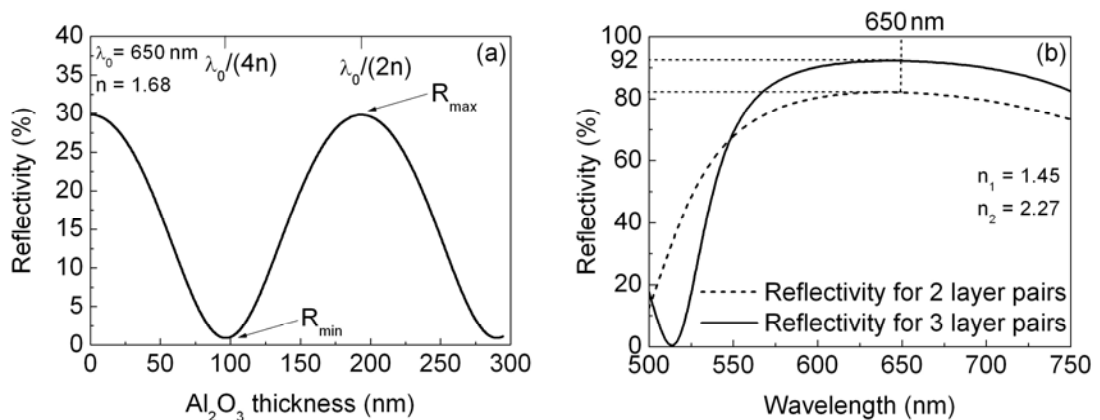
Fig. 2.3.6. Calculated reflectivities R of the front (a) and back (b) mirrors of a 650 nm AlGaInP laser having facet coatings as illustrated in Fig. 2.3.5. For the front mirror, one Al_2O_3 layer with n ≈ 1.68 is used. For the back mirror, a Bragg-reflector with two (dashed line) and three (straight line) layer pairs of SiO_2/TiO_2 was used.

A device with modified reflectivities according to Fig. 2.3.5 is often denoted as AR/HR-coated laser. With the new reflectivities R_1 and R_2, the output powers P_1 and P_2 from the resonator's AR and HR facets, respectively, obey the ratio [28]

$$\frac{P_1}{P_2} = \frac{1 - R_1}{1 - R_2} \sqrt{\frac{R_2}{R_1}} \qquad\qquad (2.4)$$

This automatically indicates that a laser without any facet coatings emits 50 % of its output power from each facet.

2.3.5 Mounting

Mounting and packaging of diode-laser chips are among the most essential processes in the production of AlGaInP lasers. Though many different types of heat-sink carriers and mounting technologies are available nowadays, the discussion in this chapter concentrates on two submount carriers used in this study, namely the C-mount carrier for high-power single emitters, and the Sirilas® passive heat-sink carrier for high-power laser bars.

The efficiency of diode lasers is high compared to classical lasers, thus creating only a smaller amount of waste heat. However what makes heat-sinking so crucial is that the dissipated power is generated over a very small area. Dissipated power densities > 10 kW/cm^2 have to be managed for high-power laser bars.

Two essential methods to mount laser diodes are available: "p-side up" and "p-side down". Even though the p-side up technique is not uncommon for low-power diode lasers, p-side down is essential for efficient heat management in high-power lasers. In the p-side down technique, the heat emitting active region of the laser is closer to the heat-sink for better heat removal. Nonetheless, if not properly applied, this technique may be more critical because stress due to soldering may lead to strain and defect creation, or even complete laser destruction.

C-mount

C-mount is a gold plated copper heat-sink carrier, with length and width adjustable to fit any laser's width and length. For example, the standard chip width and length of an AlGaInP BA laser are 500 μm and 1200 μm respectively. This can be mounted on a C-mount carrier with width×length×height ~ 2×6×7 mm^3. C-mount carriers are usually sufficient heat sink elements for single emitters. A picture of a p-side down mounted BA AlGaInP laser on a C-mount heat-sink carrier is shown in Fig. 2.3.7(a).

Fig. 2.3.7(b) shows a close-up front-view image of a p-side down mounted AlGaInP laser. Between the laser and the C-mount carrier lies an AlN$_x$ or CuW heat spreader. A 3-dimensional BA laser schematic mounted p-side down on a C-mount heat-sink is illustrated in Fig. 2.3.8(a) and a side-view in Fig. 2.3.8(b).

The approximately 10 μm mounting offset which is shown in Fig. 2.3.8 prevents serious distortions of the expanding beam through parasitic reflections and solder flow on the facet during mounting. However, this aggravates the heat removal efficiency, and can lead to heat induced problems such as worsening the COD level and the degradation of the front facet (see chapters 4 and 5); nevertheless, it is a necessary trade-off.

(a)   (b)
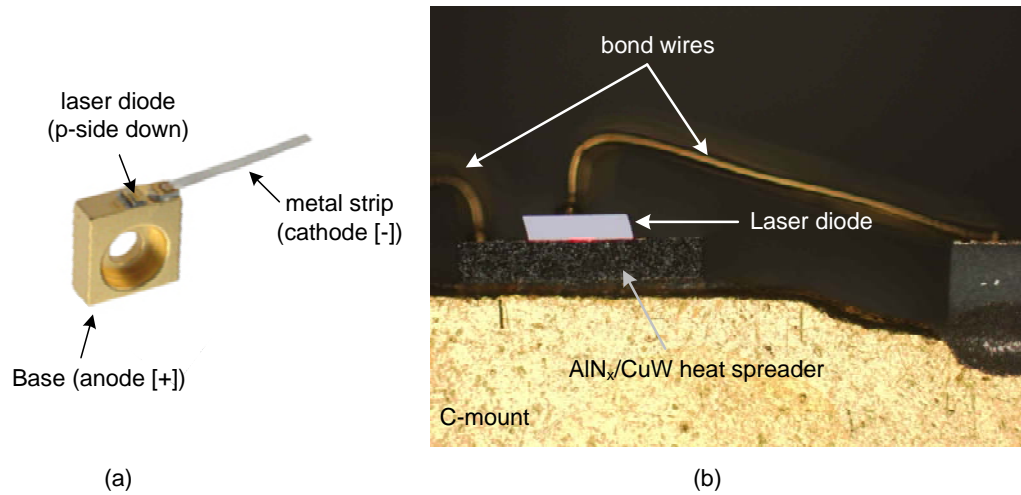
Fig. 2.3.7. (a) C-mount heat-sink carrier. Here a p-side down mounting configuration is depicted. (b) Close-up front-view image of a p-side down mounted BA AlGaInP laser diode.
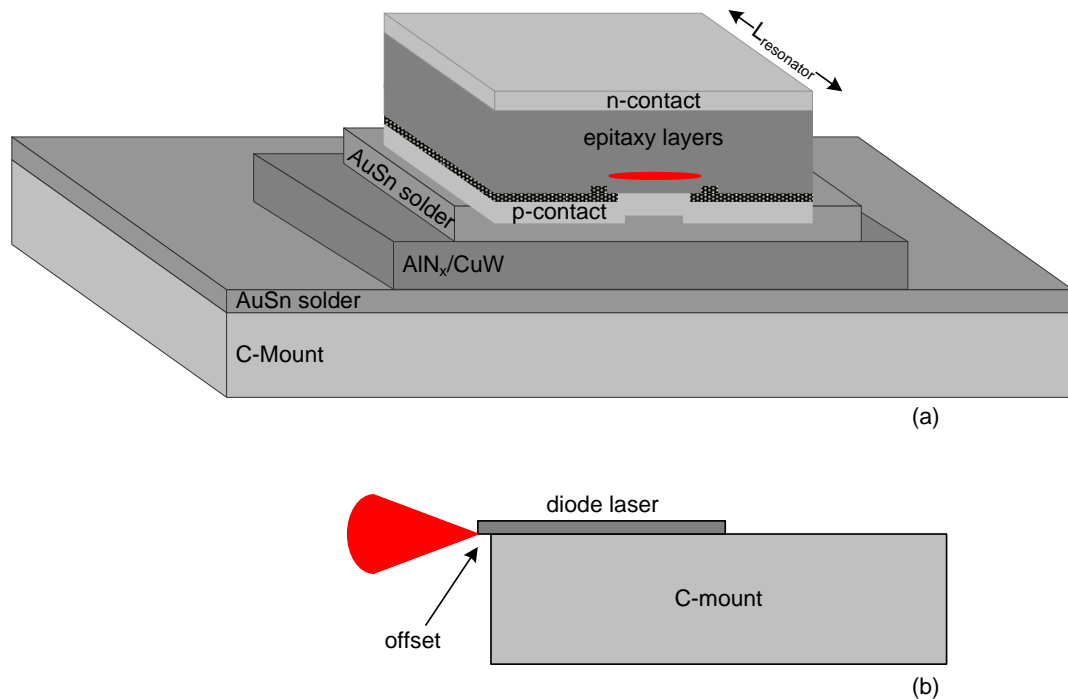
Fig. 2.3.8. (a) p-Side down mounted BA laser on a C-mount heat-sink. Usually, the lasers are soldered with AuSn on an AlN_x or CuW heat spreader. (b) Side-view of a mounted BA laser showing the necessary mounting offset to prevent the expanding beam distortions and solder flow on the facet.

Sirilas®

High-power laser bars require very efficient heat-sink carriers. Sirilas® passive heat-sink carriers were specially developed at OSRAM for 5- to 10-emitter laser bars. The standard laser bar is 2.5 mm long, consisting of 5 BA 100 μm emitters with a pitch of 500 μm. A picture and schematic of a Sirilas® passive heat-sink carrier is shown in Fig. 2.3.9.
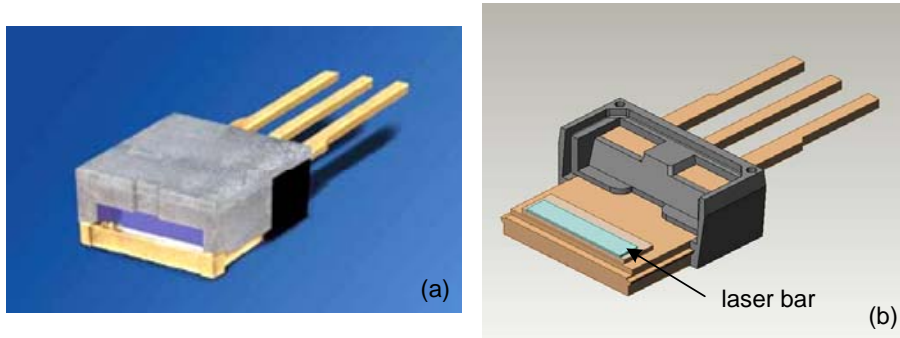
Fig. 2.3.9. (a) Encapsulated Sirilas® five-emitter laser bar heat-sink carrier. (b) Open Sirilas® heat-sink carrier showing where the laser bar can be mounted. The three metal stripes serve as laser cathode, common ground, and temperature sensor anode.

Usually, laser bars are always mounted p-side down, due to the huge amount of dissipated heat that needs to be dealt with. On top of that, due to the relatively large length of laser bars, great care should be taken during mounting to prevent problems such as soldering inhomogeneities, which may affect the performance and lifetime of the bars.

A Sirilas® submount can also be designed with an integrated active liquid cooling system for better heat management. However, due to the undesired liquid cooling, which makes the unit equipment larger, more vulnerable, and more expensive, Sirilas® passive devices are usually favored by equipment manufacturers, such as PDT systems producers.

2.4 AlGaInP laser characterization

2.4.1 Introduction to recombination mechanisms in active regions

An active region is in general defined as the region where recombining carriers contributes to useful gain and photon emission. For the double heterostructure active region, the injected current provides the generation term, and various radiative and nonradiative recombination processes as well as carrier leakage provide recombination terms. Thus we can write the rate equation,

$$\frac{dn_c}{dt} = G_{gen} - R_{rec} \qquad (2.5)$$

where n_c is the carrier density, G_{gen} is the rate of injected electrons and R_{rec} is the rate of recombining electrons per unit volume in the active region. Since there are I/q electrons per second being injected into the active region, $G_{gen} = j/qd$, where d is the thickness of the active region, and q the electron charge **[29]**.

The recombination process is a bit more complicated and includes several recombination mechanisms. There is a spontaneous recombination rate, R_{sp}, and a nonradiative recombination rate, R_{nr}, a carrier leakage rate, R_l, and a stimulated recombination rate R_{st}.

Nonradiative recombination means a conduction band electron recombines with a valence band hole without generating any useful photons. Instead, the energy is dissipated as heat in the semiconductor crystal lattice. In practice, two nonradiative recombination mechanisms for carriers are important. The first involves nonradiative recombination centers, such as point defects, surfaces, and interfaces in the active region of the laser. The second mechanism is Auger recombination, in which the electron-hole recombination energy is given to another electron or hole in the form of kinetic energy. In most III-V semiconductor material, such as InGaP material, Auger recombination is low and is usually neglected.

In double heterostructure and QW active layers, once the carriers fill to the top of the barrier, they are free to diffuse into the cladding regions. Thus in QW lasers for example, carrier leakage is present if the transverse and/or lateral potential barriers are not sufficiently high. With increased temperatures, the carrier leakage increases as the fraction of the carriers in the high energy tail increases.

Finally, under the right conditions (e.g. in a laser), a stimulated recombination, R_{st}, includes both stimulated absorption and emission. Thus R_{rec} can be written as

$$R_{rec} = R_{sp} + R_{nr} + R_l + R_{st}. \qquad (2.6)$$

The first three terms on the right refer to the natural or unstimulated carrier decay process. When due to optical excitation or current injection a sufficient large number of excess carriers is present in a direct semiconductor, stimulated emission dominates over spontaneous transitions. It is common to describe the natural decay processes by a carrier lifetime, τ_s. In the absence of photons or a generation term, the rate equation for carrier decay is just, $dn_c/dt = n_c/\tau_s$, where $n_c/\tau_s \equiv R_{sp} + R_{nr} + R_l$ **[29]**.

2.4.2 Basic laser relations

When passing through an absorbing material of thickness d in the z-direction, the intensity I of a planar optical wave exponentially decreases as [21]

$$I(z) = I_0 e^{(-\alpha z)} \qquad (2.7)$$

with I_0 being the initial intensity and α the intensity-absorbing coefficient. In laser active semiconductor materials, amplification of the optical wave is achieved. In this case, the exponential increase in intensity can be described by a negative value of α which is referred as gain $g = -\alpha$. In an optical waveguide, only part of the intensity pattern of the optical mode overlaps with the active region, which is usually located in the core of the waveguide. This is usually defined as the confinement factor Γ (< 1), and hence defining the modal gain as $g_{modal} = \Gamma g$. For a mode traveling along the optical waveguide, the intensity-absorption coefficient α is usually split into two parts, one describing the intrinsic modal absorption α_i and the other describing the modal gain $g_{modal} = \Gamma g$ which depends on the density of the injected carriers as [21]

$$\alpha = \alpha_i - \Gamma g . \qquad (2.8)$$

The intrinsic modal absorption is caused by scattering of the optical mode at defects or rough interfaces and by free-carrier absorption. Whereas scattering is extremely low for semiconductor diode lasers with good crystalline quality, free-carrier absorption cannot be avoided, since part of the optical mode pattern overlaps with the p- and n-doped cladding regions. When the modal gain Γg is larger than the modal loss α_i, the propagating optical mode is amplified [21].

In a laser device, the optical waveguide is combined with a Fabry-Perot resonator having mirror reflectivities R_1 and R_2. Some optical intensity leaves the cavity at these mirrors and contributes to the laser output beam. The intensity I_{rt} of the optical mode after a roundtrip in a cavity of length L is given by [21].

$$I_{rt} = I_0 R_1 R_2 e^{[2(\Gamma g - \alpha_i)L]} . \qquad (2.9)$$

Lasing occurs when the gain provided to the optical mode compensates the intrinsic absorption and the mirror losses for a roundtrip. In this case, the intensity I_{rt} after a roundtrip in the cavity again has its initial value I_0. Equation (2.9) will then lead to the condition for self-stimulation or laser oscillation as

$$R_1 R_2 e^{[2(\Gamma g - \alpha_i)L]} = 1 \qquad (2.10)$$

and the threshold gain relation

$$\Gamma g_{th} = \alpha_i + \frac{1}{2L}\ln\left(\frac{1}{R_1 R_2}\right) = \alpha_i + \alpha_m \qquad (2.11)$$

where α_m represents the mirror losses.

Amplification in a laser starts for carrier density values $n_c \geq n_t$, where n_c is the total carrier density, and n_t the transparency carrier density. For QW lasers, calculations of the peak gain coefficient g_p as function of the carrier density show that a logarithmic relationship in the form of [29]

$$g_p = g_0 \ln\frac{n_c}{n_t} \qquad (2.12)$$

is valid, where g_0 is a material dependent gain coefficient.

The threshold carrier density relation can now be obtained as

$$n_{th} = n_t e^{(g_{th}/g_0)} = n_t e^{\left(\frac{\alpha_i + \alpha_m}{\Gamma g_0}\right)}. \qquad (2.13)$$

Under stationary conditions, the carrier density n_c grows with increasing current density j as

$$n_c = \frac{\eta_i j \tau_s}{qd} \qquad (2.14)$$

where η_i the injection current efficiency, and denotes the fraction of current <u>above threshold</u> which contributes to stimulated emission. η_i usually depends on the lateral leakage currents (e.g. in a BA laser), recombination in the surrounding layers, and/or carrier leakage due to incomplete carrier confinement in the active layer (as carriers can escape for example to the barriers and cladding regions in a case of a QW laser) [28][29].

Equation (2.14) leads to threshold current density relation

$$j_{th} = j_t e^{\left(\frac{g_{th}}{g_0}\right)} = j_t e^{\left(\frac{\alpha_i + \alpha_m}{\Gamma g_0}\right)} \tag{2.15}$$

where $j_t = \dfrac{qd}{\eta_i \tau_s} n_t$ is the transparency current density.

When considering a laser cavity (active region) of length L, width b, and thickness d (including QW and waveguides), the total stored photon energy in a resonator mode in the volume $Vol = (L \times b \times d)/\Gamma$ is $E_{ph} = N \times Vol \times \hbar w$, where N represents the photon density and $\hbar w = hc/\lambda$ the photon energy (h = Planck's constant, c = speed of light in vacuum, λ = laser wavelength). Writing the threshold current as $I_{th} = I \times L \times j_{th}$, the optical power coupled out of the cavity through both mirrors is therefore

$$P_{OUT} = \eta_i \frac{\hbar w}{q} \frac{\alpha_m}{\alpha_i + \alpha_m} \left(I - I_{th} \right). \tag{2.16}$$

Introducing the differential quantum efficiency η_d as

$$\eta_d = \frac{d\left(P/\hbar w\right)}{d\left(I/q\right)} = \eta_i \frac{\alpha_m}{\alpha_i + \alpha_m} \tag{2.17}$$

and the slope efficiency η_{slope} as

$$\eta_{slope} = \eta_d \frac{\hbar w}{q} \tag{2.18}$$

the expression of the output power becomes

$$P_{OUT} = \eta_{slope} \left(I - I_{th} \right) \tag{2.19}$$

$\hbar w/q$ is usually referred to as the bandgap voltage. The wall-plug efficiency η_{wp}, also called conversion efficiency, tells how much pumping power is converted to coherent radiation. The electric pumping power is V×I, where V is the laser voltage, and I is the injection current. η_{wp} can be calculated as

$$\eta_{wp} = \frac{P_{OUT}}{VI}. \tag{2.20}$$

2.4.3 Electro-optical characterization

Electro-optical characterization, also called power-current-voltage (PIV-) characterization, is the first measurement that tells about the laser's performance. PIV-measurements enable the extraction of the following parameters:

- Total optical output power P_{OUT}
- Threshold current I_{th}
- Slope efficiency η_{slope}
- Series resistance R_s
- Kink voltage V_0
- Wall-plug efficiency η_{wp}
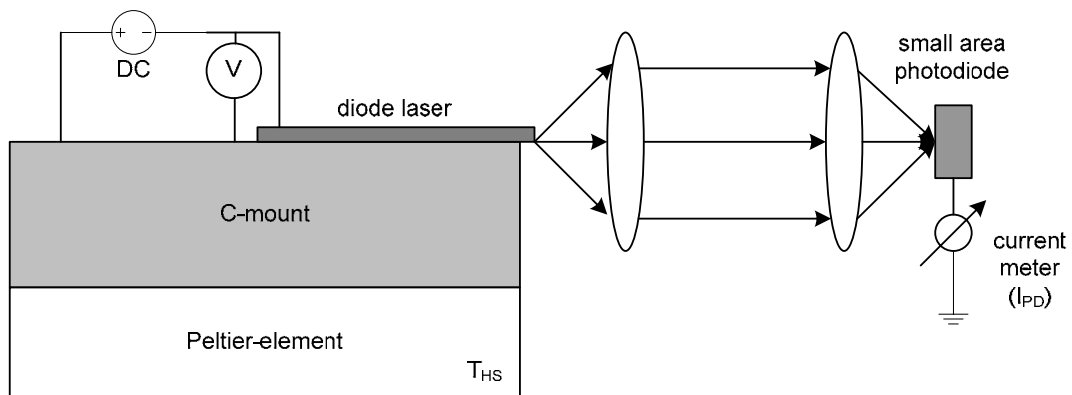
Fig. 2.4.1. A lens-coupling PIV-measurement setup. I_{PD} = photodiode output current

A typical way to measure the PIV-characteristics of single emitters is with a lens-coupling measurement setup as illustrated in Fig. 2.4.1. Here, the entire laser light from the output facet is gathered and concentrated on a small area semiconductor calibrated photodiode (PD). Other measurement setups include direct measurement with a large area ($\sim 10\ mm^2$) PD, which is closely placed in front of the laser or using an integrating sphere, which replaces the two lenses in the lens-coupling setup.

PIV-measurements can be done either in pulse mode, to avoid self heating of the laser, or in continuous wave (cw) mode, depending on the required analysis. Pulse measurements are for example used for fast testing of the lasers before mounting, and to determine the temperature dependence of the laser (section 2.4.4). A typical measured PIV-curve of a high-power 650 nm AlGaInP standard BA laser mounted on a C-mount is shown in Fig. 2.4.2. The measurements were performed in cw mode with 0.1 A current steps and at a heat-sink temperature $T_{HS} = 20\,°C$, regulated by a Peltier-element. The parameters that can directly be extracted from such measurements are indicated on the graph. Here a threshold current $I_{th} = 0.4$ A and a slope efficiency $\eta_{slope} = 0.95$ were achieved. The kink voltage, V_0, which is ideally almost

equal to the bandgap voltage $\hbar\omega/q$, and the series resistance R_s can be measured from the VI-curve. From those values, the total voltage $V = V_0 + R_sI$ can be determined.
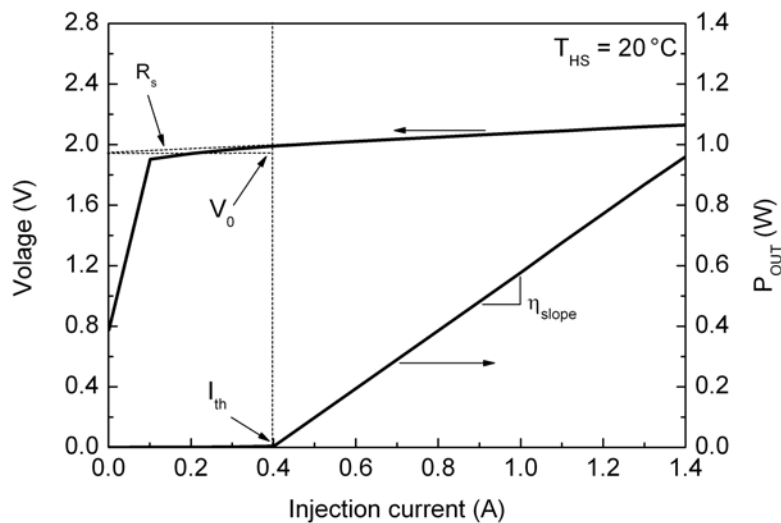
Fig. 2.4.2. Typical cw PIV-curves of a high-power 650 nm AlGaInP standard BA laser mounted on a C-mount. T_{HS} was set to 20°C.

From the PIV-measurement data, the wall-plug efficiency can be calculated according to equation (2.20). The wall-plug efficiency of the same laser of Fig. 2.4.2 is depicted in Fig. 2.4.3.
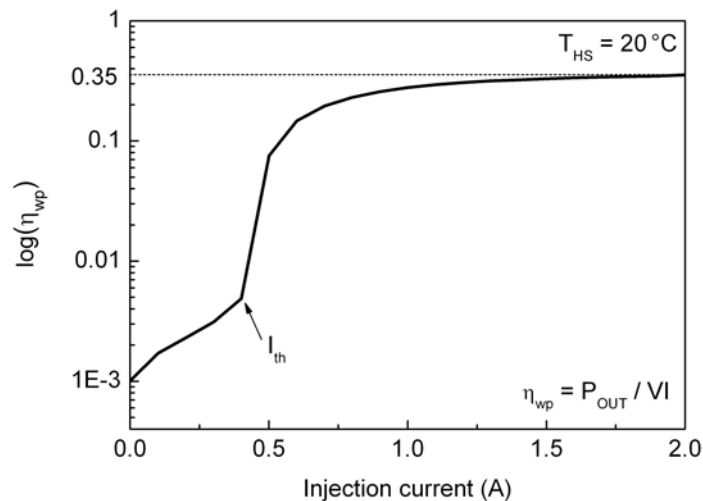
Fig. 2.4.3. Wall-plug efficiency of the same laser of Fig. 2.4.2

Fig. 2.4.3 shows that the wall-plug efficiency increases slowly below threshold due to spontaneous emission, and then undergoes a steep increase above threshold when population inversion starts. Finally, it saturates at high currents due to increased car-

rier leakage. A $\eta_{wp} = 35\%$ value is typical for high-power 650 nm AlGaInP lasers, and decreases for short-wavelength AlGaInP lasers, due to increased carrier leakage at the shallower QWs.

2.4.4 Temperature dependence

When measured at different heat-sink temperatures, the PI-curve of a laser exhibits an increase in threshold current and a decrease in the slope efficiency with increasing T_{HS}. Figure 2.4.4(a) shows PI-curves of a standard 638 nm AlGaInP BA laser mounted on a C-mount for different T_{HS}. The measurement was done in pulse mode (pulse width: 1 µs, pulse frequency 10 kHz) to avoid self heating of the laser. Figure 2.4.4(b) shows how I_{th} and η_{slope} change with T_{HS} for the same laser.

The increase of I_{th} with increasing T_{HS} is due to the laser's gain dependence on temperature. The gain is reduced with increasing temperature, because injected carriers spread over a wider range in energy with higher temperatures. Also, the increased internal loss occurs due to the required higher carrier densities for reaching threshold.
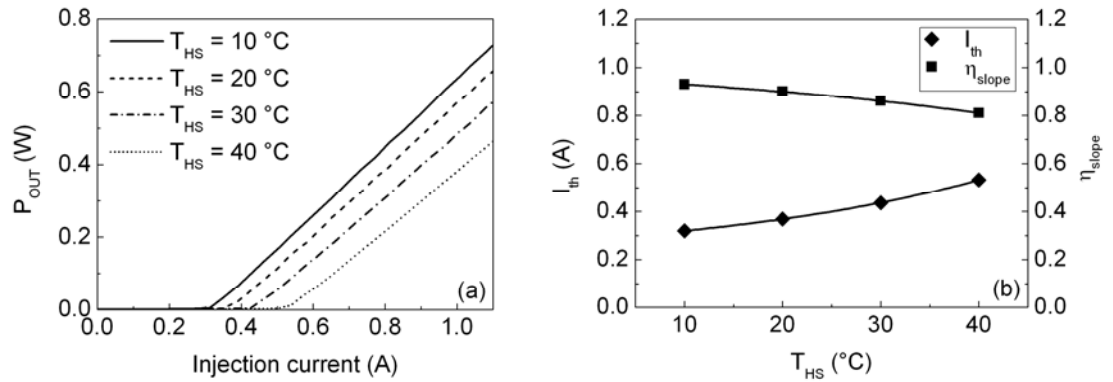
Fig. 2.4.4. (a) PI-curves of a standard 638 nm AlGaInP BA laser mounted on a C-mount for different T_{HS} in pulse mode (pulse width: 1 µs, pulse frequency 10 kHz). (b) Change in I_{th} and η_{slope} with T_{HS} for the same laser.

Both the gain and the internal loss variations result in an exponential temperature dependence of the threshold current, which can empirically be expressed as [29]

$$I_{th}(T) = I_{Ref}\, e^{\frac{T - T_{Ref}}{T_0}} \tag{2.21}$$

where T_0 is some overall characteristic temperature given in Kelvin, and I_{Ref} is the threshold current at a certain reference temperature T_{Ref}.

The decrease of η_{slope} with increasing T_{HS}, is mainly associated to the increased carrier leakage at higher temperatures. Likewise, the change of η_{slope} with temperature can be expressed as

$$\eta_{slope}(T) = \eta_{Ref} e^{-\left(\frac{T - T_{Ref}}{T_1}\right)}.$$

$$(2.22)$$

T_0 and T_1 can tell how strong the threshold current and the slope efficiency depend on temperature. For example, a small T_0 indicate a larger dependence on temperature (since $dI_{th}/dT = I_{th}/T_0$). There are no typical values for T_0 and T_1 for AlGaInP lasers, because they strongly depend on many parameter variations such as the epitaxy design, the number of QWs, the doping, etc. In general, AlGaInP lasers are more vulnerable to temperature variations than AlGaAs based lasers, due to their higher thermal and electrical resistivities **[32][33]** and higher carrier leakage. Moreover, due to this high temperature sensitivity, especially in short wavelength AlGaInP lasers, experimental results usually deviate from the phenomenological equations (2.21) and (2.22). For the example shown in Fig. 2.4.4(b), $I_{th}(T)$ and $\eta_{slope}(T)$ is best fitted with $I_{th}(T)[A] = 0.088 e^{T[K]/30} + 0.19$ and $\eta_{slope}(T) = 0.083 e^{-T[K]/40} + 1.03$.

2.4.5 Thermal resistance

In a laser, thermal resistance is a measure of the device's ability to dissipate internally generated heat. Thermal resistance is defined as

$$R_{th} = \frac{\Delta T}{P_{diss}} = \frac{d\lambda/dP_{diss}}{d\lambda/dT}$$

$$(2.23)$$

which is the ratio of the temperature increase in the device ΔT and the dissipated electrical power P_{diss}. The evaluation procedure of R_{th} can be done as follows:

1. Measure the peak wavelength $\lambda_0(T)$ shift with increasing I and the cw PI-curves at different (at least two) T_{HS} values.
2. Calculate the dissipated power $P_{diss} = VI - P_{OUT}$.
3. Evaluate $\dfrac{d\lambda}{dT}$ and R_{th} (and λ_a) from the following equation

$$\lambda_0(T) = \lambda_a + \frac{d\lambda}{dT}(T - T_a) = \lambda_a + \frac{d\lambda}{dT}(T_{HS} + P_{diss} \times R_{th} - T_a)$$

$$(2.24)$$

where T_a is one fixed value of T_{HS}, and λ_a is the wavelength at T_a at I = 0 A, i.e. without the influence of internal laser heating. $T = T_{HS} + P_{diss} \times R_{th}$ represents the device's bulk temperature (will be denoted T_{BULK} in later chapters).

As an example, R_{th} of the same standard 638 nm AlGaInP BA laser on C-mount characterized in the previous section is determined. Figure 2.4.5(a) displays the spectra measurements needed to determine the λ_0 shift at different T_{HS} (here 10, 15, and 20 °C) for current values between 0.5 and 0.9 A and 0.1 A steps. For example, λ_0 at 10°C and 0.5 A has a value of 636.6 nm and shifts to 637.3 nm at 0.9 A for the same heat sink temperature (indicated by arrows in Fig. 2.4.5(a)). Those peak values at a specific heat sink temperature are shown again in Fig. 2.4.5(b) vs. the corresponding dissipated power. Figure 2.4.5(b) also demonstrates the evaluation result of equation (2.24), where the slope of the parallel lines is $d\lambda/dP_{diss}$. Here a R_{th} value of about 7.6 K/W and a $d\lambda/dT$ value of about 0.16 nm/K were achieved, which is typical for such kind of lasers on C-mount. The value of $d\lambda/dT$ is usually fixed for lasers with the same epitaxy design.
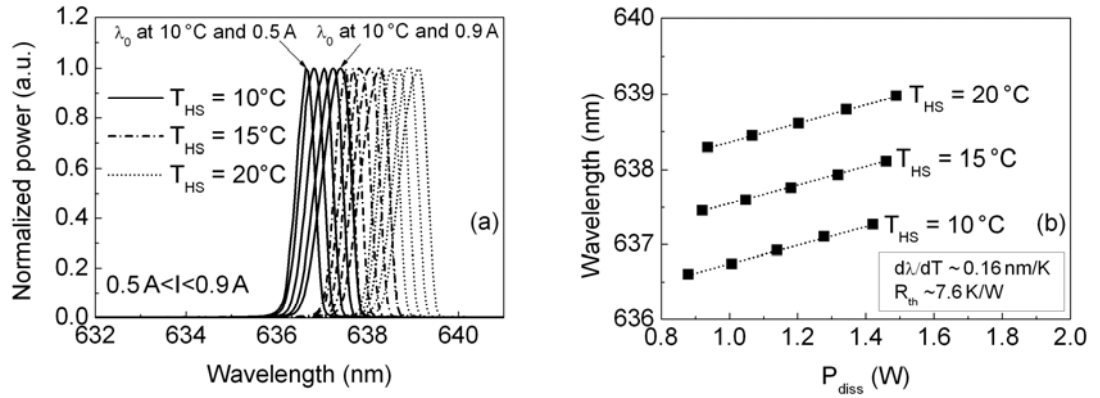
Fig. 2.4.5. (a) Spectra of the same standard 638 nm AlGaInP BA laser on C-mount characterized in section 2.4.4 for different T_{HS}. (b) Wavelength vs. P_{diss} for different T_{HS} for evaluating equation (2.24), i.e., extracting the values of $d\lambda/dT$ and R_{th}.

2.4.6 Spatial emission

Spatial emission in semiconductor lasers is usually divided into two optical field regions: near-field (NF) and far-field (FF). The optical field profile present just outside the facet of the laser is denoted as the optical NF. The waveguide mode emitted into free space undergoes diffraction. For distances $> w^2/\lambda$, where w is an effective full width of the near-field, one speaks of optical FF. The FF is usually described by the optical intensity as a function of angles Θ_x and Θ_y as illustrated, e.g. for a BA laser, in Fig. 2.4.6. The intensity is suitably calculated in the Fraunhofer approximation as [28]

$$I(\Theta_x) \propto \cos^2 \Theta_x \left| \int_{-\infty}^{\infty} E(x) e^{ik \sin \Theta_x x} dx \right|^2 \tag{2.25}$$

where E(x) is the electric field profile of the guided mode and $k = 2\pi/\lambda$. An equivalent equation holds for I(Θ_y). For small angles Θ_x, equation (2.25) corresponds to a Fourier transform. Consequently, it is easily understood that a narrow NF will result in a highly divergent FF and vice versa. Since the NF extends more in the y-direction but is rather narrow in the x-direction, the FF angles of a regular edge emitting laser usually satisfy $\Theta_x > \Theta_y$, as shown in Fig. 2.4.6 [28]. In general, the far-field is evaluated at the point where the intensity has dropped to one-half of its maximum, called FWHM (full width at half-maximum). For some applications, the full FF angle is evaluated at an intensity drop of $1/e^2$ instead at the FWHM.
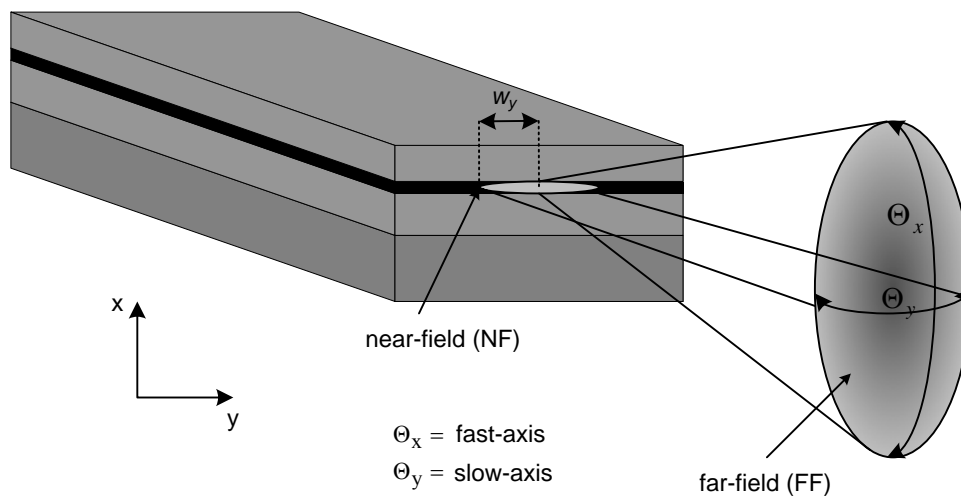
Fig. 2.4.6. Spatial emission of a BA semiconductor laser showing the transition from the optical near-field E(x,y) at the laser facet to the far-field intensity pattern in free space I(Θ_x, Θ_y).

NF measurements reveal for example if the output facet has defects, if the output light is homogeneous and how strong filamentation in multimode lasers is. The knowledge of FF data is important for example when coupling the laser emission to an optical fiber or for the determination of the lens parameters when light collimation is required. Single mode ridge lasers, for example, are coupled to single mode fibers. FF measurements can reveal if the ridge is really single mode or if there are any parasitic effects from higher order modes. BA lasers, on the other hand, usually have a multimode slow-axis FF and can for example be coupled into multimode fibers.

NF measurements are typically done using a microscope objective and a CCD camera as shown in Fig. 2.4.7(a) and FF measurements are best done with a rotating photodiode as displayed in Fig. 2.4.7(b).
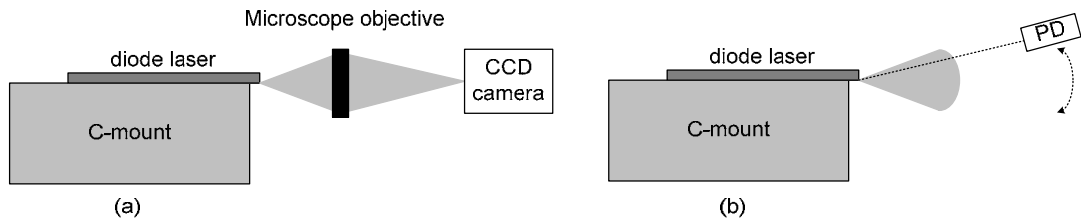
Fig. 2.4.7. (a) NF and (b) FF measurement techniques. PD = photodiode.

Figure 2.4.8 (a) shows a NF line scan measurement and emission capture of a standard 650 nm AlGaInP BA laser on C-mount at I = 1 A in pulse mode (pulse width: 1 μs, pulse frequency 10 kHz). The peaks in the NF intensity are due to filamentation, which is typical for BA lasers. Filamentation can occur due to changes in the carrier density, which affect both the optical gain and the refractive index seen by the intracavity field, or to fluctuations in the cavity due to externally induced inhomogeneities or voids, such as thermal inhomogeneities at nonradiative defects (see chapter 5). Figure 2.4.8(b) shows a FF measurement of the same laser and for the same current conditions. Here both the fast- and slow-axis are displayed. Indicated also is where the FWHM and $1/e^2$ angles can be extracted.
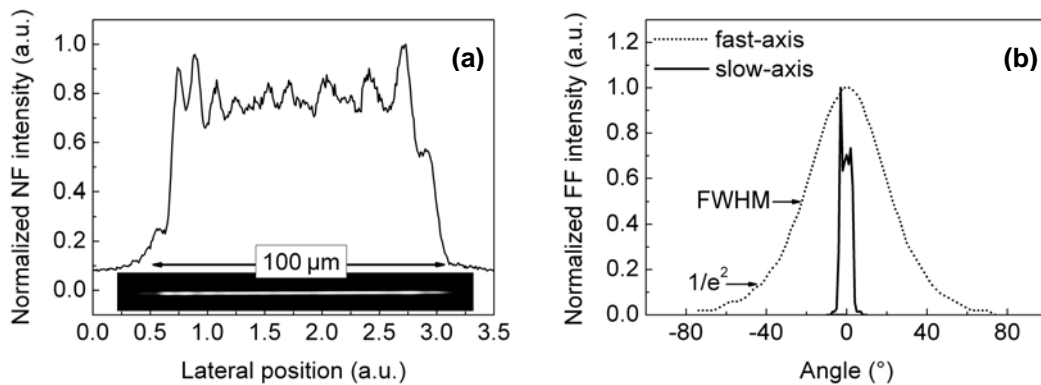
Fig. 2.4.8. (a) Normalized NF intensity measurement and lasing emission image of a standard 650 nm AlGaInP BA laser on C-mount at I = 1 A in pulse mode (pulse width: 1 μs, pulse frequency 10 kHz). (b) Normalized FF intensity measurements for slow- and fast-axis of the same laser. Indicated by arrows is where the FWHM and the $1/e^2$ angles can be extracted.

2.4.7 Internal parameters of edge-emitting lasers

As discussed in section 2.4.2, the intrinsic loss coefficient α_i is mainly due to free-carrier absorption and the injection current efficiency η_i is present due to the fact that not all injected carriers might end up in the QWs. The values of α_i and η_i can be deduced from the differential quantum efficiency of lasers having different lengths L from the same material and with the same mirror reflectivities according to equation (2.17). For a minimum of two lasers with length L and L_1, equation (2.17) gives two

equations with two unknowns resulting in the values of α_i and η_i. However, practically and for more reliability, it is generally better to plot a number of data points on a graph and determine the unknowns by fitting a curve to the data. Usually, it is most convenient to plot the reciprocal of the measured differential efficiencies vs. L. Then a straight line through the data has a slope and intercept for which α_i and η_i can be determined according to equation (2.26) as **[29]**

$$\frac{1}{\eta_d} = \frac{1}{\eta_i}\left(1 + \frac{\alpha_i}{\alpha_m}\right) \tag{2.26}$$

with $\alpha_m = \dfrac{1}{2L}\ln\left(\dfrac{1}{R_1 R_2}\right)$ representing the mirrors loss. Thus the intercept at L = 0

gives η_i, and this can be used in the slope to get α_i. Figure 2.4.9 shows such data taken from unmounted 638 nm AlGaInP 60 µm BA lasers having resonator lengths between 900 and 1800 µm. The measurements are done in pulse mode in order to avoid self-heating of the lasers. This resulted in α_i and η_i values of 3 cm^{-1} and 54.3 % respectively.
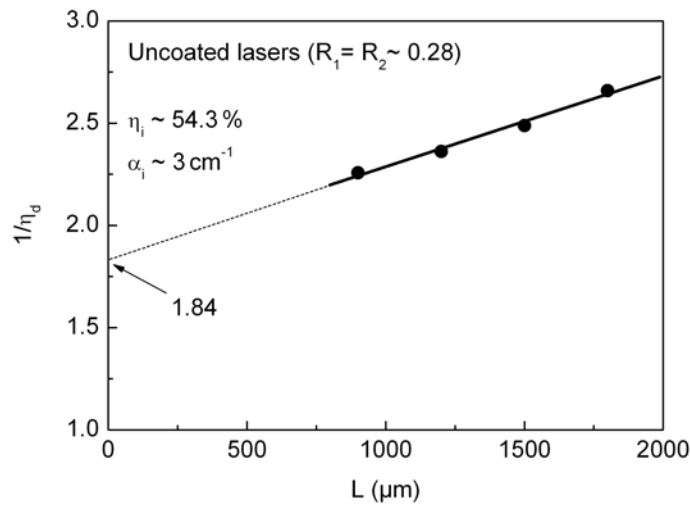
Fig. 2.4.9. A linear plot of the inverse differential efficiency vs. the cavity length L. Since the facets of the devices are uncoated, facet reflectivities are $R_1 = R_2 \approx 0.28$.

Chapter 3

Introduction to degradation mechanisms

Whether used as a simple laser pointer or as a medically qualified PDT light source, commercial semiconductor lasers have a common critical issue: reliability. Developing a robust manufacturing process that consistently produces reliable devices is essential for the commercial success of a device manufacturer. The reliability of semiconductor lasers has been in constant improvement for about four decades, since cw lasing at room temperature was achieved in AlGaAs/GaAs lasers. Especially in high-power lasers, where high dissipated power in form of heat has to be dealt with, improving the reliability of laser devices is of great importance. In this chapter, different laser lifetime testing principles and the fabrication of a lifetime testing facility to study the degradation mechanisms in AlGaInP lasers is presented. Moreover, the major aging effects in high-power AlGaInP lasers and their influence on reliability are discussed.

3.1 Lifetime testing principles

Degradation in laser diodes is substantially different from that in other electronic devices due to the recombination process of electron-hole pairs and the presence of high optical power densities within the active region and at the output facets of the laser [34]. In general, laser diode reliability may be defined as *"the ability to operate the device satisfactorily in a defined environment for a specified period of time"* [35]. From a laser user's point of view, many of the issues related to laser diode reliability are revealed by the hazard rate for a population of lasers, as shown in Fig. 3.1.1 [35][36].

Fig. 3.1.1. Hazard rate for unscreened laser components [35].

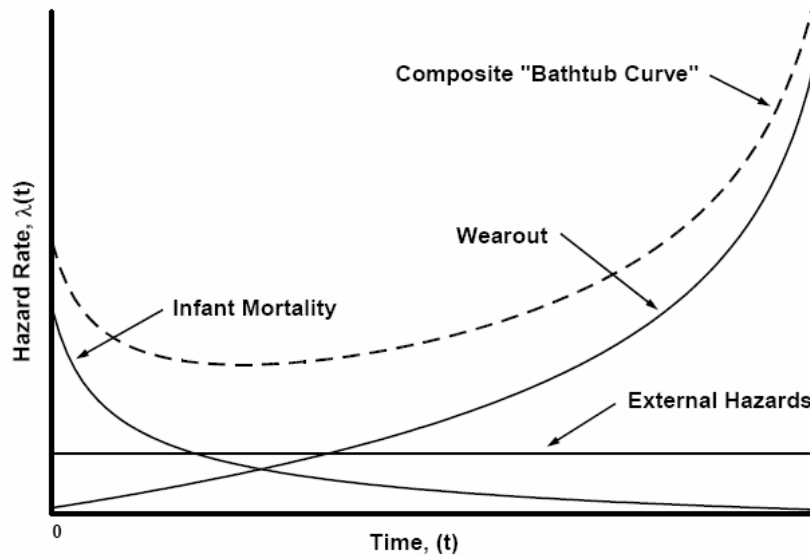Hazard rate $\lambda(t)$ is defined as the probability of failure per unit time, at time t, given that the device has survived until time t. Infant mortality failures are often caused by defects introduced during the manufacturing process or by intrinsic semiconductor defects. External factors such as current surges and ESD events create a constant hazard rate over the life of the device. Finally, wearout failures in lasers are generally found to be caused by the growth of nonradiative recombination centers within the active region of the laser, which leads to light absorption and increased dissipated power **[35][36]**. Additionally, facet degradation is one of the major aging effects in high-power edge-emitting lasers. Facet degradation can be induced by mechanical defects due to cleaving, by oxidation, and by absorption and nonradiative surface recombination. So depending on the facet treatment used (see chapter 6), facet degradation induced aging may either lead to infant mortality, for example due to a sudden COD, or to wearout due to increased nonradiative defects near the facets or to gradual oxidation.

Laser lifetime is affected by operating conditions such as injection current, optical output power, and temperature. Depending on the type and application of the laser diode, lifetime test studies involve the periodic measurement of a variety of device parameters including operating current, optical output power, threshold current, and forward voltage under accelerated aging conditions. Accelerated aging may be implemented through high temperature, injection current or optical power; however, temperature acceleration is the most common. Aging studies are conducted in one of the following three modes of operation **[34][35]**:

Constant Current aging – Often referred to as automatic current control (ACC) mode. In this mode, laser current is held constant for the duration of the test, and the changes in P_{OUT} are evaluated.

Constant Power aging – Often referred to as automatic power control (APC) mode. Here, laser output power is held constant by continuously adjusting current as required to maintain constant output power, and the changes in current are evaluated.

Periodic sample testing – In case where lasers are to be aged at temperatures above approximately 100 °C, lasing action is not present and it is necessary to periodically reduce the temperature of the laser to a lower measurement temperature. In this type of test, lasers are operated in constant current mode during the high temperature aging. This method is however less common than both aging methods mentioned above.

In order to obtain statistically meaningful data, lifetime test studies normally involve dozens of lasers monitored for periods of at least 1000 hours and often these test studies extend over a year in length. The lifetime of a device is usually empirically related to temperature through the Arrhenius equation **[34]**

$$Lifetime = A_t e^{(E_a/k_B T)} \tag{3.1}$$

where A_t is a constant, E_a [eV] is the thermal activation energy, $k_B = 0.862.10^{-4}$ eV/K is the Boltzmann's constant, and T [K] is the temperature. E_a can be estimated by varying the aging temperature (more than three levels) if other stresses are constant; that is A_t is constant. Depending on the laser's type and on the predominating degradation process, typical E_a values range between 0.2 to 0.7 eV **[35]**. If two or more types of degradation phenomena are taking place, this relationship cannot be applied to estimate the lifetime.

When the lasers' lifetime extends over many thousand hours, it makes sense to perform accelerated aging and extrapolate the data over many years. Since semiconductor lasers cannot be repaired after failure, the time at which the device fails after starting to operate indicates device lifetime, and is called time to failure (TTF). The mean value of TTF is mean time to failure (MTTF), and is generally used to characterize a device's lifetime. Different statistical models can be found in literature to estimate MTTF **[34][36]**.

The value of MTTF is important for commercial lasers and can usually be found in the device's datasheet, so the buyers can get estimation about the devices' lifetime. For research purposes, however, it is more important to look at the TTF data of devices in order understand the degradation mechanisms. Additionally, such aging data are essential when comparing different epitaxy designs to each other. In this study, only real degradation curves are analyzed.

3.2 Lifetime testing facility

A lifetime testing facility was developed during this study to investigate aging phenomena in high-power AlGaInP diode lasers. The facility can handle different kinds of laser designs, as long as their anode is bonded to a C-mount base. Studying single emitters on C-mount is as a start sufficient to tell about the reliability and to understand the degradation mechanisms of a certain laser design. This is especially true when comparing the influence of different design parameters to each other, such as epitaxy, doping, facet coating material, etc. After investigating single emitters of a certain epitaxy design, investigating the degradation of for example high-power laser bars on Sirilas® of the same epitaxy should be additionally performed. This is due to the additional stress effects that may occur for example due to the different heat-sink design, mounting inhomogeneities, and the heat interchange between emitters in a bar.

The lifetime testing facility was designed as follows:

- Constant current aging (ACC mode, with maximal $2.5\,A \pm 20\,mA$ aging current)
- Aging temperature controllable between -25 to $125\,°C$ ($\pm 1\,°C$)
- Simultaneous aging of maximum 10 devices with separate current control (which means one or more laser breakdown will not influence the others or the process)
- All input parameters (temperature, aging current, intervals, etc…) are software controlled.
- All output parameters (P_{OUT}, PIV-curves, actual temperature, etc…) are monitored and automatically saved during the process (online measurement).
- PIV-measurements can be evaluated during user defined intervals within the total aging period.
- Aging period can be changed without stopping the process.
- Aging input parameters can be changed without stopping the process.

Figure 3.2.1 illustrates the lifetime testing facility system. The heart of the facility lies in the laser carrier plate design. The plate is cooled down with a liquid which is pumped at a maximum pressure of about 3 bars from a liquid cooling system in order to maintain a constant temperature during the aging process. The C-mount lasers can be mounted on the cooling plate. The base of the cooling plate represents electric ground, and the laser n-side (metal stripe) can then be individually triggered with a negative current between 0 and $-2.5\,A$. Figure 3.2.2 displays the cooling plate design schematic. Large area silicon PDs with an area of $1\,cm^2$ are placed in close vicinity of the lasers in order to measure the relative P_{OUT}. Neutral density (ND) filters are fitted

between the lasers and the PDs, in order to reduce the high-power density on the latter and prevent them from being destroyed. Finally, the measurement data are saved as ASCII and can be evaluated using any spreadsheet program. Figure 3.2.3(a) shows the dissembled laser carrier plate uncovering the ND filters and the PDs plates. Figure 3.2.3(b) displays the finished and closed laser carrier plate.

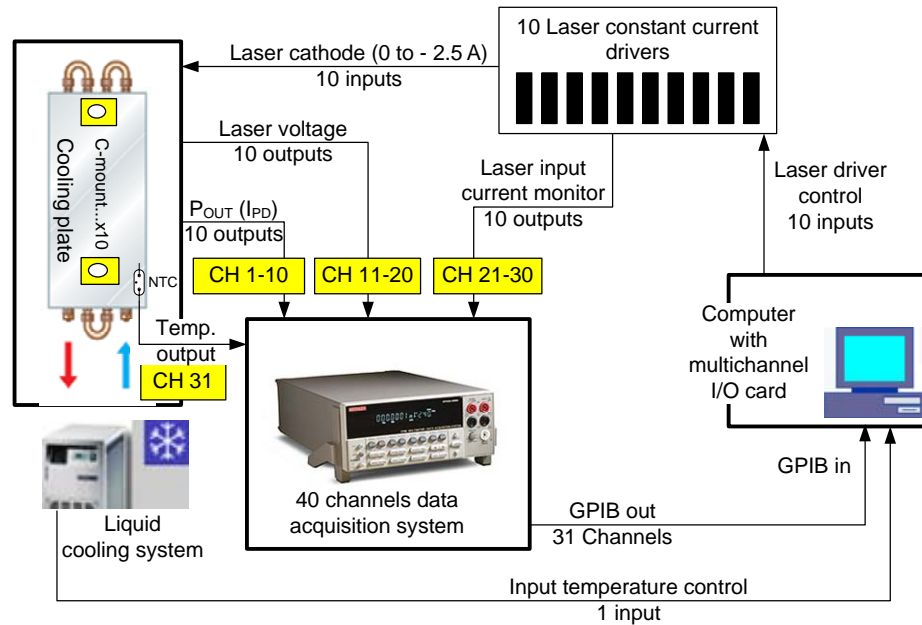
Fig. 3.2.1. Laser lifetime testing facility system. I_{PD} = photodiode current. CH = channel. GPIB = General Purpose Interface Bus. I/O = input/output.
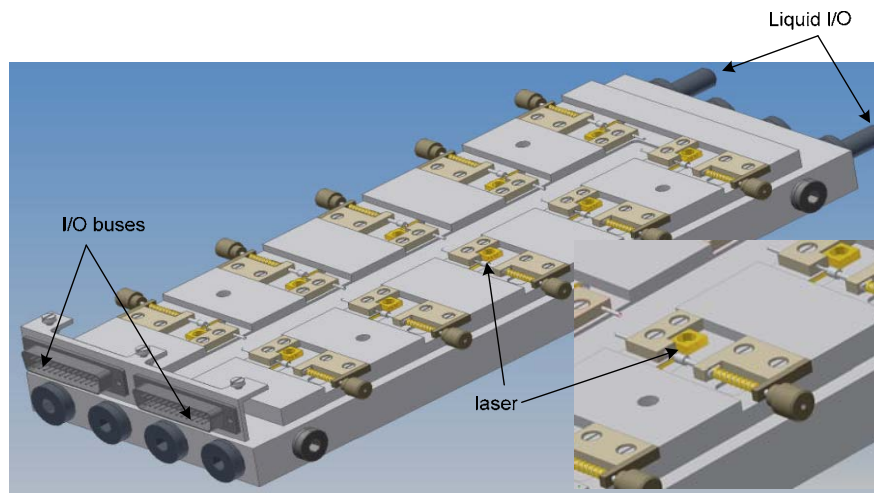

Fig. 3.2.2. 3-dimensional view of the cooling plate design (with magnification).
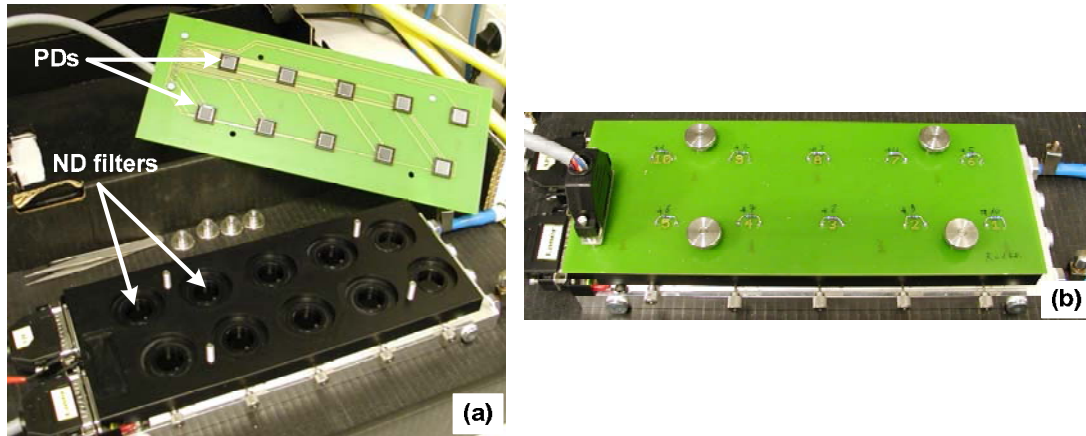
Fig. 3.2.3. (a) Dissembled carrier plate uncovering the ND filters and PDs plates. (b) Finished and closed laser carrier plate.

3.3 Degradation phenomena in high-power AlGaInP lasers

During the operation of optical devices, the output power under a constant injection current or the injection current under a constant output power changes. There are several types of degradation modes related to this change and can be classified as follows: (i) burn-in, (ii) gradual degradation, (iii) rapid degradation, (iv) catastrophic optical damage, and (v) spontaneous breakdown. In this study a decrease in laser performance during operation, such as in output power under ACC mode, will be described as negative aging, and an improvement in performance during operation as positive aging.

3.3.1 Burn-in

Burn-in is defined as the initial stage of device aging under accelerated aging mode. In high-power diode lasers, high temperature and high injection current (or optical power) burn-in screening is used to screen out devices that are likely to have unacceptably short lives and to ensure that the remaining population of lasers will have a statistically acceptable level of reliability. Due to the impact of burn-in on manufacturing cost and cycle times, burn-in times of less than 100 hours are common.

Burn-in temperature and injection current should be high to minimize burn-in time, yet not so high that a degradation mode is triggered that is not present under normal operating conditions for screened parts. Selection of burn-in conditions and screening criteria varies significantly with the type of laser and can be quite complex **[35]**.

In general, burn-in is done in cw mode, in order to get a real aging behavior including the influence of the internal heating of the laser. Figure 3.3.1(a) shows burn-in test results of 650 nm standard AlGaInP BA lasers. The burn-in was performed in ACC mode at I = 1.2 A cw and T = 40 °C, for 72 h. A 20 % P_{OUT} decrease is typical for such type of lasers at such aging conditions.

The strong P_{OUT} decrease in the first few hours is usually associated with increased nonradiative centers in the active region and in the vicinity of the output facet. Also in this period, the p-dopant diffusion into the active region may also lead to negative aging. Other effects such as impurity incorporation, especially oxygen in Al-rich layers, may drastically affect the aging.

On the other hand, burn-in does not always lead to negative aging. Positive aging can also occur in AlGaInP lasers as shown in Fig. 3.3.3(b), where lasers belonging to another epitaxy design (design 2) were aged for the same burn-in conditions, leading to almost the same P_{OUT}, i.e. almost the same optical stress. The major difference between the two designs is the p-doping profile. In design 1, the p-setback, which is the distance from the active region layer to the p-dopant, is a bit smaller. The smaller the p-setback is, the higher the chance that the p-dopant diffuses into the active layers, which leads to increased nonradiative recombination centers and explains the negative aging in design 1. However, it is unclear what really caused the positive aging in design 2.
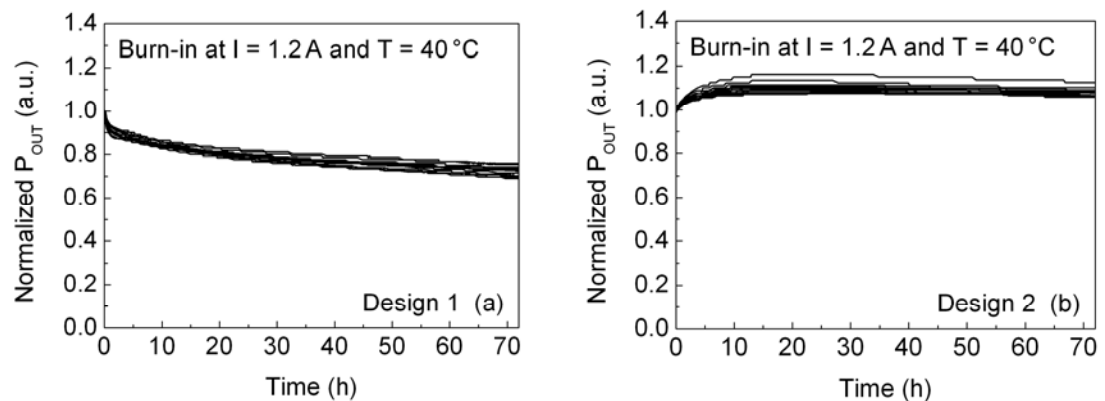
Fig. 3.3.1. (a) Burn-in test results of standard 650 nm AlGaInP BA lasers that showed negative burn-in. (b) Burn-in test results of standard 650 nm AlGaInP BA lasers that showed positive burn-in. In both cases, the burn-in was performed at I = 1.2 A cw and T = 40 °C, for 72 h.

Positive aging is as undesired as negative aging. One cause for positive aging was found to be the reduction of carrier leakage during operation, which is usually associated with an improvement in the p-side layers or in the p-side AlGaInP barrier [37]. For example, this improvement can be due to the p-dopant atoms spreading homogeneously during operation thereby reducing vacancies. Another reason for positive

aging may be the reduction of nonradiative recombination, i.e. nonradiative centers healing by the p-dopant during operation in the p-side layers. This reduction of non-radiative centers means that fewer carriers can escape and nonradiatively recombine at those centers leading to a total improvement in P_{OUT}. This effect is illustrated in Fig. 3.3.2. The difficulty in investigating the positive aging effect is that it is not always reproducible, even for slightly different growth conditions.

Fig. 3.3.2. Band diagrams of a QW laser illustrating the effect of reduced nonradiative centers in the p-side layers. In (a) is the case where many nonradiative centers are present in the p-side layers provoking more nonradiative recombination to occur there and hence more leakage. In 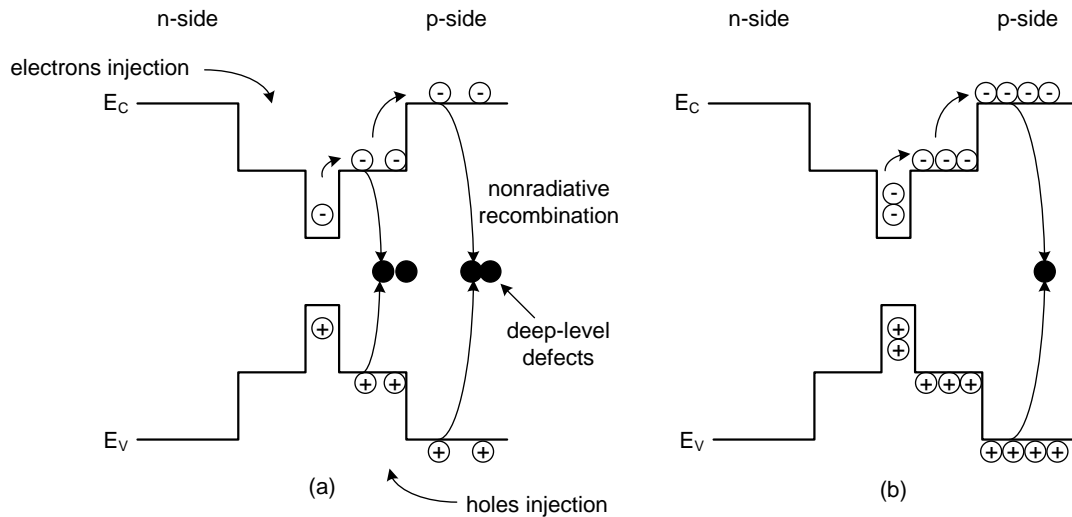(b) is the case where fewer (or healed) nonradiative centers are present leading to less nonradiative recombination and thereby less leakage.

3.3.2 Gradual degradation

Gradual degradation is defined as the slow degradation in a device operating parameters including I_{th}, η_{slope}, and P_{OUT}. After burn-in, the lasers are aged at less severe conditions for about 1000 h, usually at normal operation conditions. The aging temperature is normally chosen to be around room temperature. Under those conditions, good-quality lasers are either stable or undergo only a small negative aging. Looking at Fig. 3.3.1(b), it can be noticed that the lasers aged positively in the first 40 hours burn-in, but after that saw a slight negative aging. This negative aging is usually associated with an increase in nonradiative recombination centers in the active region during aging [38], and is often superimposed by facets degradation. Facet degradation means that additional absorption near the facet regions is present due enhanced nonradiative carrier recombination there, for example at surface states or due to oxide growth after cleaving [39]. During operation, this negative aging compensates and dominates the positive aging effect. For example, aging data of 5 standard 650 nm AlGaInP BA lasers are demonstrated in Fig. 3.3.3. The aging was performed in ACC mode at I = 1 A cw and T = 20 °C for 850 h.
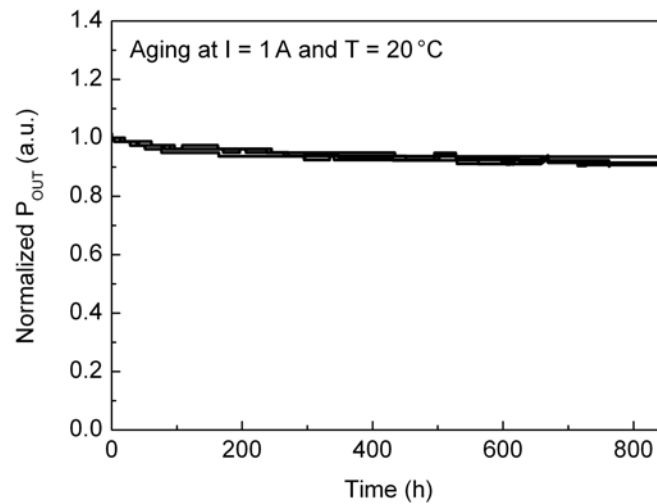
Fig. 3.3.3. Aging test results of standard 650 nm AlGaInP BA lasers. Aging was performed at I = 1 A cw and T = 20°C for 850 h.

Looking at aging data such as in Fig. 3.3.3, it can be seen that P_{OUT} decreased by about 10 % after 850 h. Nevertheless, evaluating only the P_{OUT} data does not tell if aging is due to degradation in η_{slope}, I_{th}, or in both. In order to estimate the change in I_{th}, η_{slope}, and P_{OUT}, temperature dependent pulse measurements in analogy to section 2.4.4 should be performed.

Figure 3.3.4(a) shows PI-curves of a 650 nm standard AlGaInP BA laser mounted on a C-mount for different T_{HS}. The measurements were made in pulse mode (pulse width: 1 μs, pulse frequency 10 kHz) to avoid self heating of the laser. Figure 3.3.4(b) demonstrates how I_{th} and η_{slope} change with T_{HS} for the same laser. The laser was measured in three phases: unaged, after 72 h burn-in at I = 1.2 A cw and T = 40 °C, and after 1000 h aging at I = 1 A cw and T = 20 °C.

Figure 3.3.4(b) shows the change in I_{th} and η_{slope} with T_{HS} for all three aging phases. Those measurements reveal that the aging did not affect I_{th} much, as all three corresponding fit-curves for the three phases almost lie on top of each other. On the other hand, looking at the η_{slope} fit-curves, it can be seen that η_{slope} decreased for about 10% (and with it P_{OUT}) after burn-in, and stayed almost stable for the following 1000 h aging.
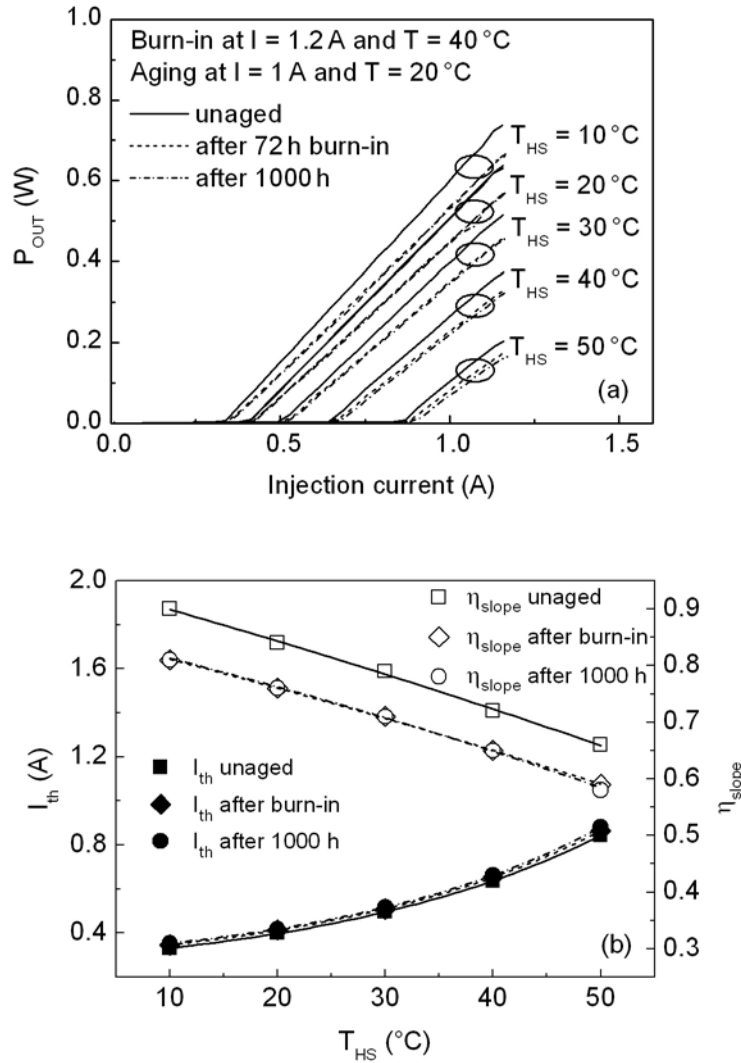
Fig. 3.3.4. (a) PI-curves of a standard 650 nm AlGaInP BA laser mounted on a C-mount for different T_{HS} in pulse mode (pulse width: 1 μs, pulse frequency 10 kHz). (b) Change in I_{th} and η_{slope} with T_{HS} for the same laser. Measurements were performed for the following phases: unaged, after 72 h burn-in at I = 1.2 A cw and T = 40 °C, and after 1000 h aging at I = 1 A cw and T = 20 °C.

Usually, such measurements can help evaluate the aging mechanisms of a laser. Looking at equations (2.15) and (2.18), j_{th} is linearly proportional to $1/\eta_i$ and $1/\tau_s$ and exponentially proportional to α_m and α_i. η_{slope} is linearly proportional to η_i, $1/\alpha_i$ and depends to a lesser extent on α_m, because α_m comes in both the numerator and the denominator of equation (2.18). In general, the mirror reflectivities do not change during aging; however, external effects such as increased moisture or dust accumulation on the laser facet can cause a minor change in the reflectivities.

Since several parameters may change during aging, it is difficult to guess just by looking at equations (2.15) and (2.18) which parameter mostly changed. For that reason, a simulation based on those equations was made to help understand what happens during aging. In the example demonstrated in Fig. 3.3.4, I_{th} increased minimally

during aging, and η_{slope} decreased by about 10%. From the simulation, and as shown in Fig. 3.3.5(a), it was found that this decrease in η_{slope} cannot be due to a large increase in the injection current efficiency η_i, which means an increase of carrier leakage, since this would have also strongly affected I_{th}. Concerning α_m, even a relatively large change in the reflectivities only causes a minimal change in both I_{th} and η_{slope}. On top of that, when α_m increases or decreases, both I_{th} and η_{slope} decrease or increase respectively. As I_{th} and η_{slope} increase or decrease together with a changing α_m, this does not simulate a real negative aging situation where I_{th} increase and η_{slope} decrease. On the other hand, and as demonstrated in Fig. 3.3.5(b), if the absorption parameter α_i increases, most of the change will affect η_{slope}. This means that in the example shown in Fig. 3.3.4, most of the aging in P_{OUT} was due to an increase in absorption.
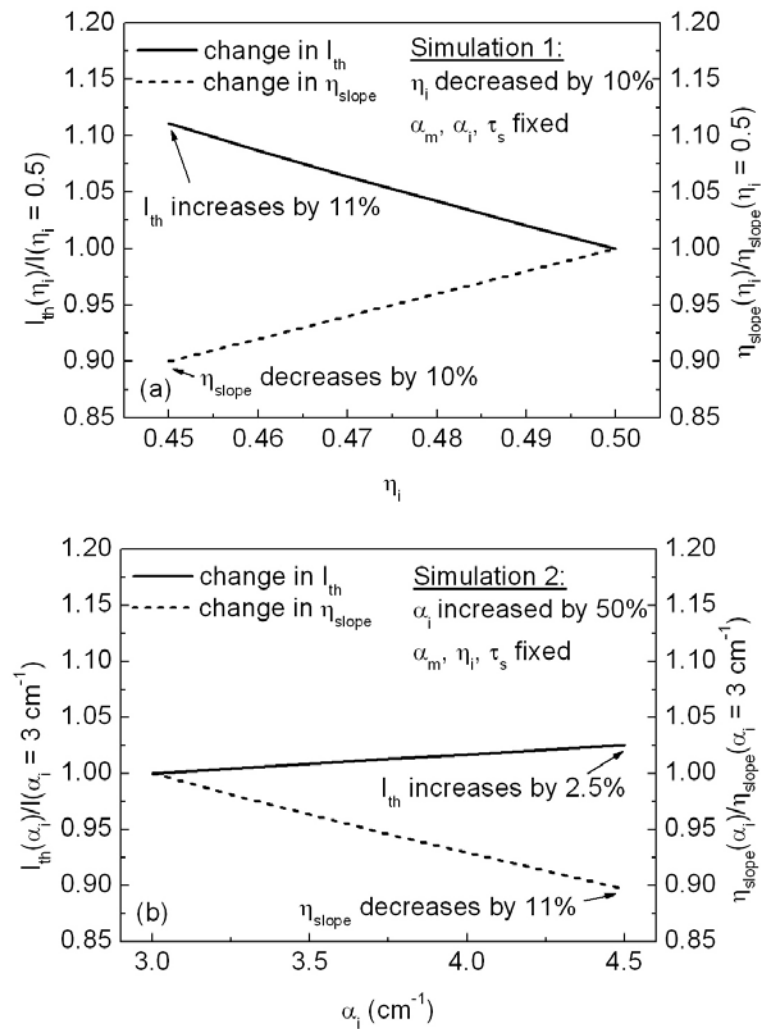

Fig. 3.3.5. Simulation results based on equations (2.15) and (2.18) of a standard 650 nm BA AlGaInP laser showing the effect of: (a) a 10% decrease in the injection current efficiency η_i and (b) a 50% increase in the absorption parameter α_i on the threshold current I_{th} and the slope efficiency η_{slope}.

The absorption parameter α_i is the sum of free carrier loss and waveguide mode loss. A change in α_i can be due to increased free carrier absorption in the cladding and/or waveguide layers due to an increase in defects or to a change in the doping profiles after aging in those layers. However, additional absorption near the facet region due for example to increased nonradiative carrier recombination there will also lead to an increase in the total absorption profile and add up to α_i.
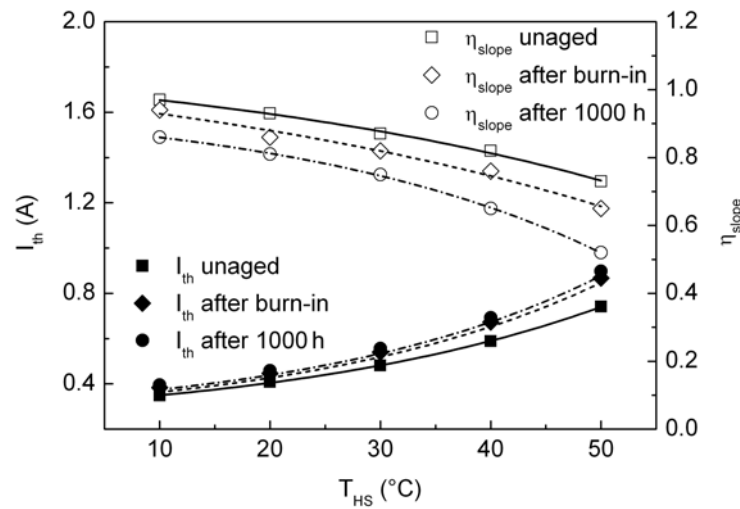

Fig. 3.3.6. Aging results of a 635 nm standard AlGaInP BA laser for the following phases: unaged, after 72 h burn-in at I = 1 A cw and T = 40 °C, and after 1000 h aging at I = 0.7 A cw and T = 20 °C.

In general, both j_{th} and η_i degrade after aging, which makes it more difficult to estimate the cause of degradation, i.e. the single dependence on η_i, α_i, τ_s, and to a lesser extent α_m. Figure 3.3.6 shows I_{th} and η_{slope} data vs. T_{HS} before and after aging for a 635 nm standard AlGaInP BA laser aged for 72 h burn-in at I = 1 A cw and T = 40 °C, and for another 1000 h at I = 0.7 A cw and T = 20 °C. Here, both I_{th} and η_{slope} degraded after aging, which can be due to a combination of changes in η_i, α_i, τ_s, and α_m. Also, the laser shows relatively strong temperature sensitivity, which is in general the case for short-wavelength AlGaInP lasers due to their relatively shallower QWs, which makes them more vulnerable towards leakage. Moreover, compared to the laser shown in Fig. 3.3.4, η_{slope} degradation did not stop after burn-in (unlike I_{th}), but decreased further during the aging process. This also indicates, according to the simulation described in the previous example, that after burn-in the degradation was mainly caused by a change in α_i. On the other hand, the fact that I_{th} and η_{slope} show more change at high temperatures, means that leakage also played a role in aging.

Sometimes, if I_{th} increases without having a change in η_{slope}, the degradation is easily associated to a decrease in τ_s, which is due to an increase in the nonradiative recombination centers in the active region. This is however rarely the case.

3.3.3 Rapid degradation

Characteristic phenomena in rapid degradation are fast decrease in output power (in ACC mode) and formation of nonradiative regions. Rapid degradation is mostly due to external effects and processing failures, such as strong mirror oxidation, facets contamination, contact degradation, solder migration, etc. However, internal effects, such as strong p-dopant diffusion into the active region due to a bad setback design (which is the distance from the active region layer to the p-dopant), defect introduction during crystal growth, etc...can also cause rapid laser degradation. For example, aging data of 5 standard 650 nm AlGaInP BA lasers are displayed in Fig. 3.3.7. The aging was made in ACC mode at I = 1 A cw and T = 20 °C for about 600 h. No burn-in was performed prior to aging. Unlike the typical gradual degradation results illustrated in Fig. 3.3.7, P_{OUT} decreased by more than 80 % after around 40 h of aging. In this case, the degradation was due to strong p-dopant diffusion into the active region during aging, which was controlled afterwards by secondary ion mass spectroscopy (SIMS) measurements.
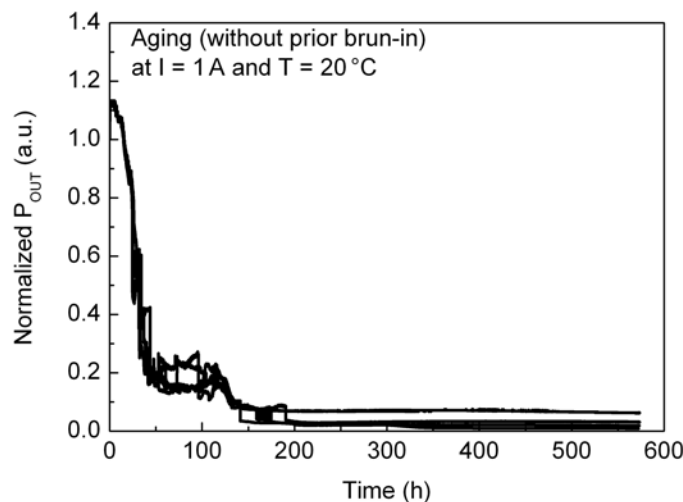
Fig. 3.3.7. Aging test results of standard 650 nm AlGaInP BA lasers that showed rapid degradation. Aging was made at I = 1 A cw and T = 20 °C for about 600 h. No burn-in was performed prior to aging.

3.3.4 Catastrophic optical damage (COD)

COD is characterized by a sudden drop in the output power at a certain maximum operation point. Figure 3.3.8 illustrates a typical PI-curve of a standard 650 nm AlGaInP BA laser that underwent a COD event. Unlike the rollover effect, COD causes irreversible laser destruction. Usually after a COD event only spontaneous emission is left, but sometimes, the COD effect can occur in several small steps before reaching total destruction where only spontaneous recombination can occur. P_{COD} repre-

sents P_{OUT} at COD, i.e. the maximum total output power reached by the laser before being destroyed.

COD is seeded by photon absorption near the facets regions and enhanced nonradiative recombination at surface states. In cleaved lasers, additional surface defects can arise due to oxide growth on the facets [39][40]. Enhanced nonradiative recombination and photon absorption lead to increased temperature near the facets regions, hence bandgap shrinkage and consequently increased absorption. This in turn increases temperature even more and finally leads back to increased absorption. At a certain critical temperature, a "thermal runaway" process provokes irreversible laser destruction.

COD sets the absolute limit to extract high power out of semiconductor edge-emitting lasers. In order to improve the COD level, it is vital to understand what mechanisms hide behind its cause. In the next chapters, complete characterization and understanding of the COD effect in AlGaInP lasers are presented.
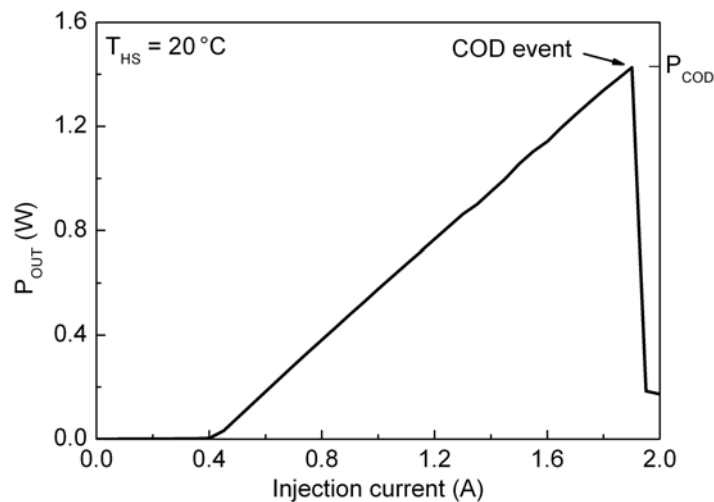
Fig. 3.3.8. Typical PI-curve of an AlGaInP BA laser that underwent a COD event. P_{COD} represents the output power at COD.

3.3.5 Spontaneous breakdown

Unlike slow and rapid degradation, spontaneous breakdown is characterized by a sudden drop in P_{OUT} anytime during lifetime testing. Similar to rapid degradation, spontaneous laser breakdown can be due to external effects, but sometimes, internal effects also come into play. It has been observed in [39] that the closer the aging current/power of the laser to its COD current/power limit is, the more likely and the faster spontaneous breakdown will take place during operation. Actually, spontaneous breakdown can be explained as a P_{COD} degradation due to total performance deg-

radation (except for positive aging), i.e. a COD that happens at much lower output powers than expected.
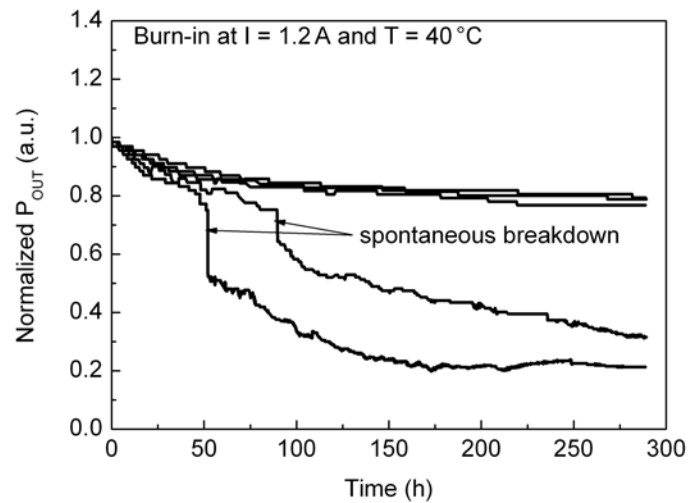
Fig. 3.3.9. Burn-in test results of 5 standard 635 nm AlGaInP BA lasers where 2 lasers underwent a spontaneous breakdown. Burn-in was performed at I = 1.2 A cw and T = 40 °C, for about 300h.

Figure 3.3.9 shows burn-in test results of 5 standard 635 nm AlGaInP BA lasers where 2 lasers underwent a spontaneous breakdown. In fact, the aging behavior of those 2 lasers was from the start worse than the others, which indicates that spontaneous breakdown may have happened here due to some external effects. The difference between the spontaneous breakdown induced defects and the COD induced defects will be depicted in chapter 4.

Chapter 4

Investigation of COD induced defects

This chapter presents detailed investigation of defects generated during COD in high-power AlGaInP lasers using microphotoluminescence (µPL) mapping, focused ion beam (FIB) microscopy, and deep-etching techniques. High-resolution µPL images demonstrated that during COD, nonradiative DLDs originate from the front mirror of the laser and propagate deep inside the cavity. Furthermore, FIB microscopy identified the epitaxial layers affected by COD, revealing that the DLDs are confined to the active region. In addition, deep-etching uncovered the DLDs by making them visible, and showed that they are composed of complex dislocation networks. Moreover, the difference between cw and pulsed mode COD is described. Lasers that underwent a spontaneous breakdown where also studied. In this study, different high-power laser designs were driven into COD for investigation, including BA lasers, laser bars, and tapered lasers. Additionally, a comparison to a tapered IR-emitter was performed.

4.1 Facet inspection

The first step in investigating the defects induced by COD is to inspect the laser facets. Visual inspection can be performed using an optical microscope and a scanning electron microscope (SEM) or a FIB microscope. Facet defects are best identified when observing the spontaneous emission of the active region, realized by driving the laser with very a small injection current. Figure 4.1.1 shows the electroluminescence (EL) of a good 650 nm AlGaInP BA laser mounted on a C-mount, with a 100 µm active stripe width. The mirrors of the lasers are coated with AR/HR coatings, so that most of the output power comes out of the AR facet. The AR mirror is coated with an Al_2O_3 layer with thickness ~ 145 nm, i.e. a reflectivity of ~ 18 %. Under

spontaneous emission, the entire active region emits light. The $100\,\mu m$ active width where lasing occurs can already be identified due to current confinement by gain guiding in BA lasers.

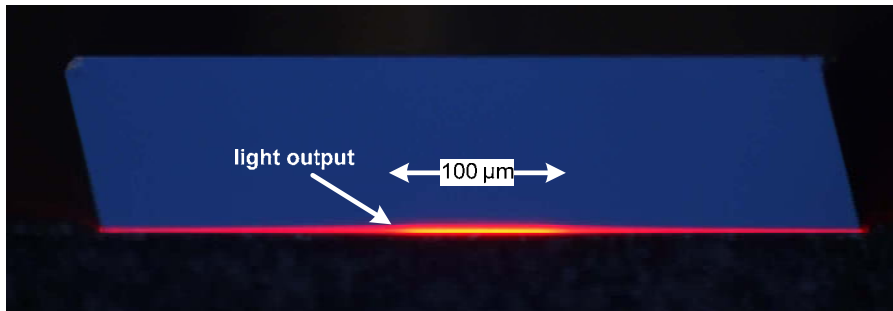**Fig. 4.1.1.** Electroluminescence from the output facet of a good AlGaInP BA laser. The active stripe width = $100\,\mu m$.

For this experiment, several lasers were intentionally driven at high injection currents to a point where a COD event occurred. Figure 4.1.2 shows EL from the output facet of 3 lasers (a), (b), and (c) that underwent a COD event. Looking at the EL of those lasers, dark spots could be identified in the lasing region. In laser (a), the COD induced 3 dark regions at different locations on the facet. In laser (b), the COD induced a small defect on the left side of the active stripe region and in laser (c) the COD induced one large dark region on the right side of the lasing stripe. In all the investigated lasers, the COD happened at the AR-coated output facet. The HR-coated back facet stayed intact.
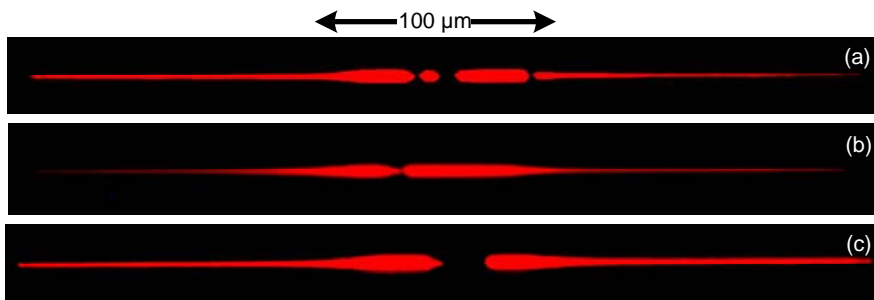
Fig. 4.1.2. Electroluminescence from the output facet of 3 COD driven AlGaInP BA laser. The active stripe width = $100\,\mu m$.

It is known from IR-emitters that a COD event causes visible damage in the AR-coating, where the effect looks like material explosion **[41]**. In AlGaInP lasers, however, no visible damage can usually be identified in the Al_2O_3 AR-coating after COD. In very few cases, visible deformation in the AR-coating can be spotted. Nevertheless, it is small compared to the damage caused on the facet of IR-emitters after COD. Figure 4.1.3 displays optical microscope and corresponding SEM images of an

AlGaInP broad-area laser where visible damage (elevation) on the AR-coating could be identified after COD.
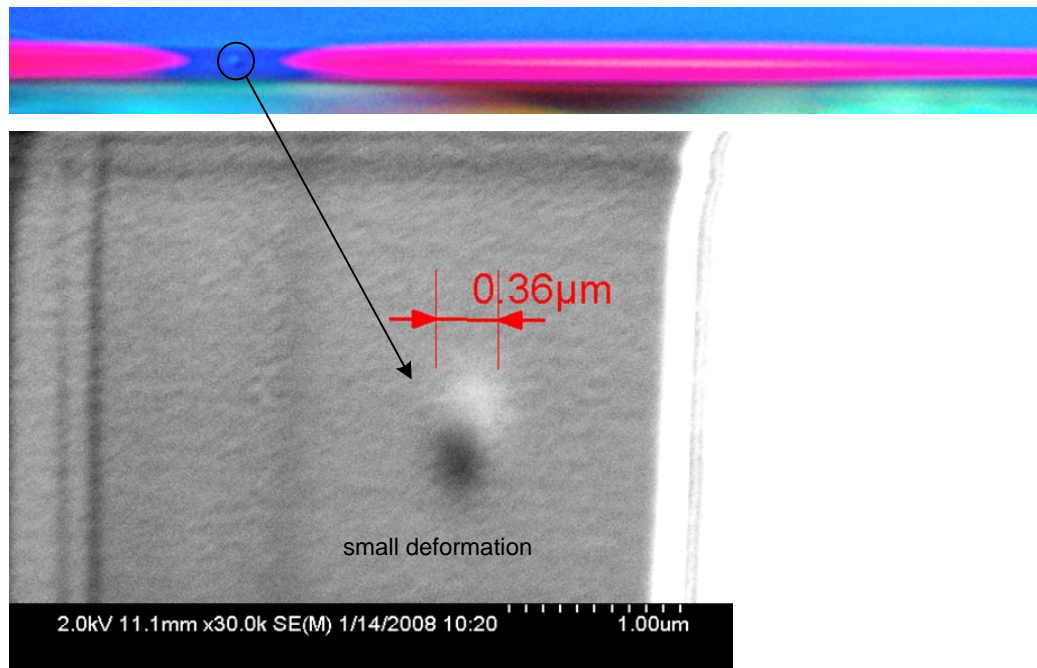
Fig. 4.1.3. Optical microscope and corresponding SEM images uncovering a small deformation in the AR-coating after COD.

4.2 Defect localization

4.2.1 Microphotoluminescence (µPL) mapping

Photoluminescence (PL) is one of many forms of luminescence and is distinguished by photon excitation. During photoluminescence, if the energy of the photons coming from the excitation source is greater than the energy gap of the semiconductor, the sample emits photons. One speaks of µPL when the spatial resolution of the excited area lies in the order of few micrometers.

The active region of degraded optical devices can be imaged by µPL mapping for defect study; the excitation source is usually a focused laser. In semiconductor technology, PL mapping is routinely used for defect investigation on wafers, since it is basically a nondestructive method.

The excitation laser penetration depth depends on its wavelength and on the refractive index of the material. In µPL, epitaxial layers with few µm thicknesses can normally be evaluated **[42]**.

4.2.2 Laser processing for the μPL mapping experiment

The amount of damage that occurs inside a resonator due to COD can be investigated using μPL mapping. A schematic representation of a μPL mapping measurement system is shown in Fig. 4.2.1. The excitation laser source used in this experiment is a 488 nm Ar^+-ion laser with output power < 1 mW. A spatial resolution of around 1 μm was reached using a 50× "long working distance" microscope objective. In order to obtain PL out of the active region of the AlGaInP lasers, the samples need to be carefully processed. First, in order to get a COD under cw operation, the test lasers need to be mounted (p-side down) on a C-mount and measured under a fixed heat-sink temperature so that P_{OUT} does not go into thermal rollover before COD. Second, the n-metallization must be removed and the light-absorbing relatively thick GaAs substrate selectively etched, so that the excitation laser light can penetrate into the active region.
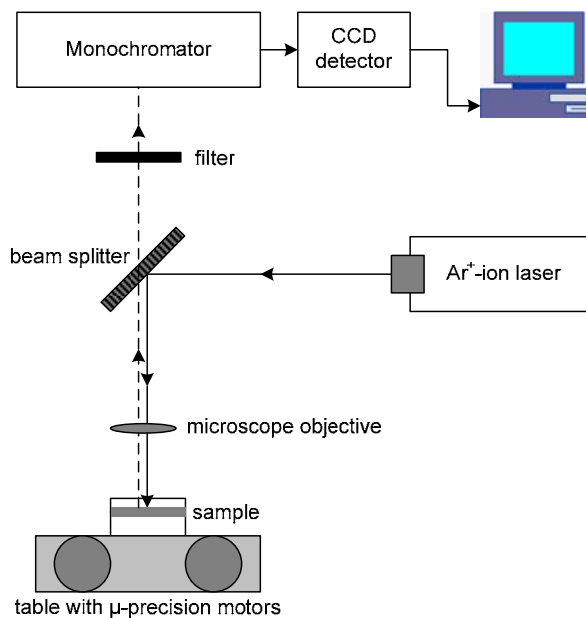
Fig. 4.2.1. A μPL mapping system.

The processing steps are illustrated in Fig. 4.2.2. The mechanical polishing of the n-metallization was performed manually using a fine rotating sandpaper (granularity = 4000). Afterwards, the sides of the epitaxy layers were protected with a resist in order to prevent under-etching of the p-GaAs cap layer, as will be shown e.g. in Fig. 4.2.4. Several experiment were tried to obtain a suitable etching solution, such as $H_2O:NH_3:H_2O_2$ (4:2:1) and $H_2SO_4: H_2O_2:H_2O$ (1:6:40), however, problems such as protecting resist etching or difficulty in controlling the etch rate led to unacceptable results. In the end, the $H_2SO_4:H_2O_2$ (4:1) solution was successful. This solution is exothermic and has a GaAs etch rate of about 10 μm/min (relatively fast). After etching the GaAs substrate, the resist is removed by acetone and isopropanol. Figure 4.2.3(a) shows an optical microscope top-view of a 650 nm standard AlGaInP BA

laser with etched GaAs substrate. The ~ 2 μm thick laser is still mounted on a C-mount and ready for the μPL mapping investigation. Figure 4.2.3(b) shows the epitaxial layers which are left after the GaAs substrate removal. Interestingly, the 10 μm wide active stripes in the GaAs cap become visible under the AlGaInP layers, since the thin AlGaInP material becomes partially transparent under white light illumination. Scanning the now exposed laser surface with 1 μm steps, achieved by μ-precision motors, and mapping the photoluminescence enables the observation of nonradiative defects in the device.
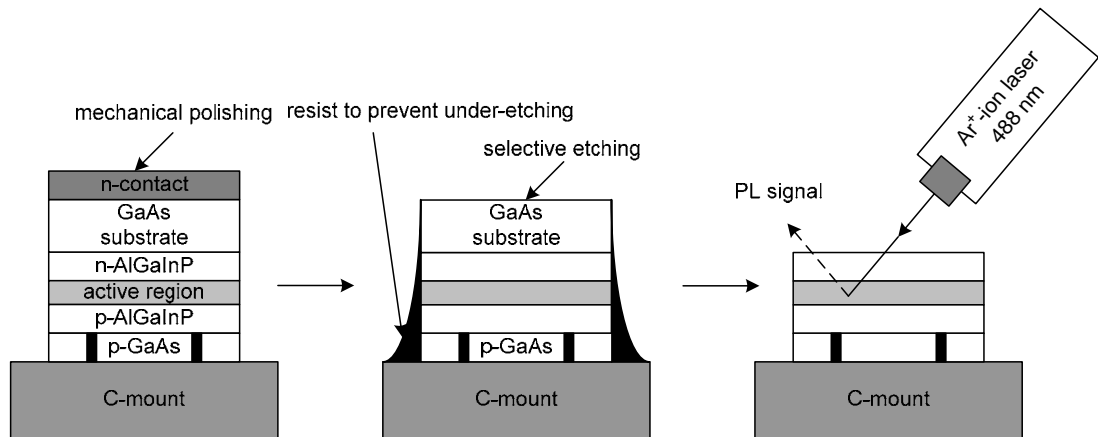

Fig. 4.2.2. AlGaInP lasers processing steps for the μ-PL experiment
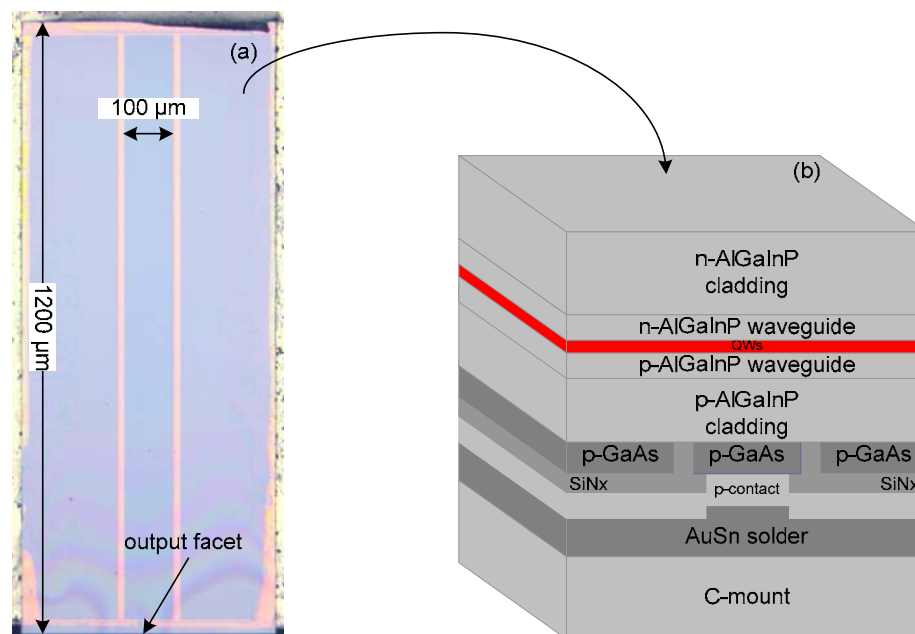

Fig. 4.2.3. (a) Optical microscope top-view of a 650 nm standard AlGaInP BA laser with etched GaAs substrate. The laser is mounted on a C-mount. (b) Remaining epitaxy layers after the GaAs substrate removal. Arrow points to the surface where image in (a) is taken.

4.2.3 µPL mapping results – AlGaInP BA lasers

Figure 4.2.4 shows the µPL mapping results of a reference 650 nm AlGaInP BA laser without COD. In order to check if any kind of nonradiative defects are present, other than COD induced defects, the laser was first aged for 1000 h. The substrate etching was performed in this case without a protecting resist, which led to underetching of the GaAs cap, however, the active zone between the stripes was not affected, because it is isolated from the rest.
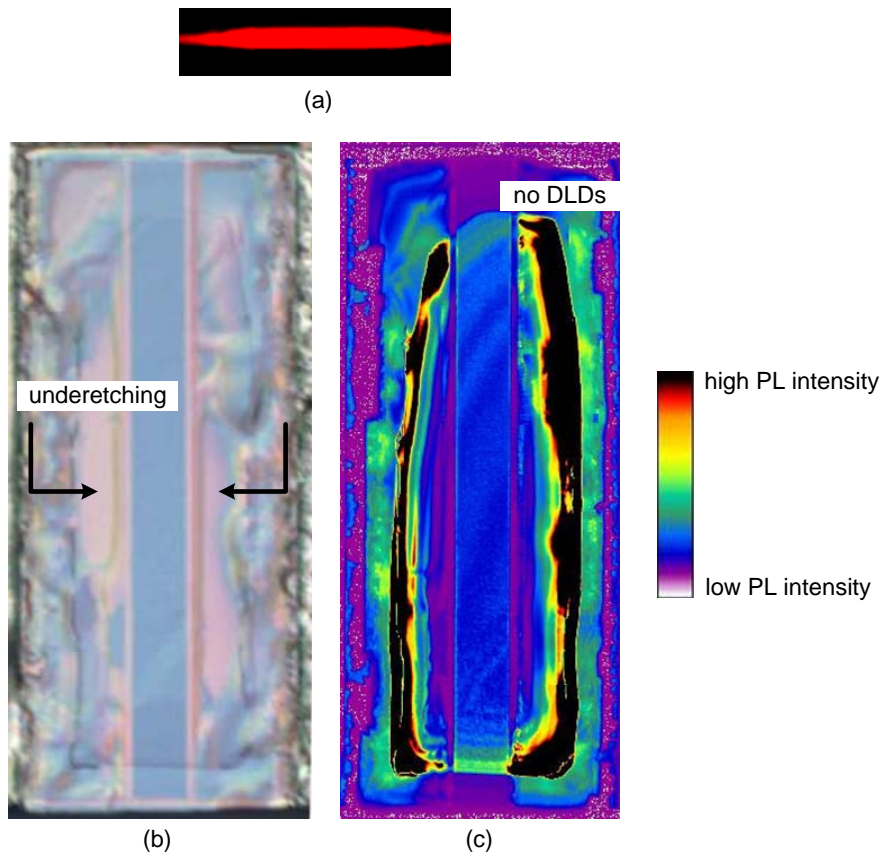
Fig. 4.2.4. Reference laser without COD. (a) EL from the output facet. (b) Optical microscope top-view after etching. (c) µPL mapping showing that no DLDs are present (black = high PL intensity, white = low PL intensity). The p-GaAs cap underetching effect can be seen in both images.

Figure 4.2.4(a) shows the EL taken before the laser preparation, 4.2.4(b) an optical microscope top-view image of the laser after the substrate and protecting resist removal, and 4.2.4(c) the µPL mapping of the whole laser area. The monochromator is set in a range around the PL wavelength of the active region, in order to suppress the PL emission of the other epitaxial layers. Due to inhomogeneities in the etching and to the GaAs cap underetching, the luminescence is also inhomogeneous, but still the results are sufficient to demonstrate that no nonradiative defects are present in the active area between the stripes. This will be clear when comparing the results to a laser with COD, as shown in Fig. 4.2.5.
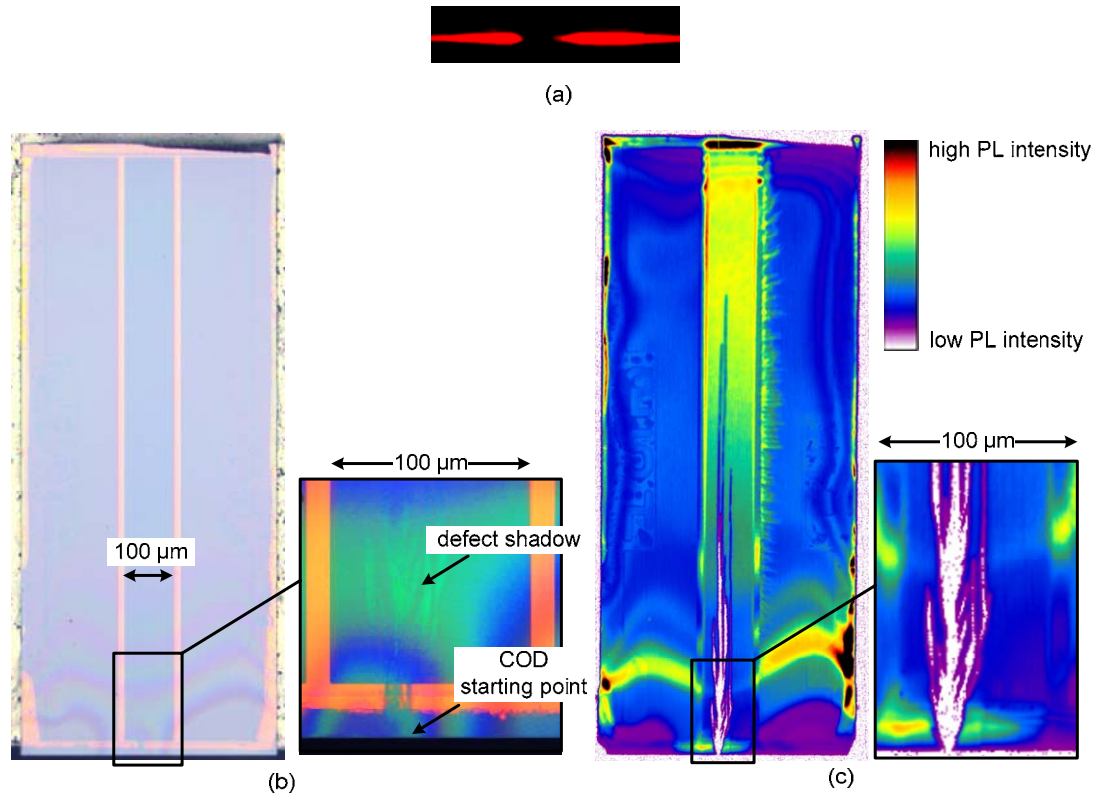
Fig. 4.2.5. AlGaInP BA laser after COD. (a) EL from the output facet. (b) Optical microscope top-view after etching including a magnification of the output facet. Defect shadow can already be spotted. (c) µPL mapping with magnification on the output facet uncovering the COD induced DLDs. (black = high PL intensity, white = low PL intensity)

Figure 4.2.5 shows a laser from the same batch and design as the reference laser displayed in Fig. 4.2.4. This laser was also aged for 1000 h and then driven in COD. Afterwards, it was processed for the µPL mapping experiment according to section 4.2.2. As a protecting resist was used, almost no GaAs cap underetching occurred.

Figure 4.2.5(a) demonstrates the EL form the output facet of the laser. A large dark spot can be identified where the COD occurred. Figure 4.2.5(b) shows the laser after the substrate and resist removal with a magnification of the output facet. Looking at the magnified output facet, first, a defect shadow can be identified. Second, the AR-coating was not affected by COD, since the surface is even and smooth. More FIB images of the AR-coating of this laser will be shown in section 4.2.4.

The µPL mapping of the laser uncovered the defects inside the cavity, as shown in Fig. 4.2.5(c). Obviously, the laser was seriously damaged during COD. Highly non-radiative defects (white = low PL intensity), i.e. DLDs, start from the output facet, split into many branches, and propagate up to a distance of more than half the resonator length. On the other hand, due to the high quality n-GaAs substrate and the state-of-the-art crystal growth, no other DLDs, for example occurring at intrinsic de-

fects as it has been observed by some groups [13][14] in IR-emitters, were detected. The wavy luminescence close to the output facet is due to the inhomogeneous substrate wet-etching, where even small thickness changes can affect the μPL intensity.

4.2.4 FIB microscopy results – AlGaInP BA lasers

In the next experiment, FIB microscopy was employed in order to examine the epitaxial layers affected by COD. The COD driven laser investigated is the same one displayed in Fig. 4.2.5 after it has been processed and mapped by μPL. Figures 4.2.6(a) and 4.2.6(b) show respectively top- and front-view FIB images of the output facet where COD occurred. In Fig. 4.2.6(a), no damage could be identified by FIB on the n-AlGaInP cladding or on the facet. Similarly and as shown in Fig. 4.2.6(b), no damage could be spotted on the AR-coating in the region where COD occurred.
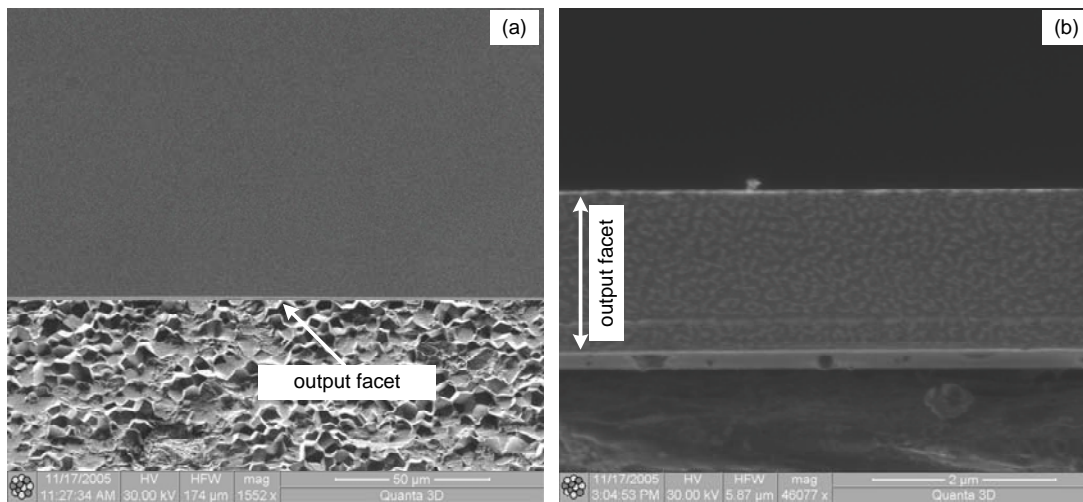
Fig. 4.2.6. (a) Top- and (b) front-view FIB images of the output facet of the processed laser displayed in Fig. 4.2.5.

Knowing from the μPL mapping where the DLDs occurred in the cavity, a FIB cut around 50 μm long, 20 μm wide, and 5 μm deep through the layers (including a defect line) was performed. Such a cut creates a hole in laser where one can look inside on the epitaxy layers. Figure 4.2.7 shows a close-up picture in this FIB cut. The different epitaxial layers and the DLDs can clearly be identified. Interestingly, the defects are confined to the active region, including the QW and partially propagating in the n- and p- AlGaInP waveguide layers.
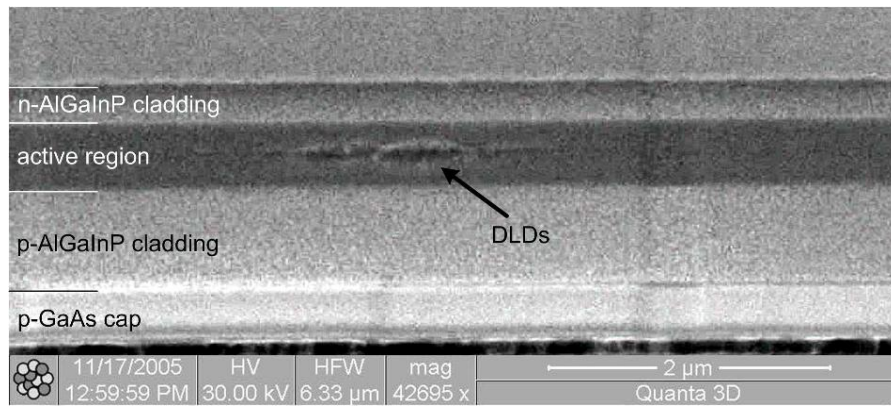
Fig. 4.2.7. FIB cut through of the processed laser shown in Fig. 4.2.5 showing the different epitaxial layers and uncovering a dark line defect.

To understand more about the nature of DLDs, the remaining n-AlGaInP cladding and waveguide layers were further etched (longer in the same etching solution) till reaching the active region. Since the laser analyzed for defects already has a FIB cut through its layers, and the protecting resist was already removed, no further etching was possible. For that reason, other lasers from the same batch were driven into COD and then etched deeply through the active region. Interestingly, the defects became visible. It is important to note that when μPL mapping is performed on a laser before and after deep etching, one gets the same result, i.e. no additional defects occur due to deep-etching.

Figure 4.2.8(a) shows an optical microscope image of a deep-etched laser, where the DLDs became visible. Checking these lasers in FIB also revealed some interesting images of the DLDs. Figures 4.2.8(b) and 4.2.8(c) display two FIB top-views with different magnifications of a deep-etched laser showing the defects leftovers. Height measurements revealed that the defects are elevated with respect to the surrounding undisturbed material, i.e. they etched at a slower rate their surrounding. In analogy to IR-emitters [11], this can indicate that the crystalline nature of the DLDs changed to noncrystalline. However, it will be shown section 5.1.4 using micro-Raman spectroscopy, that probably the nature of the DLDs did not become noncrystalline. This can be due to the fact that the COD level in AlGaInP lasers is relatively low compared to the 980 nm Al-free InGaAs/InGaP lasers investigated in [11], and also to the difference in the material systems themselves (especially in Al content).

Moreover, it can be observed in Fig. 4.2.8(b) and Fig. 4.2.8(c) that the DLDs are composed of semicircular complex dislocation networks, similar to the findings in IR-emitters [14][43]. Due to the large temperatures that accompany the COD effect (see chapter 5), it looks like the semiconductor material was molten and resolidified, probably causing extensive layer intermixing as in [14]. Moreover, the defects spread

into many small branches (in no specific crystal direction) which stop or recombine with the main defect root.
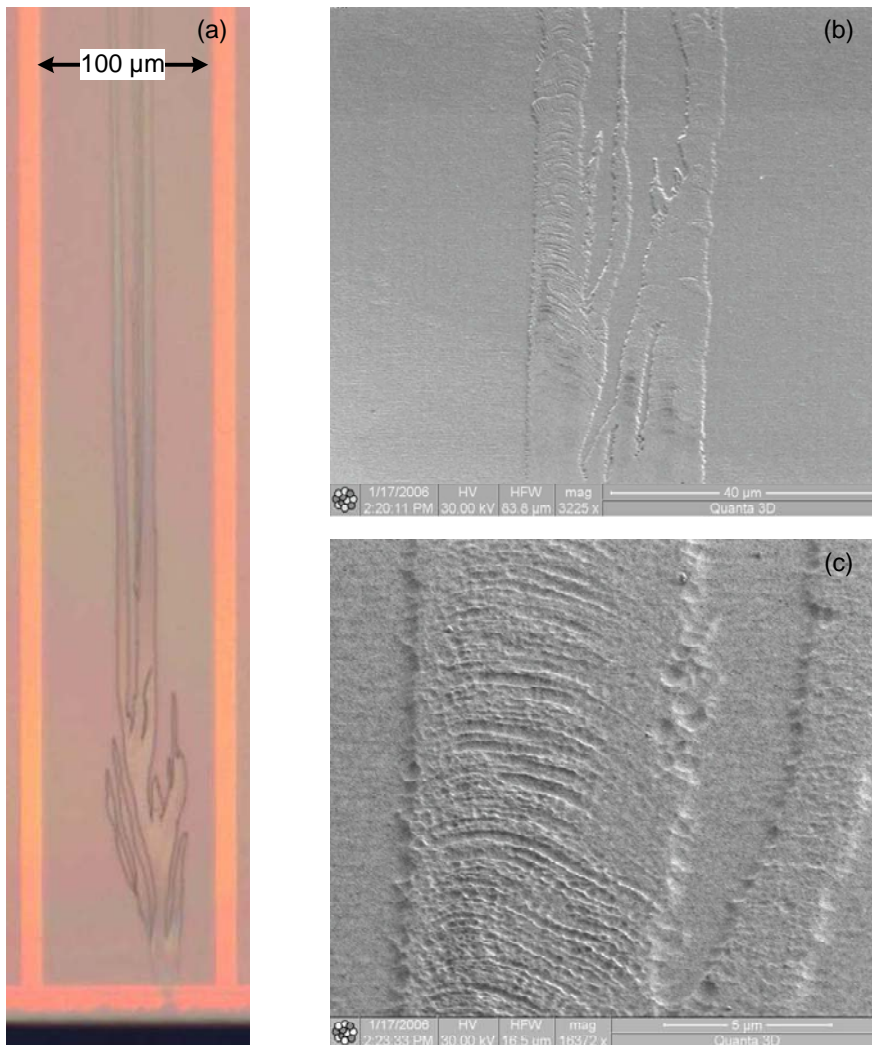
Fig. 4.2.8. (a) Optical microscope image of a COD damaged laser after deep-etching. (b),(c) FIB top-views with different magnifications of a deep-etched laser showing the DLDs leftovers.

The defects have a width of several tens of micrometers at the facet where they start and end up with a tip of a few nanometers. In Fig. 4.2.8(c), it appears from the semi-circles that the DLDs grew in steps. This can be explained as follows: before COD, the optical power density in the cavity is very high and with it the light absorption and temperature near the output facet region. COD is triggered at the point on the facet where temperature is highest (see chapter 5), causing massive damage near the output facet were COD starts. This causes a chain reaction and a gradual defects growth. With increasing defects density in the cavity, the optical power density decreases and with it light absorption and temperature. Finally the optical power density becomes too low to cause further damage; hence no further defects can grow

anymore. This explains why the extent of the DLDs becomes smaller and smaller and at some point, the defects stop propagating into the resonator.

This gradual defect growth is best observed when the lasers are driven in COD in pulse mode. Figure 4.2.9 shows a FIB top-view image of a visible defect in a deep-etched laser that was driven into COD under pulse operation (pulse width: 1 µs, pulse frequency 10 kHz). Here, the COD process repeats at every current pulse and the defects grow step wise in the cavity. It has been reported in IR-emitters that the periodicity of the defective "packets" is related to the magnitude of the drive current pulse at the time of failure [12]. It can be true that the defect periodicity is related to the pulse magnitude, since melting and cooling of the semiconductor is then related to the pulse width and frequency. However, the problem in quantifying such a behavior is that the extent of melting and cooling is also related to the changing optical power density in the cavity during the COD process. Measurements of the defect "packets" of the laser in Fig. 4.2.9 demonstrated that this periodicity changes along the DLDs length. Other interesting studies [44][45] performed on the pulse COD effect revealed that P_{COD} decreases with increasing pulse width. This is reasonable since with increasing pulse width, the average time at which the laser is on is higher and with it the average temperature in the cavity.
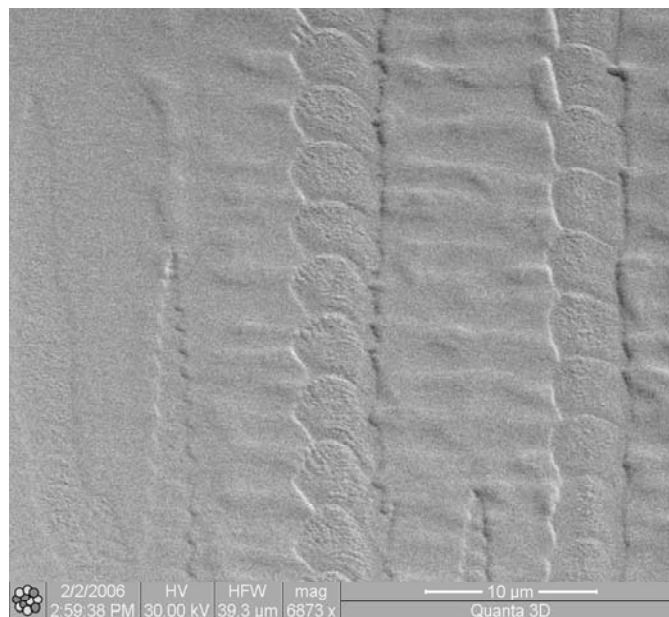
Fig. 4.2.9. FIB top-view of defect leftovers of a deep-etched AlGaInP BA laser that was driven into COD under pulse operation (pulse width: 1 µs, pulse frequency 10 kHz).

4.2.5 Defects induced by spontaneous breakdown

As explained in section 3.3.5, spontaneous breakdown is characterized by a sudden drop in P_{OUT} anytime during lifetime testing. In principle, spontaneous breakdown is a COD event that happens at a much lower output values. This can also be observed

when investigating the defects triggered by spontaneous breakdown. Figure 4.2.10 shows the EL and µPL mapping images near the output facet of a 650 nm AlGaInP BA laser that underwent a spontaneous breakdown event. Similar to COD, spontaneous breakdown caused DLDs inside the cavity, however much smaller as when caused by an intentional COD event. This is expected, since the optical power during a spontaneous breakdown event is much lower than during a typical COD event.
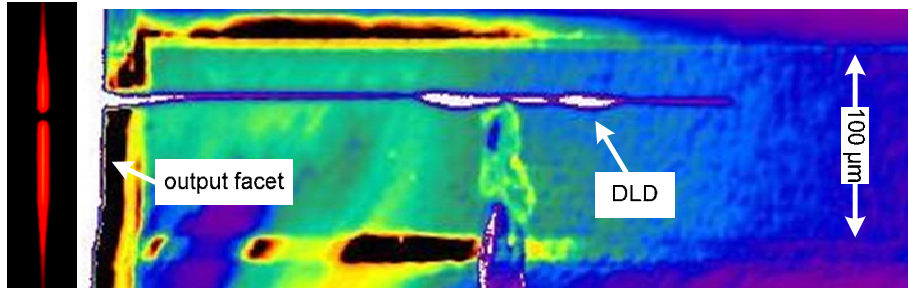
Fig. 4.2.10. EL and corresponding µPL mapping images near the output facet of a 650 nm AlGaInP BA laser that underwent a spontaneous breakdown event.

4.2.6 Results from other laser designs

In this section, COD induced defects in special laser designs, namely in high-power laser bars, and in tapered lasers are examined.

COD in high-power laser bars

In a high-power laser bar, COD can happen in one or more emitters. Usually, the COD starts in one emitter, and then the others follow (especially if they have a common contact configuration). Figure 4.2.11 displays the EL of a 635 nm 5-emitter high-power laser bar mounted on a Sirilas® carrier where the two side lasers underwent a spontaneous breakdown event. 72 h burn-in at 40°C was done on this laser bar before the spontaneous breakdown happened.

Fig. 4.2.11. EL of a 635 nm 5-emitter high-power laser bar where the side lasers underwent a COD event (dark spots are pointed by arrows).

This is an interesting case for discussion, because in the next chapter, it will be shown that COD (or spontaneous breakdown) strongly correlates with the facet temperature. In a mounted laser bar, the center-emitter is in general hottest because of the heat interchange from the neighboring emitters, and also because the heat from the side emitters can better spread to the sides of the heat sink. Figure 4.2.12 displays

simulation results done with COMSOL showing the facet temperature distribution in a 5-emitter laser bar mounted on a heat sink having a 300 K temperature. All emitters are considered to generate the same amount of heat. The simulation clearly shows that the center-emitter is hotter than the edge-emitters.
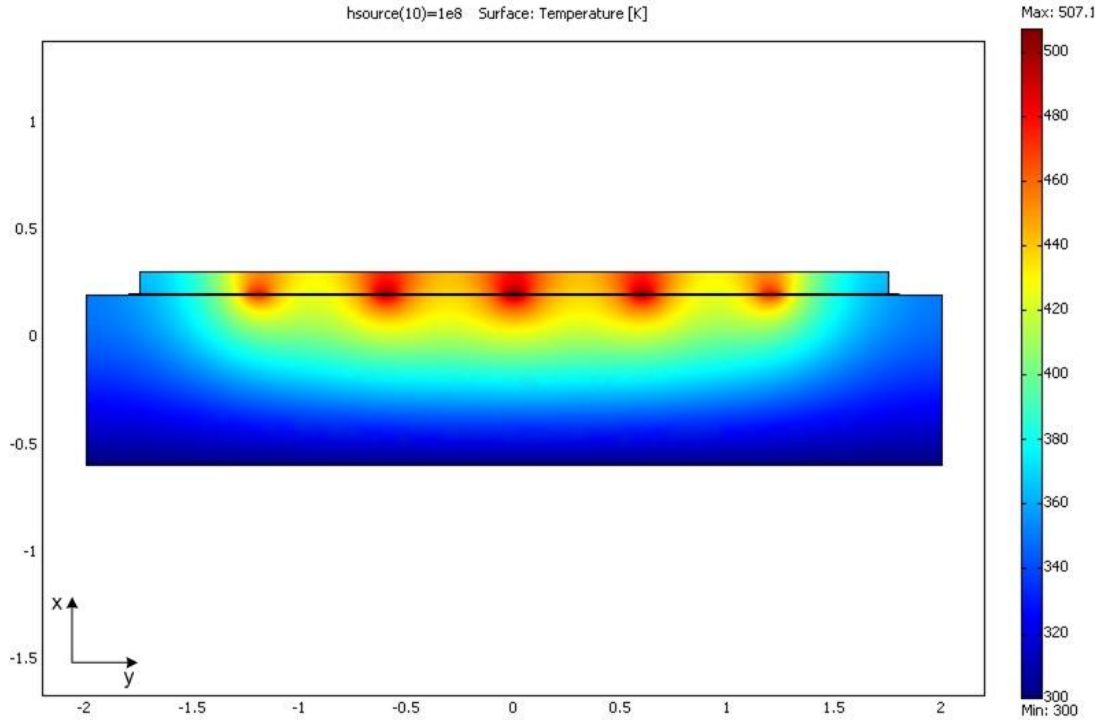
Fig. 4.2.12. Simulation results showing the facet temperature distribution in a 5-emitter laser bar mounted on a heat sink having a 300 K temperature. All emitters are considered to generate the same amount of heat.

According to this fact, it should be expected that the center-emitter goes first into COD. However, and it has also been observed in **[46]**, the facet temperature distribution across the laser bar may change during aging, where the edge-emitters can even become hotter than the center-emitter. This may be due to an increased number defects in the edge emitters, which may have been introduced during packaging (which induce a localized temperature increase). Another reason may be caused by larger emitter currents or even by higher surface currents at the bar edges **[46]**. Moreover, due to the different temperature distribution in a bar, the lasers age differently. This also strongly affects the facet temperature distribution. Due to all those factors, and as it has been observed in other aged and unaged laser bars, it is hard to predict in which emitter the COD is first going to happen. Detailed analysis about the COD temperature dynamics will be discussed in the next chapter.

Figure 4.2.13 shows a COD driven high-power 650 nm 10-emitter laser bar in pulse mode (pulse width: 1 μs, pulse frequency 10 kHz) where only 1 out of 10 lasers underwent a COD event (neither a center- nor an edge-emitter). This was intentionally

achieved by manually shutting down the injection current as soon as P_{OUT} dropped. The laser bar was then processed and deeply etched for defects investigation. As expected, only this one laser had the typical COD induced DLDs. The DLDs also had the typical pulse COD mode periodicity, similar to the single emitter shown in Fig. 4.2.9. The fractures on the mirror of the laser are only due to handling (specifically during the n-metallization polishing), due to the difficulty of processing a mounted long laser bar.

Fig. 4.2.13. 10-Emitter high-power laser bar with pulsed COD (pulse width: 1 µs, pulse frequency 10 kHz). Right: the laser that had a COD and its corresponding EL is shown. Left: the EL of the neighboring laser where no COD occurred.

COD in tapered lasers
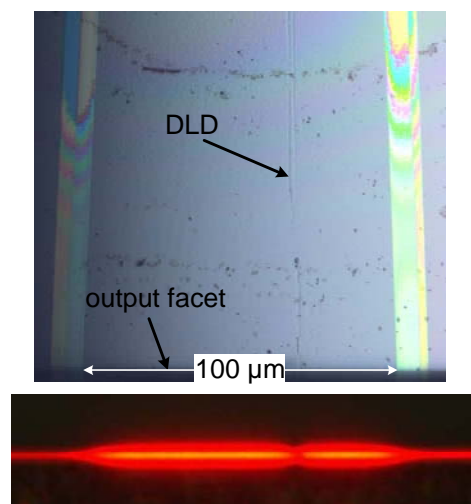
Fig. 4.2.14. EL and corresponding optical microscope images of a deep-etched tapered laser showing that the spontaneous breakdown happened at the front facet.
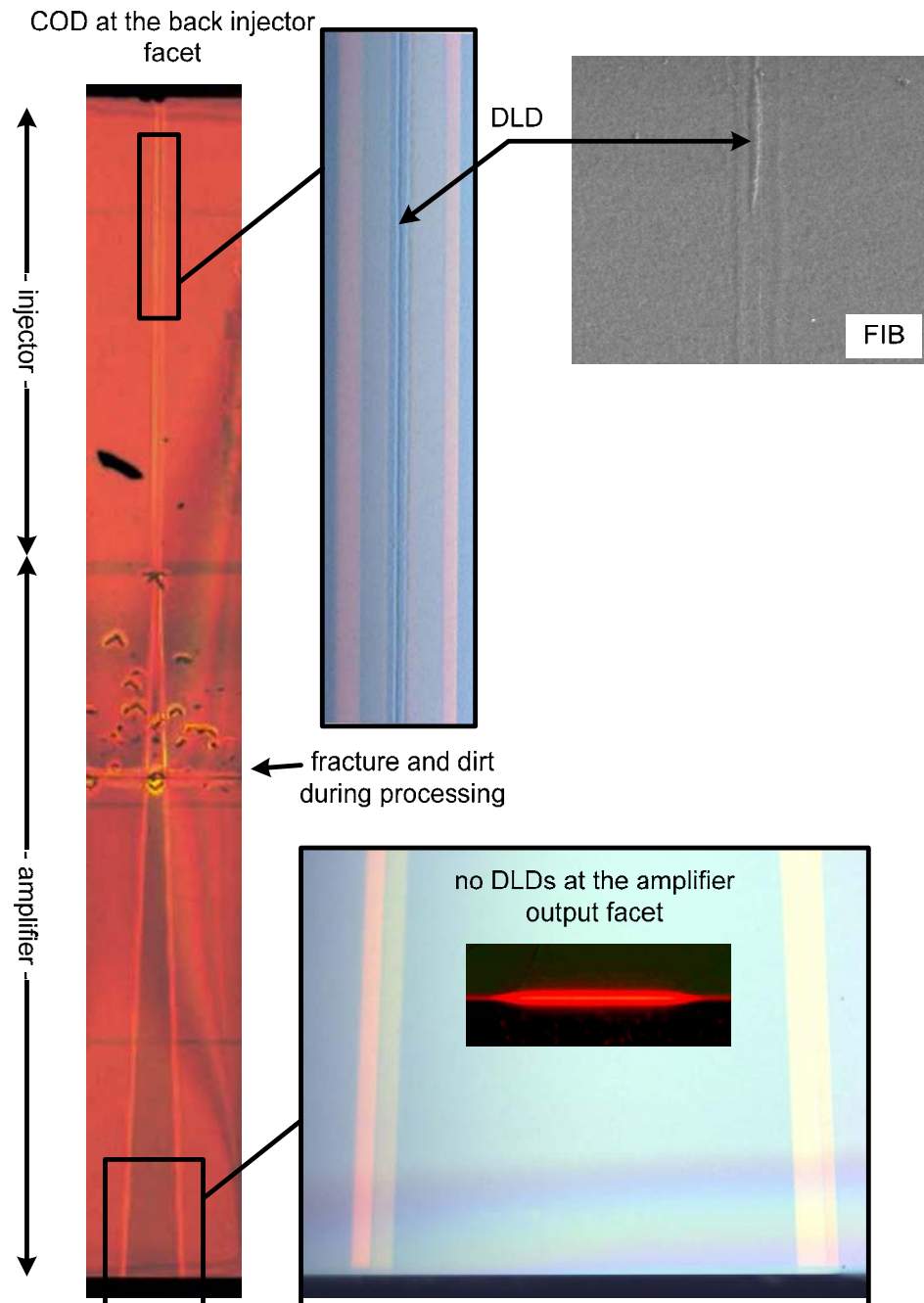
Fig. 4.2.15. EL, optical microscope, and FIB images of a deep-etched tapered laser showing that the spontaneous breakdown happened at the back facet.

As explained in section 2.3.2, a tapered laser is a combination of a ridge laser and a BA laser. The COD in a tapered laser usually happens at the front facet just like BA lasers. However, if external effects come into play, like mechanical defects or facet contamination, it can happen that the COD will happen at the back facet. Figure 4.2.14 shows a deep-etched tapered laser where a spontaneous breakdown happened at the front amplifier side facet. On the other hand, figure 4.2.15 shows a deep-etched tapered laser from the same batch where a spontaneous breakdown happened at the injector side (back facet) and not at the amplifier side (front facet). The lasers were

aged under exactly the same conditions. Understanding what happened to those la-
sers can best be done when looking at the aging results of those lasers shown in Fig.
4.2.16. The lasers degraded very strongly in the first few hours, and had a very
strange aging behavior afterwards, which indicates that external effects caused the
spontaneous breakdown (see section 3.3.5). External effects in this case were strong
facets contamination due to increased dirt accumulation there. Nevertheless, this ex-
ample led to the rare case where COD (or spontaneous breakdown) happens at the
back facet.
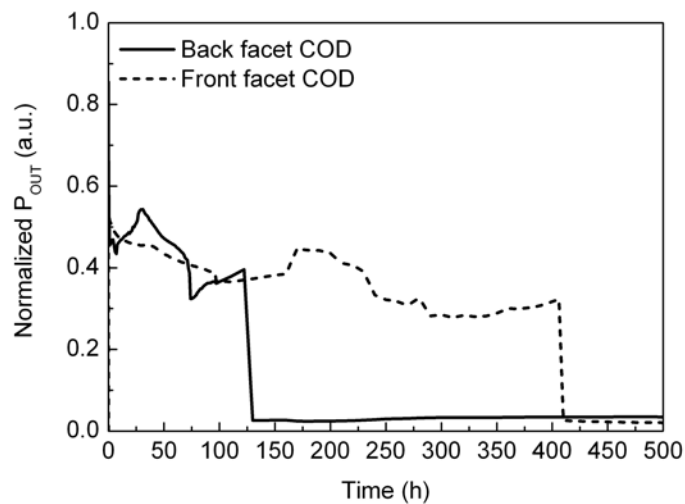
Fig. 4.2.16. Aging test results of the tapered lasers that underwent a spontaneous breakdown. The
dashed line represents the laser where the spontaneous breakdown happened at the front facet (figure
4.2.14). The straight line represents the laser where the spontaneous breakdown happened at the back
facet (figure 4.2.15).

4.2.7 Crystal direction of defects

It has been mentioned by some authors **[13][14]** that the DLDs (in IR-emitters) fol-
low a certain set of crystal directions (e.g. <110>). However, when looking how the
defects wildly split and recombine during COD, it is hard to believe that they really
follow any crystal direction. In order to analyze this phenomena, a special tapered
laser design, where the amplifier opens in a right instead of an equilateral triangle
(i.e. one side continues straight from the injector and one side bends) was analyzed
for COD. Figure 4.2.17 shows this laser after it has been processed and deeply etched
to make the DLDs visible. In this figure, it can be seen that the DLDs follow exactly
the light field direction forced by the bent angle and not the crystal direction perpen-
dicular to the output facet.
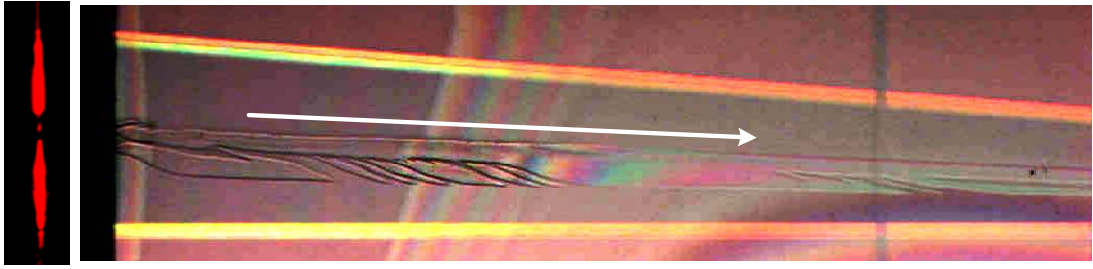
Fig. 4.2.17. EL and corresponding optical microscope images of a deep-etched specially designed tapered laser showing that the DLDs follow the light direction and not a certain crystal direction.

Chapter 5

COD temperature-power dynamics

Facet temperature changes in high-power AlGaInP BA lasers were analyzed by means of micro-Raman (μR) spectroscopy. Measurements as a function of injection current demonstrated that the temperature at the laser output facet rises linearly with optical output power. Temperature profile measurements across the laser stripe showed a strong correlation between near-field intensity, facet temperature, and COD. Additionally, the dynamics of the COD process under continuous wave operation was analyzed by combined thermal and optical near-field imaging. The COD process was revealed as extremely fast, spatially confined, and connected to a pronounced impulsive temperature change. Finally, the P_{COD} temperature-power dependence revealed that a critical facet temperature is needed to induce COD. The consistent results produced by complementary measurement techniques indicate that absorption of stimulated photons at the laser facet is the major source of facet heating and the trigger of COD.

5.1 Facet temperature analysis by micro-Raman spectroscopy

Raman spectroscopy is a very useful nondestructive technique to characterize semiconductor devices. Since it probes lattice vibrations (phonons), which are sensitive to internal and external perturbations, it can be used to study several material features such as composition, crystallinity, crystal orientation, etc. [47], and especially interesting for this study the determination of the local temperature in a lattice.

In order to understand the COD temperature dependence, it is very important to analyze the temperature changes in AlGaInP lasers, particularly at the laser output facet where COD starts. Temperature measurements on ridge laser facets [48][49] and

temperature mapping of broad-area laser facets has been done in the past **[50]**, however only during regular laser operation or after gradual degradation. The situation where lasers operate at their limit finally leading to COD was not investigated in detail. In this section, facet temperature changes of AlGaInP lasers during operation even beyond the COD event were analyzed by µR spectroscopy.

5.1.1 Raman spectroscopy principle

Raman spectroscopy relies on inelastic scattering, or Raman scattering of monochromatic light. In µR spectroscopy, a sample is excited with a laser beam having a spatial resolution in the µm range. During excitation, the excitation laser photons interact with the lattice vibrations (phonons). If the collision is elastic, the energy of the scattered light does not change after the collision (also called Rayleigh scattering). However, a small fraction of emitted light (approximately 1 in 10^7 photons) is scattered at energies different from the energy of the incident laser light. The process leading to this inelastic scatter is called the "Raman Effect" and its energy shift is called "Raman shift" **[51]**. There are two inelastic scattering possibilities:

1. <u>Phonon emission:</u> If part of the incident photon energy is transferred to the lattice, the energy of the scattered photon is decreased by the same amount; the respective spectral lines are called Stokes-lines.

2. <u>Phonon absorption:</u> If the incident photon absorbs a phonon, the energy of the scattered photon is increased by the same amount; the respective spectral lines are called anti-Stokes-lines. This effect can occur when there is a substantial density of phonons present. The anti-Stokes-lines are usually weaker compared to the Stokes-lines.

For a Raman scattering process, not only conservation of energy, but also conservation of momentum is required in crystalline solids **[47]**:

$$\hbar\omega_{scattered} = \hbar\omega_{incident} \pm \hbar\omega_{phonon} \qquad (5.1)$$

$$k_{scattered} = k_{incident} \pm k_{phonon} \qquad (5.2)$$

Here, ω refers to the angular frequency and k to the wavevector. The sign (+) applies to the anti-Stokes components, whereas the sign (–) refers to the Stokes scattering. Since most semiconductors are opaque for the visible light used for Raman scattering, Raman experiments are mostly performed in the backscattering configuration. The incident light is perpendicular to the surface, and the backscattering light is collected along the same direction. Furthermore, when the backscattering configuration is used to analyze crystalline material, since the incident light and the scattered light

are perpendicular to a certain crystal plane, not all lattice vibration can be observed in a Raman scattering experiment. This is due to the polarization selection rule described in **[52]** and **[53]**. Following Loudon's description of the Raman tensors, it was found for crystals with zinc blend structure that for backscattering from a (100) surfaces, only the longitudinal optical (LO) phonons can be observed. From a (110) surfaces only transversal optical (TO) phonons are allowed and for (111) surfaces both the LO and TO phonons should be detected.

5.1.2 Temperature measurement

Information on temperature by µR spectroscopy can be extracted in three different ways **[47]**: from the Stokes/anti-Stokes intensity ratio, from the frequency, and from the FWHM of the Raman peak. Using the Stokes/anti-Stokes intensity ratio works well in general, as long as the signal to noise ratio remains low. More easily, and as explained in the next section, the Stokes frequency shift can be used to determine the facet temperature of lasers.
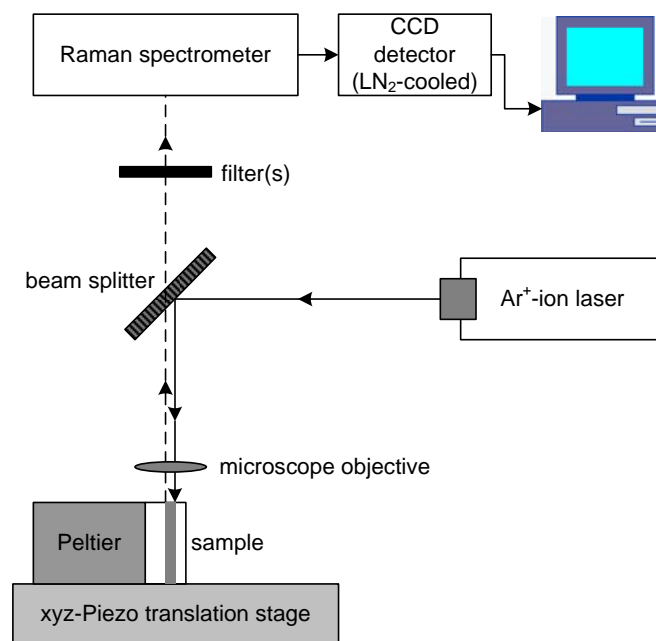
Fig. 5.1.1. A backscattering µR spectroscopy measurement setup.

A backscattering µR spectroscopy measurement setup (Fig. 5.1.1) is used in this study. A DILOR™ *x-y* Raman spectrometer is employed and as an excitation source, a 488 nm Ar$^+$-ion laser is focused to about 1 µm with cw power < 1 mW (leading to a temperature increase of ~ 10 K on the sample's surface). In order to get a good signal due to the presence of dark noise, the CCD camera is LN$_2$-cooled to around –196 °C. To get an acceptable signal to noise ratio, typical measuring times lie between 60 and 180 s. The PL coming out of the laser should be filtered. For historical reasons, the Raman signal is plotted vs. wavenumber, which is defined by $1/\lambda$ in cm^{-1}. In the

plots, only the Raman shift with respect to the excitation laser's wavenumber is presented.

Actually, the Raman Effect can be observed in an excited sample, independent of the excitation laser's wavelength. However, attention should be paid when using an excitation laser having a wavelength shorter than the sample's wavelength, i.e. when PL is generated. As the crystal symmetry is partially broken on the material surface, weak higher order harmonic frequencies can be generated. This becomes problematic if they lie in a range close to the excitation laser's wavelength. For example when exciting a 980 nm sample with a 488 nm laser, the second harmonic lies by 490 nm and can dramatically disturb the Raman signal.

Raman scattering measurements in AlGaInP layers were extensively analyzed by [54]. Figure 5.1.2 shows a typical Stokes signal measured at an AlGaInP BA laser facet at room temperature. Figure 5.1.3 shows the composition dependence of measured phonon frequencies of various modes in $In_{1-x}Al_xP$ and $(Al_xGa_{1-x})_{0.51}In_{0.49}P$ layers by [54].

In this study, the lasers investigated are grown on a (100), 6° towards $(1\bar{1}\bar{1})$ misoriented n-GaAs substrate by metal-organic vapor phase epitaxy. Cleaving is afterwards performed in a way that the laser output facet corresponds to the $(0\bar{1}1)$ plane. So according to the selection rule, measuring the Raman scattering from this surface should only allow the TO phonons to be observed. Since in our case the investigated laser's crystal growth is misoriented, made of several epitaxial layers, and the crystal surface can be rough, the selection rule is usually lifted. In this case and as displayed in Fig. 5.1.2, both transversal optical (TO) and longitudinal optical (LO) phonons were observed in the Raman scattering signal of the AlGaInP lasers. Comparing the measured Raman signal in Fig. 5.1.2 to the ones measured by [54] in Fig. 5.1.3, a very strong correlation can be deduced. As the exciting laser used for measurements has a spatial resolution of about 1 µm, i.e. the spot size is larger than the active region thickness (around 0.5 µm), the measured Raman signal correspond to an average between the Stokes signals from the InGaP QWs (x = 0), the $Al_{0.4}Ga_{0.6}InP$ waveguide (x = 0.4), and $Al_{0.7}Ga_{0.3}InP$ cladding (x = 0.7) layers. This means that a comparison to Fig. 5.1.3 is best done at 0.3 < x < 0.4.

The measured AlGaInP phonon lines shown in Fig. 5.1.2 at around $325\,cm^{-1}$ and 345 cm^{-1} correspond respectively to the InP-like TO and InP-like LO phonon lines deduced by [54]. The lines around $425\,cm^{-1}$ and $458\,cm^{-1}$ correspond respectively to the AlP-like TO and AlP-like LO phonon lines. In this study, the AlP-like LO-phonon peak change with temperature was followed, since it had the strongest line intensity.
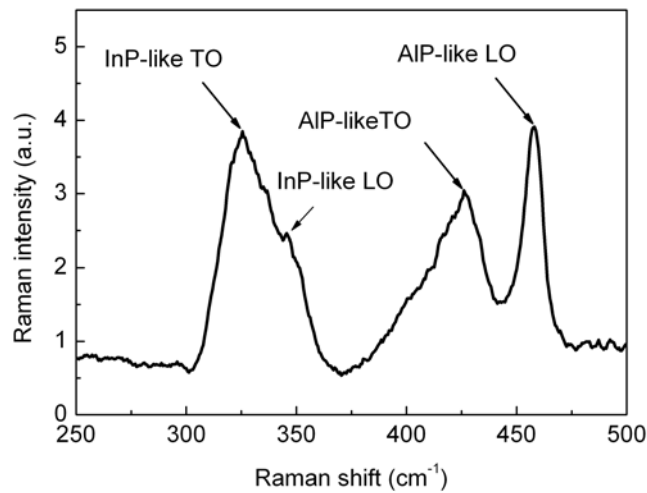
Fig. 5.1.2. Typical Stokes signal measured by a 488 nm Ar$^+$-ion laser from a standard AlGaInP laser at the output facet at room temperature.
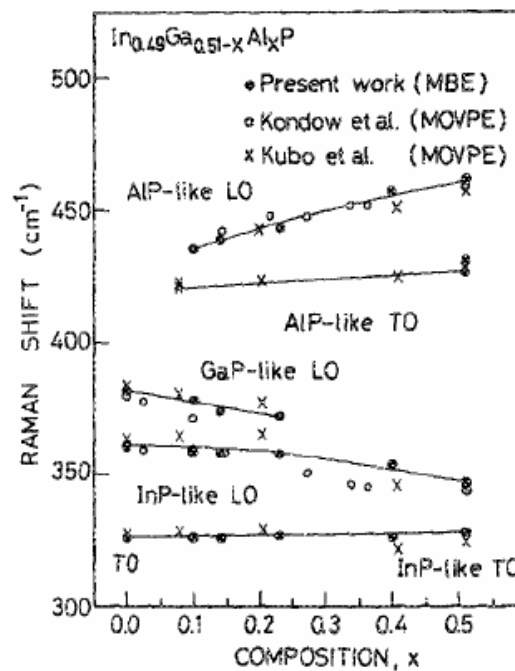
Fig. 5.1.3. Composition dependence of measured phonon wavenumbers of various modes in $(Al_xGa_{1-x})_{0.51}In_{0.49}P$ layers at room temperature. Solid lines represent the best-fit [54].

5.1.3 Temperature determination

In order to determine the laser's facet temperature at a certain cw injection current or with increasing injection current, a temperature calibration measurement was first performed. For that reason, the injection current is set to 0, and the Stokes lines frequency shift with increasing heat-sink temperature is measured. This leads to Stokes lines shift towards smaller wavenumbers (due to lattice expansion). If this phonon

frequency shift is called dω_{ph}, then dω_{ph}/dT is determined. Now with increasing current and at a fixed heat-sink temperature, internal laser heating also leads to Stokes frequency shift, i.e. dω_{ph}/dI can be determined. Now dividing (dω_{ph}/dI)/(dω_{ph}/dT) gives the information dT/dI, i.e. the change of temperature at the excited spot with changing injection current.

Figure 5.1.4 shows the Stokes line shift with temperature of a standard 650 nm AlGaInP BA laser between T_{HS} = 30 and 60 °C at I = 0 A. A value for dω_{ph}/dT ~ 0.028 cm^{-1}/K was obtained.
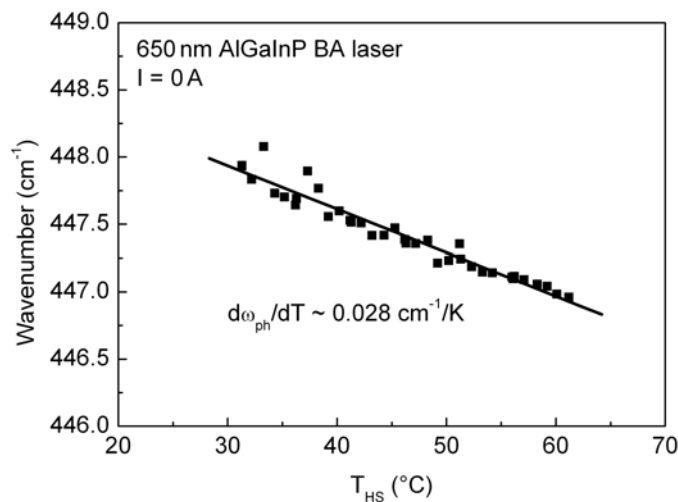
Fig. 5.1.4. AlP-like LO phonon Stokes-line shift with temperature of a standard 650 nm AlGaInP BA laser.

5.1.4 Facet temperature vs. injection current

The facet temperature (T_{FACET}) rise with increasing driving current was analyzed by μR spectroscopy even beyond the COD event. The results were obtained from 7 nominally 'identical' 650 nm standard AlGaInP lasers from the same batch with threshold current densities of ~ 0.3 kA/cm^2 and slope efficiencies between 0.8 and 1 W/A at ambient temperature.

Before performing this measurement, comparison between the Raman signals of a good AlGaInP and COD affected material was made. This comparison is necessary in order to check that the Raman signal does not change at the COD damaged material. Otherwise, wrong interpretation of the results during the COD effect would make it impossible to identify how the temperature changed after COD. On top of that, since Raman spectroscopy is sensitive to internal and external perturbations, it can be used to study several material features, including the crystallinity of materials. This means that information about the crystalline nature of the defects, as mentioned

in section 4.2.4, can also be investigated. For this experiment, an unprocessed laser was used, and several processed lasers as in section 4.2, including a laser etched only till the n-AlGaInP cladding and a deep-etched laser. Raman signal measurements similar to the one displayed in Fig. 5.1.2 were performed on the COD induced DLDs and compared to the undisturbed surrounding material, but no significant difference in the Raman signals could be observed. From this finding, it can be concluded that most probably, the DLDs did not become noncrystalline, unlike as what has been observed in the 980 nm Al-free InGaAs/InGaP lasers investigated in [11]. Fortunately, this also indicates that µR spectroscopy can be used to study the temperature changes after COD, as the Raman signal is not affected by material morphology changes at the COD defect sites.

Figure 5.1.5(a) shows facet and bulk temperatures versus injected current density at 25 °C for two devices. In laser 1, the measured spot was distant from the COD starting point at the facet (which is characterized by a dark spot in the electroluminescence (EL) picture taken afterward), whereas in laser 2, the measured spot was in close vicinity to the COD starting point. The arrows pointing at the EL pattern denote the position on the facet where the actual T_{FACET} measurement was performed. The bulk temperature (T_{BULK}) of the lasers, represented by triangles in Fig. 5.1.5(a), is obtained as

$$T_{BULK} = (VI - P_{OUT})R_{th} + T_{HS} \qquad (5.3)$$

where V is the laser voltage, I is the injection current, R_{th} is the measured thermal resistance as in section 2.4.5.

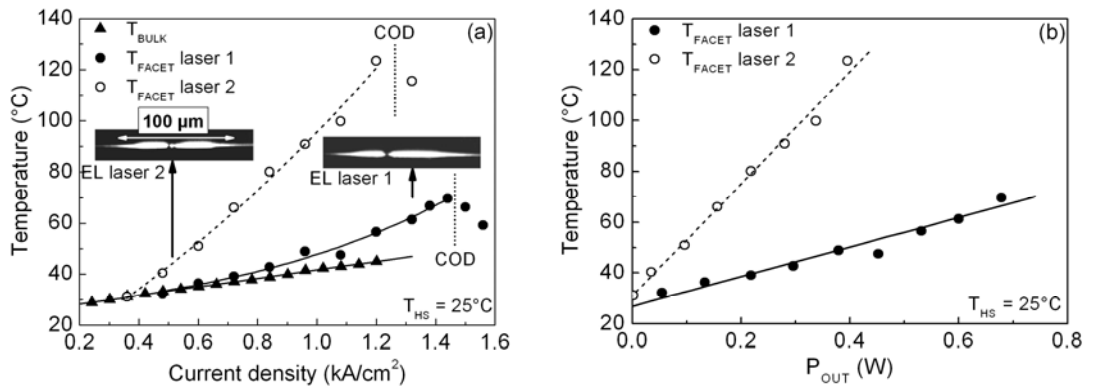
Fig. 5.1.5. (a) T_{FACET} measured by µR spectroscopy vs. injection current density of two 650 nm standard AlGaInP BA lasers (laser 1 = filled circles, laser 2 = open circles). T_{BULK} vs. injection current density for the lasers (triangles). Electroluminescence (EL) patterns of laser 1 and laser 2 after COD are also shown. (b) T_{FACET} vs. P_{OUT} for the same lasers before COD.

Below laser threshold, the laser heating is mainly due to Joule heating, which leads to only a small temperature increase ($\sim 5\,\mathrm{K}$) at the facet. Comparing the temperature curves for the two lasers above threshold, it can be seen that T_{FACET} rises with laser driving current, however this increase is much more dominant in the vicinity of the COD starting point at the facet (laser 2). After COD, T_{FACET} decreases for both lasers. In order to make sure that the Raman signal itself did not change at the defects after COD, Raman signal measurements at the facet at $I = 0\,\mathrm{A}$ were done after COD at the COD starting point and at an intact point next to it were no COD occurred.

Figure 5.1.5(b) shows T_{FACET} of the same lasers versus P_{OUT} before COD. The linear increase of T_{FACET} with P_{OUT} indicates that the facet temperature increase is mainly due to absorption of laser light at the output facet. After COD, the sudden drop in P_{OUT} results in lower light absorption at the facet, leading to a T_{FACET} decrease.

5.1.5 Facet temperature vs. near-field intensity

In order to understand the results of the previous experiment, a temperature line scan measurement across the 100 μm wide active stripe of a BA laser from the same batch as the lasers in the previous section was performed. The cw injection current density was set to $0.67\,\mathrm{kA/cm^2}$ and the heat-sink temperature T_{HS} to 20 °C. Figure 5.1.6(a) shows the near-field intensity (NFI) before and after COD, and the corresponding T_{FACET} measurement. Before COD, a strong correlation between NFI and T_{FACET} was found (see solid line and full circles). Hot regions on the laser facet are clearly correlated with high NFIs. This correlation is shown in Fig. 5.1.6(b).
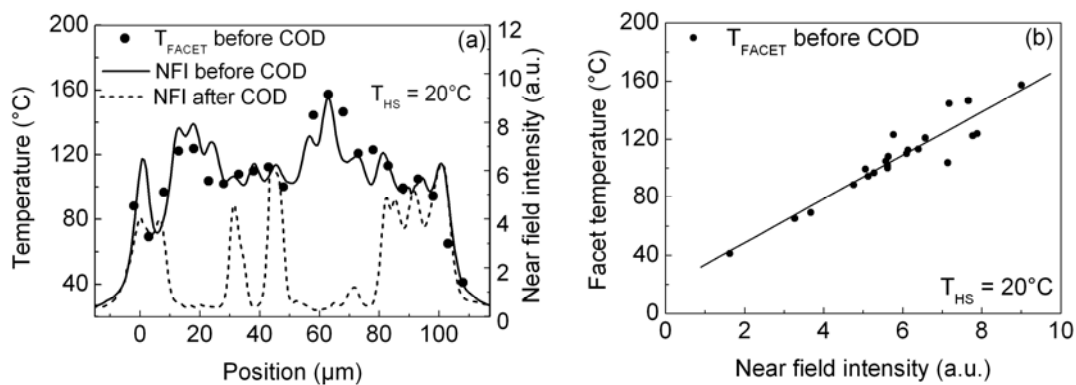
Fig. 5.1.6. (a) NFI of a laser at $0.67\,\mathrm{kA/cm^2}$ and $T_{HS} = 20$ °C before (solid line) and after (dashed line) COD. T_{FACET} profile across the active stripe of a laser before COD (full circles). (b) T_{FACET} vs. NFI before COD for the same laser.

As evident by the NFI, COD happened at the hottest facet temperature spots, i.e., at the highest NFI peaks (for first COD event, followed by COD at the next peaks). After analyzing several fresh and aged devices, it was found that especially in nonde-

graded lasers, COD happens at the highest NFI peaks, which indicates again that the temperature increase at the facet is mainly due to light absorption. In strongly degraded laser devices, however, additional surface defects can arise with oxide growth on the facets **[39][40]** causing localized nonradiative surface recombination hence localized hot regions at the facet. This finally provokes a "thermal runaway" and eventually COD not necessarily at the NFI peaks.

The peaks appearing in the NFI are due to filamentation, which is a common problem in BA high-power lasers. Filamentation in BA devices can be due to two mechanisms: (i) changes in the carrier density which affect both the optical gain and the refractive index seen by the intracavity field **[55]-[58]**; (ii) fluctuations in the cavity due to externally induced inhomogeneities or voids, such as thermal inhomogeneities at nonradiative defects **[59]**.

To quantify the change of refractive index and gain with carrier density on the dynamical properties of semiconductor lasers, Henry introduced the linewidth enhancement factor as **[56][57]**

$$\alpha_H = -\frac{4\pi}{\lambda}\frac{\partial n/\partial n_c}{\partial g/\partial n_c} = -\frac{4\pi}{\lambda}\frac{\partial n}{\partial g} \tag{5.4}$$

where n is the refractive index, g is the gain per unit length, λ is the wavelength and n_c is the carrier density. For example, calculations have shown that filamention in BA lasers with active stripe width > 50 µm occurs if α_H exceeds 0.5. Since α_H typically exceeds 2 for such devices, filamentation is unavoidable **[58]**.
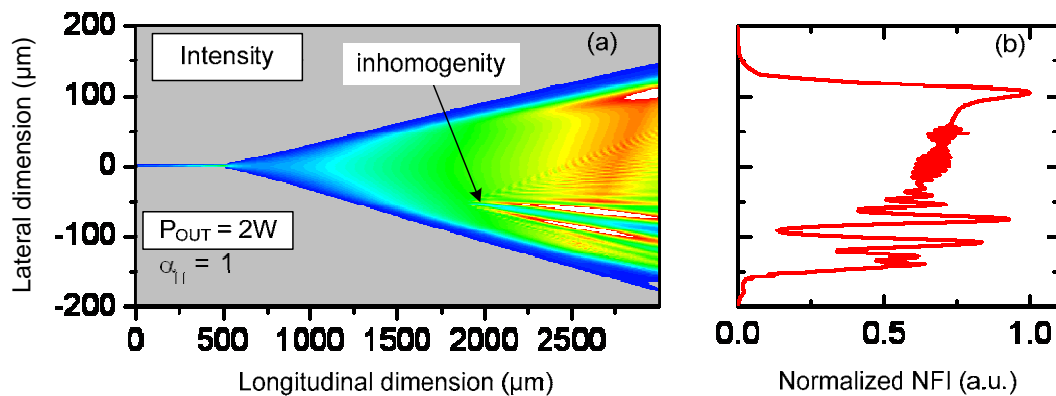
Fig. 5.1.7. Simulation on an IR tapered laser showing the effect of thermal induced inhomogeneities on filamentation. (a) Top-view intensity distribution in the cavity. (b) Corresponding normalized NFI [59].

Externally induced inhomogeneities in the cavity are usually due to inhomogeneous soldering or at some hot spots occurring at nonradiative defects. In Fig. 5.1.7, a simulation performed at the Fraunhofer Institute IAF **[59]** based on the equations in **[57]**

on an IR tapered laser shows the effect of induced thermal inhomogeneities on fila-
mentation and the corresponding NFI (this will eventually cause a change in the re-
fractive index).

It can be seen in Fig. 5.1.7 how the light intensity field splits at the induced inho-
mogeneity causing several filamentation peaks in the NFI. In order to reduce the ef-
fect of this mechanism, homogeneous soldering and mounting of the laser, as well as
good heat-sinking can help.

5.2 COD dynamics by real-time imaging

Since μR spectroscopy is a versatile but rather slow method, the complete tempera-
ture dynamics during the fast occurring COD event is not fully resolved. For the
measurements in section 5.1.4, the operation current density is increased in small
discrete steps ($\sim 0.04\,kA/cm^2$), and after each increase, the Raman signal is meas-
ured. Thus, as shown in Fig. 5.1.5(a), the COD occurs between two measurement
steps. Alternatively, thermoreflectance could be used for quicker measurements [60].
However, T_{FACET} measurements during COD obtained with that method can be
masked by simultaneous changes in surface (reflectivity) and material morphology.
In this section, spatially and temporally analyses of the COD process by combined
thermal and optical NFI imaging with cameras, which is a relatively fast method,
complement the μR facet temperature measurements.
For this experiment, 650 nm standard AlGaInP lasers were used. Stable cw operation
with threshold currents densities of $\sim 0.3\,kA/cm^2$ and slope efficiencies of $\sim 1\,W/A$
are observed. Three devices that exhibited almost identical COD scenarios with COD
current levels of $2.0\,A < I < 2.2\,A$ were used for the investigation. In the following,
one of such data sets is discussed.

Two cameras are employed in parallel. A Si-CCD camera covering the spectral range
from 300 to 1100 nm images the optical NF of the laser diode. At the same time, a
focal-plane-array HgCdTe thermal infrared (TI) camera working in the $3.4 - 5.5\,\mu m$
range images the temperature distribution of the entire facet of the laser including the
submount. The nominal spatial resolutions are $0.77\,\mu m/pixel$ and $8.8\,\mu m/pixel$ for NF
and TI imaging, respectively. The integration times were 500 ms (NF) and 2 ms (TI).
The emission from the laser diode is split by a dichroic mirror tilted towards the TI
camera that is situated directly in front of the laser's front facet and under an angle of
63° towards the NF camera. The mirror is based on Si with an AR-coating for $\lambda > 3$
μm and a HR-coating for $\lambda < 1$ μm. The laser current is ramped from 0 to 2.1 A in
discrete steps of 20 mA at a frequency of 0.5 Hz until COD and beyond at $T_{HS} = 20$
°C. The synchronized NF camera delivers one image per current step. The TI cam-

era, on the other hand, is continuously recording at 430 Hz (i.e., 2.3 ms per frame, with a dead time of only 0.3 ms).
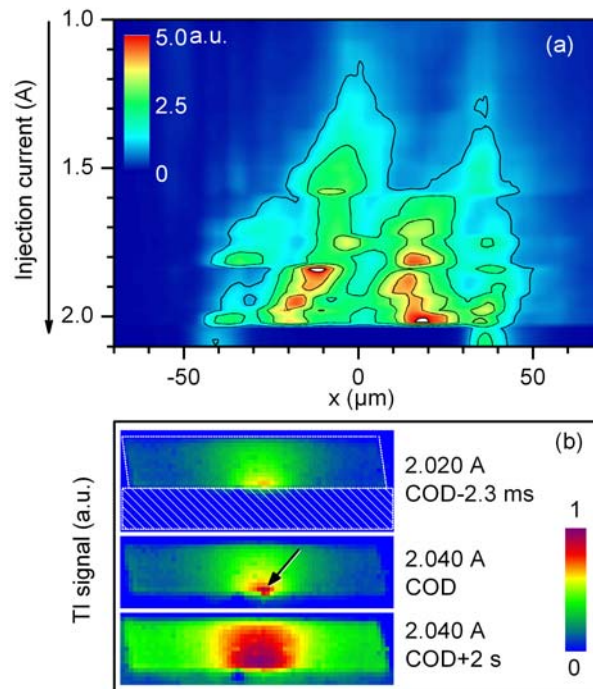
Fig. 5.2.1. (a) Optical NFI taken from the CCD camera vs. injection current. The COD occurred between 2.02 and 2.04 A. Equipotential lines at intensities of 1, 2, 3, 4, and 5 are given. (b) Raw TI images of the front facet before, at, and 2 s after COD. COD occurred at the location indicated by an arrow (top to bottom). The dimensions of the diode (500 µm width) are indicated by the dotted white line and the submount is shaded.

Figure 5.2.1 displays data measured with the two camera systems. In Fig. 5.2.1(a), the evolution of the NF with injection current is given and the typical filamentation in BA lasers is visible. There are two main maxima at -30 µm $< x < -10$ µm and at 10 µm $< x < 30$ µm (x represents the lateral position across the facet), the latter one leading at an intensity of 5.2 a.u. to the COD event between 2.02 and 2.04 A. The peak at the position x ~ -11 µm reaches a distinct maximum (5.4 a.u.) at 1.84 A, without, however, accompanying COD. Figure 5.2.1(b) shows three selected TI images. The arrow points to the location of the COD event (COD seed) and the white rhomboid marks the shape of the laser diode.
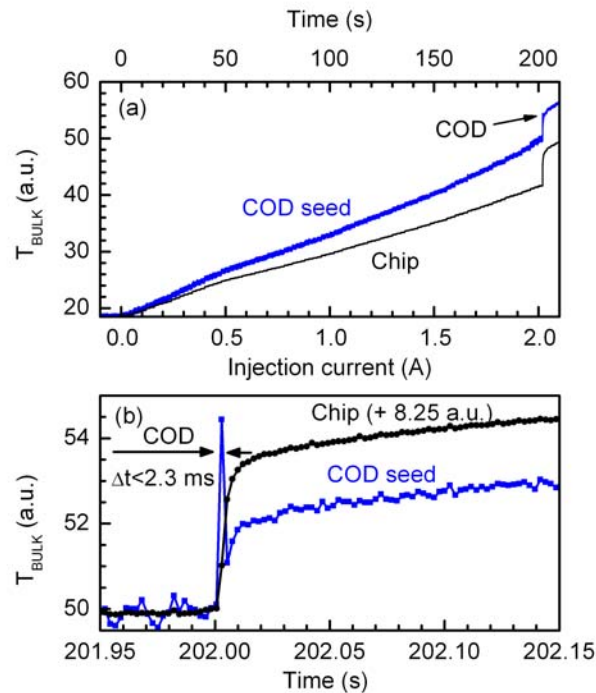
Fig. 5.2.2. (a) Bulk temperature increases with injection current of a single pixel (COD seed, blue line) and the entire semiconductor chip. (b) Data from (a) around the COD event on an expanded scale showing the T_{BULK} vs. time. The entire chip temperature is shifted 8.25 a.u. up for comparison.

Figure 5.2.2 illustrates the thermal behavior of the device as extracted from sequences of TI images such as those in Fig. 5.2.1(b). In Fig. 5.2.2(a), the temperature increase of the region where COD occurred ("COD seed") and of the entire semiconductor chip (averaged) are plotted as a function of injection current. Figure 5.2.2(b) displays the time evolution of the temperature increase at the COD seed and for the entire chip.

Figures 5.2.3 show selected lateral temperature profiles derived from thermal images recorded at different times. The corresponding raw camera image of the device front (500 μm wide) from Fig. 5.2.1(b) at the time of COD is displayed in Fig. 5.2.3 (a). Both panels (b) and (c) refer to the same local scale and pairs of lines with the same color are taken at the same current (and time).

Fig. 5.2.3. (a) Raw camera image of the device front (500 μm wide) from Fig. 5.2.1 at the time of COD. (b) Absolute temperature profiles taken from Fig. 5.2.1(b) along a line that contains the active region. The temperature flash at COD (green line) and the subsequent average temperature jump (red line) are displayed.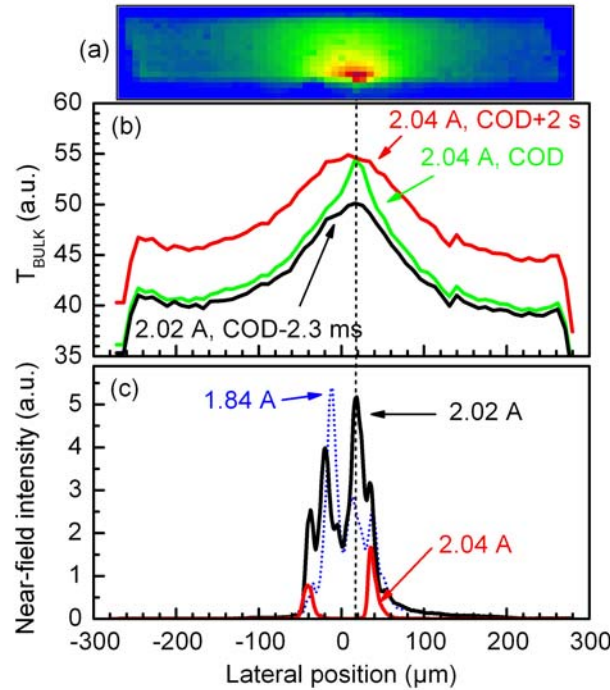 (c) Corresponding NFI profiles before and after COD [black and red lines as in (a)]. The dotted blue line represents the highest NF intensity observed at I = 1.84 A.

The laser's thermal evolution en route to COD is here discussed. Starting at zero current, the bulk temperature of the laser chip rises linearly up to the laser threshold (I_{th} ~ 0.4 A, Fig. 5.2.2(a)). Above threshold, the slope of the temperature rise is reduced due to stimulated emission. As observed by the μR measurements, the laser facets are hotter than the bulk, mainly because of additional absorption and surface recombination processes (see section 5.1). The reabsorption of the laser emission at the front facet is proportional to the NFI distribution displayed in Fig. 5.2.1(a). As a consequence, both the bulk and the facet temperature peak at the most intense filaments in the active region.

Since TI averages along almost the entire cavity, the contribution of the facet is usually very weak, but at high currents close to COD (> 1.7 A) the temperature near the active region rises in a super-linear way (blue curve in Fig. 5.2.2(a)). At a current of I ~ 2.04 A, the facet cannot withstand this load and the laser sustains COD. This gives rise to (i) an exceptional short temperature spike at the location of the damage (blue lines in Fig. 5.2.2)), (ii) an almost complete collapse of the NFI (Fig. 5.2.1(a)), and (iii) a rapid increase of the average bulk temperature of the whole chip (Fig. 5.2.1(b) and Fig. 5.2.2(b)). The data of Fig. 5.2.1 and Fig. 5.2.2 suggest that the COD process is initiated in a spatially highly confined part of the laser chip. The COD process

manifests itself as a single pixel and single frame event from which an upper limit of $\Delta x \times \Delta y \leq 8.8 \times 8.8 \ \mu m^2$ and $\Delta t < 2.3$ ms for the spatio-temporal dimensions of the COD seed is derived. The measured temperature overshoot at COD represents the average over such dimensions, i.e., a lower limit, with potentially much higher values for a fraction of the volume or time interval.

The combined TI and NFI data (Fig. 5.2.3) demonstrate that the thermally observed COD seed occurs at the same point in space as the strongest peak of the NFI distribution. This finding is compatible to what has been observed in the µR spectroscopy experiment. A high optical facet load is, however, only a necessary condition for COD, because the intensity of the NF filament observed for I = 1.84 A was already higher than the one at I = 2.02 A, which is the COD injection current (Figs. 5.2.3(c) and 5.2.1). Consequently, a sufficient condition could be a high optical load at the facet plus a high thermal load in the bulk, resulting in a critical facet temperature as the key precondition for the occurrence of COD. The interplay between temperature and power and the critical temperature approach are further analyzed in the next section.

5.3 COD temperature-power analysis

For further analysis of the relation between temperature and COD, identical unaged 650 nm standard AlGaInP lasers (batch 1) where driven into COD at T_{HS} between 10 and 40 °C. Figure 5.3.1 shows the power-current curves of these lasers and their corresponding T_{BULK}.

With increasing T_{HS}, the laser gain decreases and the carrier leakage increases, leading to an increase in I_{th} and a decrease in η_{slope}, respectively. For each laser, T_{BULK} was calculated and its value at COD was registered. First, it can be seen that T_{BULK} increases quickly at COD, due to an abrupt drop in P_{OUT}. After COD, it keeps rising with increasing current due to increased carrier recombination. Note that even though the T_{FACET} decreases after COD due to the reduced light absorption, if the injection current is further increased, T_{FACET} will increase again along with T_{BULK}. The behavior of P_{OUT}, T_{BULK}, and T_{FACET} before and after COD is schematically illustrated in Fig. 5.3.2.
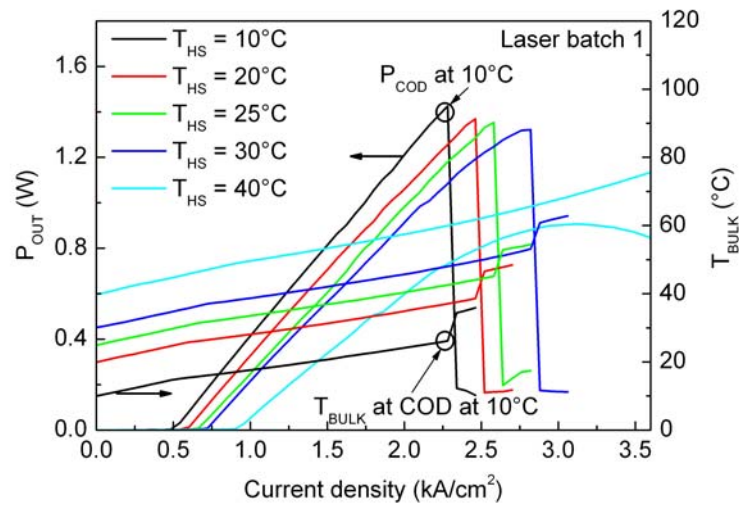
Fig. 5.3.1. Power-current curves and corresponding T_{BULK} curves of five broad-area AlGaInP lasers at T_{HS} between 10 and 40°C (batch 1). P_{COD} and T_{BULK} at COD at 10°C are indicated by open circles.
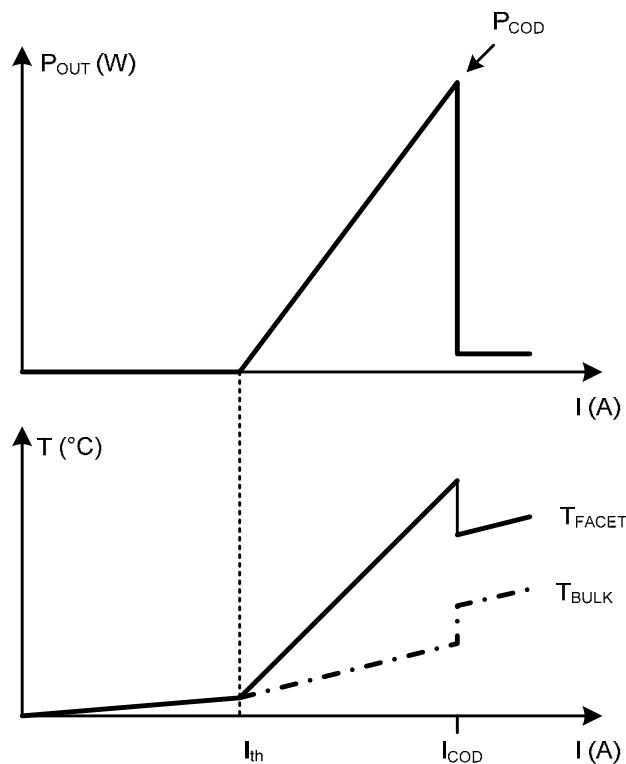
Fig. 5.3.2. Schematic behavior of P_{OUT}, T_{BULK}, and T_{FACET} before and after COD. Here worst case is shown where only spontaneous emission is left after COD.

On the other hand, P_{COD} decreases with increasing T_{HS} (at T_{HS} = 40°C, the laser undergoes thermal rollover and no COD occurs). In Fig. 5.3.3, P_{COD} at the different T_{HS} is plotted versus the corresponding T_{BULK} at COD for the lasers shown in Fig. 5.3.1

(triangles, batch 1). Interestingly, in the measured range of T_{HS}, P_{COD} and the corresponding T_{BULK} at COD have a linear relationship with increasing T_{HS}.
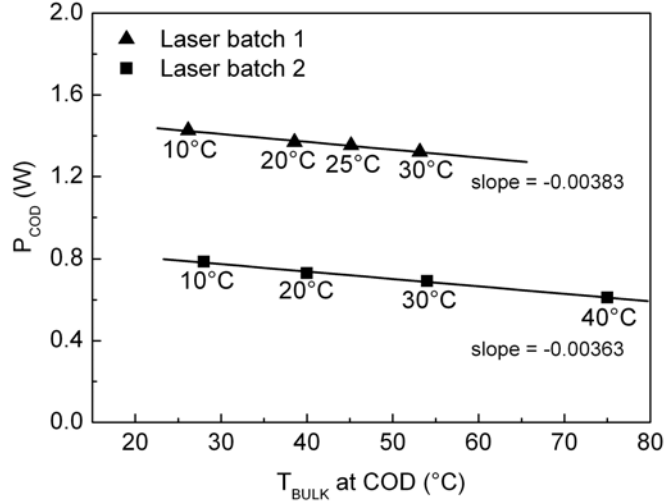
Fig. 5.3.3. P_{COD} vs. T_{BULK} at COD for the lasers shown in Fig. 5.3.1 (triangles, batch 1) and P_{COD} vs. T_{BULK} at COD for lasers belonging to another epitaxy design (squares, batch 2).

Analyzing several additional lasers from other batches with emission wavelengths between 635 and 650 nm, it was found that this linearity (with almost the same slope ~ – 0.003) always occurs. As an example, figure 5.3.3 shows similar data of another set of 635 nm lasers with a different epitaxy design (squares, batch 2), leading to lower P_{COD} values. Both set of data show similar temperature-power dependence. This dependence can be explained with a critical facet temperature (T_{FCRIT}) necessary to induce COD. This critical facet temperature is determined by the bulk temperature, T_{BULK}, and the local near field intensity, NFI, as

$$T_{FCRIT} = T_{BULK} + const \times NFI \tag{5.5}$$

This approach explains why the COD occurs at the NFI peaks, and supports the idea that *the major facet heating is caused by light absorption* at this position. Moreover, this indicates why in section 5.2, the COD did not occur at 1.84 A at the highest near-field intensity peak, because T_{BULK} was not high enough for the facet temperature to reach critical facet temperature required for COD to take place. Thus the results of sections 5.1, 5.2 and 5.3 are collectively clarified.

5.4 Comparison: IR-emitter

A tapered 940 nm AlGaAs/InGaAs single QW laser was driven into COD for defects analysis and comparison to AlGaInP based devices. Figure 5.4.1 displays the output facet and the corresponding EL images after COD. Interestingly, and as it has been observed by some authors [41], the COD leaves visible defects on the Al_2O_3 AR-coating. This can be due to the fact that in IR emitters, P_{COD} is much larger than in red emitters.
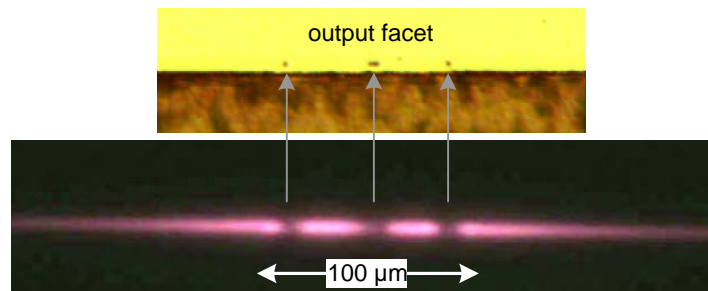
Fig. 5.4.1. Output facet and corresponding EL images of a tapered 940 nm AlGaAs/InGaAs single QW laser after COD. Arrows point to the visible defects in the AR-coating due to COD.

To check the defects inside the cavity, µPL mapping and FIB analyses were performed on this laser. Figure 5.4.2 shows a µPL mapping image (with a magnification of a defect) of the tapered laser amplifier where the DLDs occurred, and a FIB image of a defect after deep etching.
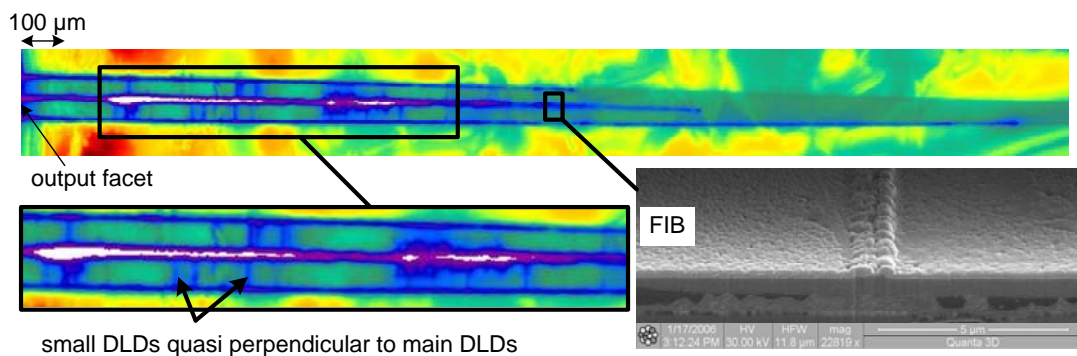
Fig. 5.4.2. µPL mapping image (with a magnification of a defect) of the COD tapered laser amplifier shown in Fig. 5.4.1 where the DLDs occurred and a FIB image of the defects after deep etching.

It is remarkable to note that the two side DLDs also follow the light field direction similar to what has been observed in AlGaInP emitters in section 4.2.7. Second, some other small DLDs spreading quasi perpendicular to the main DLDs are present. This has not been observed in AlGaInP lasers. One major difference between the two

lasers is that IR-emitters do not have a misoriented GaAs substrate during growth as in red-emitters. However, it is unclear if this caused those extra dislocations.

After the μPL experiment, the laser was deeply etched through the active region and observed by FIB as shown in Fig. 5.4.2. The defects are basically similar to the ones in AlGaInP lasers, as they are confined to the active region and etch slower than the intact surrounding material. It is interesting to also note that under a white light optical microscope illumination, the defects do not become visible when stopping the etching at the n-AlGaAs cladding, since AlGaAs material is not transparent under white light illumination like AlGaInP material. An IR-microscope should be used in this case to see the defects shadow.
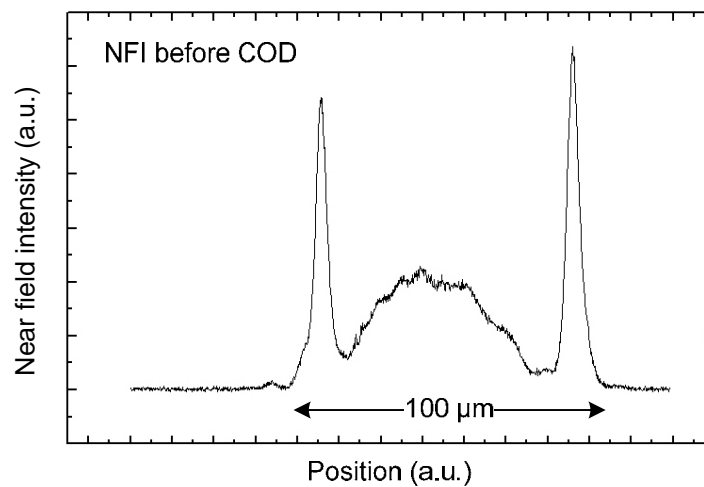
Fig. 5.4.3. NFI of the tapered 940 nm AlGaAs/InGaAs before COD

After demonstrating the correlation between COD and the NFI peaks in red lasers, a comparison to IR lasers would support the analysis. Figure 5.4.3 shows the NFI of the same tapered 940 nm AlGaAs/InGaAs emitter before COD. The NFI of this laser has two strong peaks at the sides and one smaller peak in the middle. This laser was one in a series of test lasers where different design parameters were being changed, which led to the unusual 3 peaks in the NFI (as the diffraction of the ridge waveguide does not match the angle of the taper). On the other side, it came out to be very suitable for this investigation. Just like in AlGaInP lasers, strong correlation between the NFI and the COD is identified. This reveals that also in IR-emitters, light absorption at the output facet plays an important role in understanding the COD effect.

Chapter 6

Influence of design parameters on COD

The increasing importance of extracting high optical power out of semiconductor lasers motivated several studies in COD level improvement. For the past two decades, such improvements have especially been done on infrared (IR) emitters, but recent improvements on AlGaInP material were also successful. Recent developments include quantum well intermixing (QWI) near the facets to decrease absorption there **[7][8][61][62]**, proper facet passivation to reduce surface oxidation **[6][63]-[68]**, and current-blocking to reduce surface recombination at the mirrors **[9][10]**. Some other sophisticated growth techniques with multiple epitaxial runs introduce an epitaxially grown window layer to decrease absorption near the facets regions **[69]-[71]**. In this chapter, the COD dependence on epitaxy and process design parameters is presented. Moreover, COD level improvement in AlGaInP by low-absorption facet designs is demonstrated.

6.1 Influence of chip design on COD

6.1.1 Influence of waveguide thickness and wavelength

Changing the epitaxial parameters has a great influence on COD. Figure 6.1.1 shows pulse P_{COD} data vs. wavelength of lasers belonging to different epitaxy designs. Highlighted are lasers with two different AlGaInP waveguide thicknesses, namely a group with waveguides thickness = 50 nm (i.e. p-waveguide = n-waveguide = 50 nm; filled squares), and another group with waveguides thickness 250 nm (empty dia-

monds). The fluctuations in P_{COD} within one waveguide thickness group are due to the fact that other parameters have also been changed.
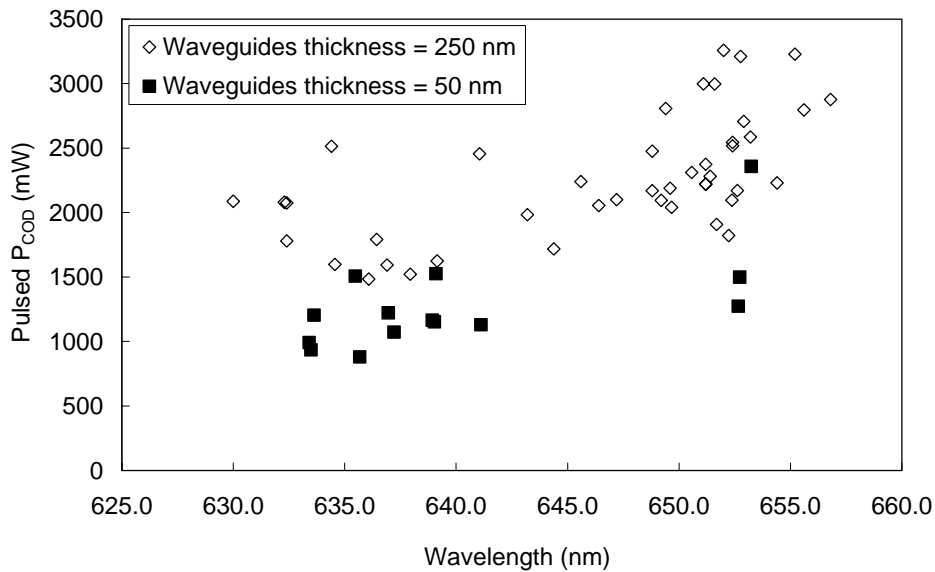

Fig 6.1.1. Pulsed P_{COD} vs. wavelength for different epitaxy designs. Waveguides thickness = 50 nm (filled squares) and waveguides thickness = 250 nm (empty diamonds) are highlighted.

Looking at Fig. 6.1.1, it can be seen that the lasers with a thinner waveguide tend to have a lower P_{COD}. In order to understand this phenomenon, a simulation of the intensity profile of the guided fundamental mode inside the cavity of single QW (SQW) 650 nm AlGaInP lasers with waveguide thicknesses of 40 and 200 nm was performed. The calculation was carried out according to the transfer matrix theory for layered media described in [72]. The optical confinement factor Γ for both cases was extracted. Figure 6.1.2 shows the intensity profiles of the fundamental mode inside the cavity of standard AlGaInP laser structure as in Fig. 2.2.2. The layer parameters used in the simulation are displayed in the figure's inset.

For the 200 nm thick waveguide, the calculation resulted in a confinement factor $\Gamma_{200\,nm} = 0.0169$, and for the 40 nm thick waveguide $\Gamma_{40\,nm} = 0.0196$. The COD level worsening in the thinner waveguide can be explained as follows: the thinner the waveguide, the higher the confinement factor Γ. This leads to an increase in the output power in the cavity for the same injection current. As explained in section 5.1, the facet temperature is proportional to the output power, i.e. the critical facet temperature ($T_{FCRIT} \propto P_{OUT}$) and COD are reached faster for thinner waveguides[*].

So improved COD level performance can in general be achieved by increasing the waveguide thickness. However, a trade-off should to be made when having a lower confinement factor. A lower Γ leads to a higher threshold gain, as g_{th} is proportional

---

[*] For very thin waveguide thicknesses, a critical limit is reached where the fundamental mode cannot be confined to the waveguide anymore, but expands in the cladding, leading anew to a decrease in the confinement factor.

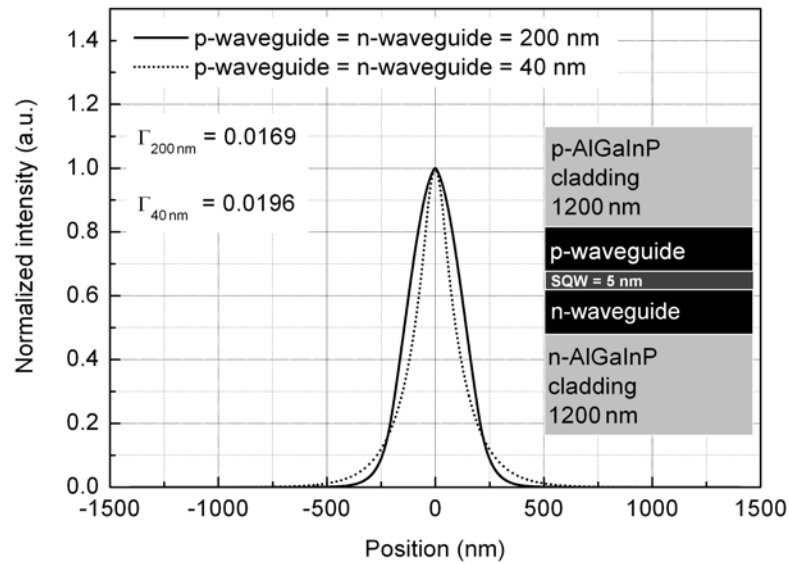to $1/\Gamma$ as in equation (2.11), and results in a threshold current increase according to equation (2.15).

Fig 6.1.2. Intensity profiles of the fundamental mode inside the cavity of standard AlGaInP laser structure calculated for two different waveguide thicknesses. Inset: layer structure parameters used in the simulation.

Another observation which can be extracted from Fig. 6.1.1 is that AlGaInP lasers with shorter wavelengths have a lower P_{COD} then the ones with longer wavelengths. This is due to the fact that lasers with shorter wavelengths have shallower QWs compared to longer wavelengths lasers, which increases the carrier leakage, i.e. decreases the injection current efficiency. This increases the dissipated power P_{diss}, which leads to a higher loss in form of heat, i.e. increased temperature in the device and according to section 5.3, an increase in T_{FACET}, and eventually lower COD level.

6.1.2 Influence of resonator length

In order to study the influence of the resonator length L on COD, several 638 nm Al-GaInP 60 µm BA lasers from the same epitaxy design and wafer were used. Resonator lengths of 900, 1200, 1500, and 1800 µm were compared. In order to analyze only the effect of the resonator length on P_{COD}, the lasers were uncoated and unmounted, and pulsed P_{COD} was determined. In this case, COD happens randomly at the front or back facet of the lasers. Figure 6.1.3(a) shows pulsed PI-curves of several lasers with different resonator lengths measured above threshold. Figure 6.1.3(b) shows the mean P_{COD} for each length variation vs. resonator length for the same lasers.

Figure 6.1.3(b) demonstrates that P_{COD} increases linearly with increasing L. Actually, the easiest way to get more power out of a resonator is to increase its area, however with increasing L, as shown in Fig. 6.1.3(a), $I_{th} = b \times L \times j_{th}$ also increases (or j_{th} decreases) and η_{slope} decreases for longer resonators, which is theoretically expected according to equations (2.15) and (2.18).
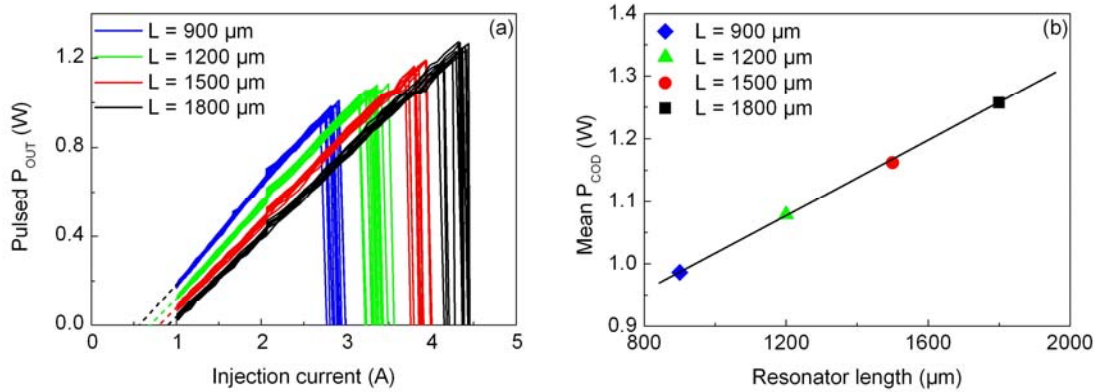
Fig 6.1.3. (a) Pulse PI-curves vs. injection current of unmounted and uncoated AlGaInP 60 µm BA lasers with different resonator lengths above threshold. (b) Mean P_{COD} vs. resonator length for the same lasers.
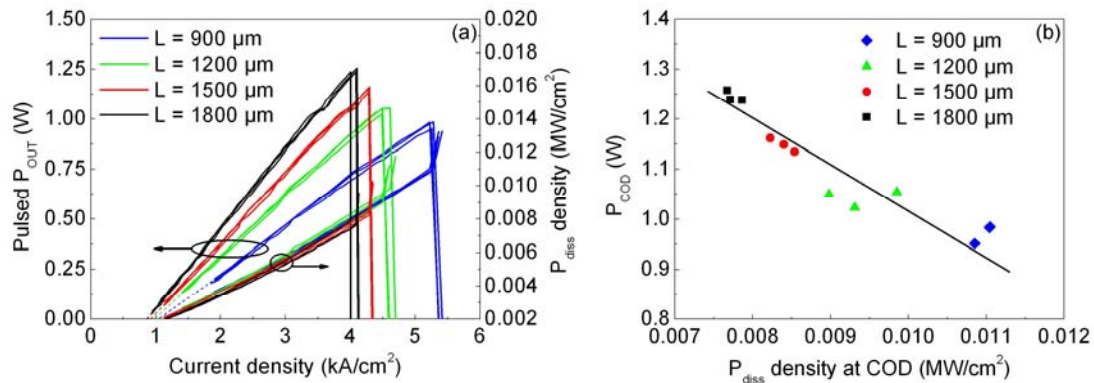
Fig 6.1.4 (a) Pulsed P_{COD} vs. current density of for the same lasers of Fig. 6.1.2. (b) P_{COD} vs. the corresponding P_{diss} density at COD for the same lasers. For picture clarity, only 3 lasers from each length variation are plotted.

It is not trivial to perceive why P_{COD} is higher for longer resonators when looking at the PI-curves, because many parameters, such as I_{th}, η_{slope}, etc…change with resonator length. This is why the data should be evaluated vs. the densities. Figure 6.1.4(a) shows the same curves as in Fig. 6.1.3(a) (data of only 3 lasers are shown for picture clarity), though vs. the current density. Also, the dissipated power <u>density</u> (P_{diss} density = $P_{diss}/L \times b$) in MW/cm^2 is also plotted vs. the current density (remember: $P_{diss} = VI - P_{OUT}$). Figure 6.1.4(b) displays the absolute values of P_{COD} vs. P_{diss} density at COD for the same lasers. Here, the comparison is very similar to what has

been done in section 5.3, however in this case, one cannot speak of $T_{BULK} = P_{diss} R_{th} + T_{HS}$ because the lasers are unmounted and the measurements are done in pulsed mode. For that reason, at room temperature and without heat sinking, P_{diss} can be used to evaluate how much power is lost in form of heat, which will eventually influence T_{FACET}.

Looking at Fig. 6.1.4(a), it can be seen that j_{th} decreases for longer resonators, which is expected according to equation (2.15). Moreover, it can be seen that P_{OUT} is higher for longer resonators when plotted vs. the current density. Now looking at Fig. 6.1.4(b), interestingly, in the measured range of L, P_{COD} and the corresponding P_{diss} density at COD have almost a linear relationship with increasing L, which is to be expected according to the logic used in section 5.3. Since for increasing L P_{OUT} is higher (vs. the current density), less P_{diss} density (or bulk temperature) is needed for T_{FACET} to reach T_{FCRIT}. This is due to the fact that the critical facet temperature depends on both the bulk temperature and the output power, leading to a higher COD levels for longer resonators.

From this analysis, it can be concluded that higher output powers and eventually higher P_{COD} can be achieved using longer resonators; nevertheless, this is useful only when working at high output powers, since I_{th} and η_{slope} become worse when L increases. Moreover, difficulties in mounting long resonators can cause inhomogeneity problems.

6.2 Influence of facet passivation on COD

Facet passivation is the processing of the laser facets to reduce degradation. Having a facet free of defects is essential for obtaining a good laser performance, as additional local absorption at facet surface defects can negatively influence the aging and the COD level. As explained in section 2.3.4, the facets of the lasers are often coated with dielectric materials which not only provide a barrier for atmospheric oxygen, moisture, etc., but also alter the facet reflectivities, maximizing the front-to-back P_{OUT} ratio and increasing the overall device efficiency. However, great care is required when coating the air-cleaved facets, because oxygen and moisture can eventually deposit on the mirrors prior to coating, which leads to increased degradation and hence COD at lower P_{OUT} than would ordinarily be expected. In order to prevent surface oxidation prior to coating deposition, the first solution would be ultrahigh-vacuum cleaving and subsequent in-situ passivation [73]. Nevertheless, such a sophisticated process is not suitable for mass production as it is very expensive and time consuming. Other solutions, such as proper facet passivation procedure and

finding the right coating material and deposition parameters can greatly be advantageous.

Over the past years, several studies have been performed to develop the right facet passivation procedure. Pre-coating facet treatments include ablation by unreactive ions (e.g. argon) [63]-[65], sulphation [63][66][67], elemental (e.g. silicon, aluminum) barrier layer [63], hydrogenation and passivation by a thin semiconductor layer (such as ZnSe, BeTe, Si,…) in the epitaxy reactor [68], nitridation (bombardment by ionized nitrogen) [65], or silicon nitride (Si_3N_4) layers [63].

Such pre-coating facet treatments can serve the following [63]:

1. The removal of surface states resulting from dangling bond imperfections, thereby removing any surface conductive layers, decreasing the facet temperature during operation and improving the device efficiency.
2. The removal of any surface oxide already present.
3. The occupation of states prone to oxidation, thus reducing oxidation.
4. The stabilization of the crystal structure at the output facet to decrease scatter, improving efficiency.
5. Creating a diffusion barrier, preventing oxygen incorporation from the atmosphere, oxygen diffusion toward the surface of the crystal from the facet coating, and preventing the diffusion of atoms in the crystal outward into the facet coating.
6. Minimizing absorption: any coating must exhibit a low absorption coefficient at the lasing wavelength, so as not to increase the facet temperature under operation.

Though some passivation pre-coating treatments have proven to be useful, it is essential to test the aging stability of the lasers after facet processing. In many cases, some processes lead to a lower COD level on unaged devices, however, prove to have much better aging stability after burn-in and aging. For example, figure 6.2.1 demonstrates the P_{COD} aging behavior of standard 650 nm AlGaInP BA lasers with and without facet pre-coating treatment to remove the unwanted mirror oxidation before coating deposition. All lasers where air-cleaved and coated with Al_2O_3.

Interestingly, the lasers with facet pre-coating treatment have lower P_{COD} than the ones without any facet pre-coating treatment. However, after burn-in and aging, the pretreated lasers show a more stable aging behavior and higher P_{COD} values than the untreated ones. This can be due to the fact that facet pre-coating treatments, for example with unreactive ion ablation or hydrogenation can introduce additional defects on the facets leading to a worst COD threshold before aging. On the other hand, the lasers without facet pre-coating treatment are more vulnerable to aging, because

more defects can develop due to the formation of surface oxides during laser operation, and lead to local facet heating and ultimately a faster COD event compared to the ones with a pretreatment.
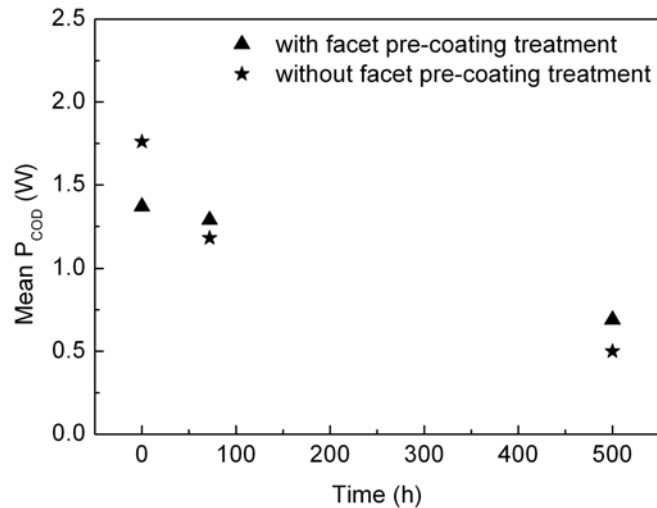
Fig 6.2.1. Mean P_{COD} vs. aging time of coated standard 650 nm AlGaInP BA lasers with and without facet pre-coating treatment.

On the other hand, some expensive and sophisticated facet passivation processes can improve the COD level. For example, figure 6.2.2 shows COD aging data of standard 635 nm AlGaInP BA lasers with two different facet passivation processes. Process 1 requires about twice the processing time and cost compared to process 2. Before aging, process 1 showed about 55 % improvement in the P_{COD} level compared to process 2, but less than 20 % improvement after 1000 h aging; this does not make it so attractive considering the minor improvement it brought.
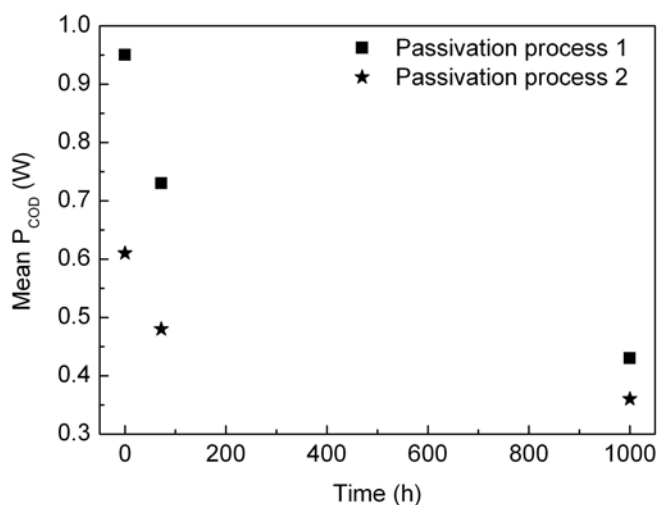

Fig 6.2.2. Mean P_{COD} vs. aging time of coated standard 635 nm AlGaInP BA lasers with two different facet passivation processes.

6.3 Influence of low-absorption facets on COD

Photon absorption and nonradiative carrier recombination at surface states, lead to increased facet temperature and lower P_{COD}. Reducing the carrier injection near the facets regions has demonstrated to be an efficient way to reduce T_{FACET}, i.e. the non-radiative carrier recombination there, and introducing a window structure to avoid absorption at the mirror facet by QWI, or by re-growing a semiconductor layer having a larger bandgap than the active region proved to be the most ideal methods to suppress COD.

6.3.1 Current-blocking

Introducing a non-injection region near the facets has shown to be an effective way to improve COD [9][10]. This can be done by simply pushing the p-metallization back from the facet regions.
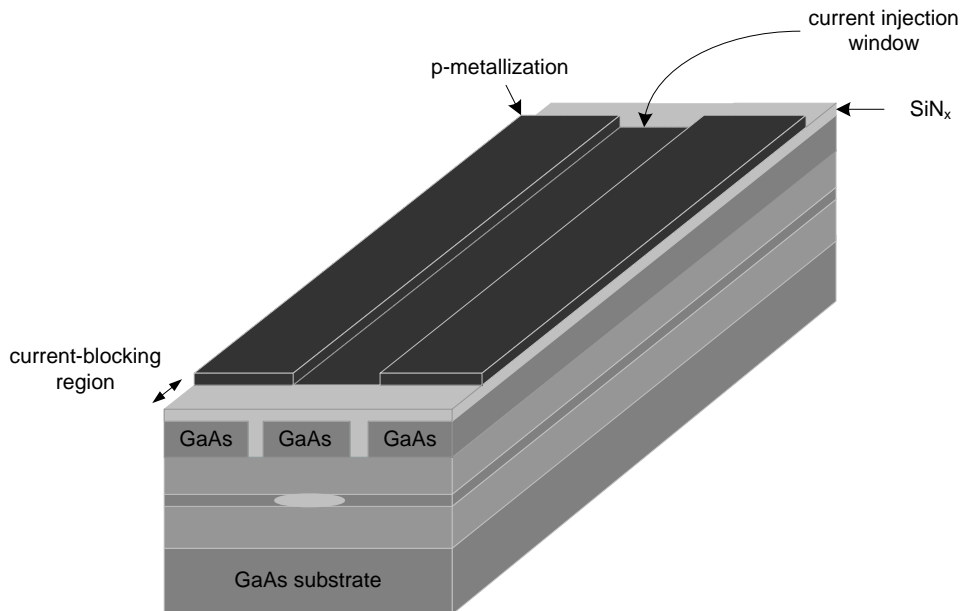
Fig. 6.3.1. High-power BA AlGaInP structure with a current-blocking region.

Figure 6.3.1 (reproduction of Fig. 2.3.2(b)) shows a BA AlGaInP lasers schematic with a pushed-back p-metallization (about $30\,\mu m$) design. The current-blocking region creates a window at the facets regions where no current directly flows (the SiN_x layer also acts as a blocking layer, as it covers the whole facet area). This reduces the nonradiative carrier recombination and T_{FACET}, and improves the COD level. T_{FACET} measurements of InGaAs/AlGaAs 940 nm BA lasers done by [10] showed that T_{FACET} is smaller in lasers with current-blocking design. In AlGaInP 650 nm BA lasers, the cw COD level improved by about 60 % in lasers with current-blocking de-

sign. All the lasers investigated in this study are designed with a current-blocking region.

6.3.2 Non-absorbing mirrors by QWI

Non-absorbing mirrors (NAM) means having a window region near the facet with higher bandgap compared to the rest of the resonator. This way, photon absorption near the facet region can be reduced. Re-growing epitaxial layers having a larger bandgap near the facet is possible [69]-[71], but simpler methods, such as QWI, are easier to implement.

Quantum well intermixing is a process in which atoms from quantum wells and their corresponding barriers interdiffuse, to alter the shape and depth of the quantum well, thus modifying the quantized energy state, as illustrated in Fig. 6.3.2.
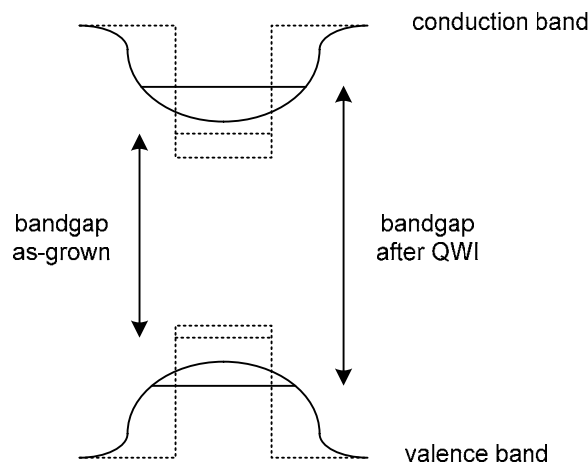
Fig. 6.3.2. Conduction and valence band structure of a QW before (dashed line) and after (solid line) QWI.

The modified quantized energy state is usually observed as a blue-shift of the band edge, that is, an increase in the quantized energy state. There are several techniques used to accomplish QWI [75], such as impurity-induced disordering (IID) [7][8[74], impurity-free vacancy-enhanced disordering (IFVD) [76], photo absorption induced disordering (PAID) [8], and implantation-enhanced interdiffusion [77].

Figure 6.3.3 shows photoluminescence measurements of 633 nm AlGaInP BA lasers, where QWI was performed to create NAM near the facets. A wavelength blue-shift of about 20 nm was observed between the intermixed region near the facets and the rest of the resonator where no intermixing occurred.
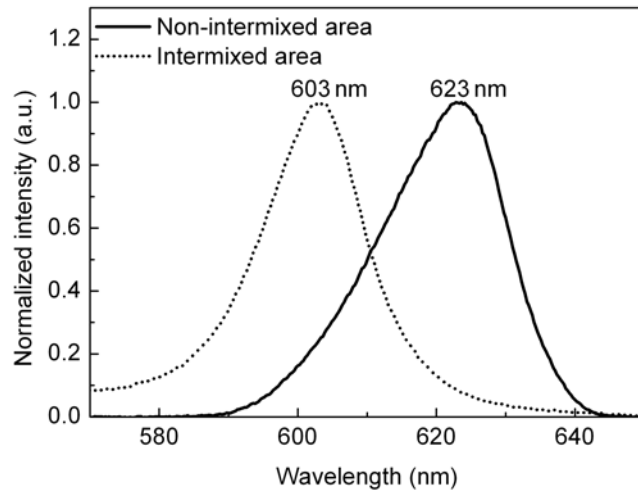
Fig. 6.3.3. Photoluminescence of a 633 nm AlGaInP lasers showing the wavelength blue-shift between the intermixed region near the facets and the non-intermixed rest of the resonator.

A comparison between PI-curves of the test lasers with and without a NAM window design is shown in Fig. 6.3.4. About 35 % improvement was achieved in the COD level, and a small improvement in the threshold current was also obtained.
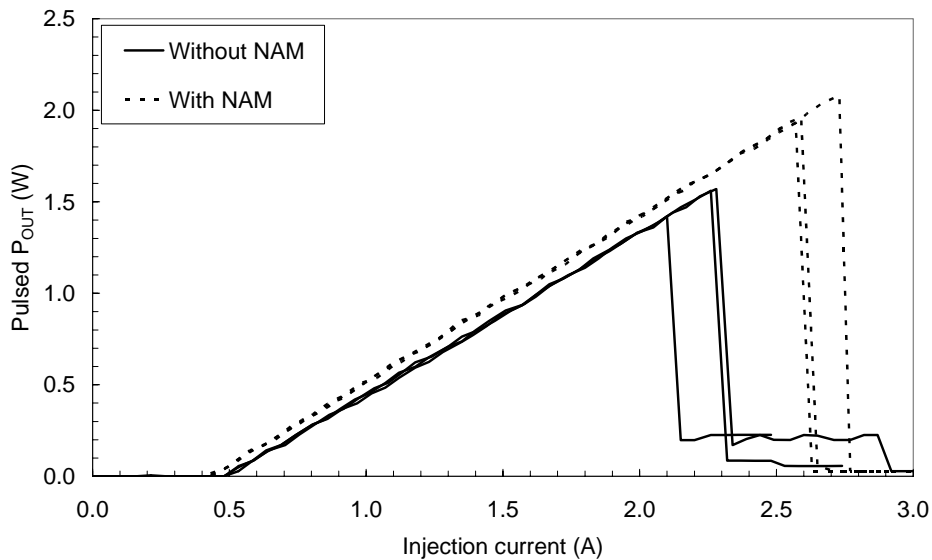
Fig. 6.3.4. PI-curves of 633 nm AlGaInP BA lasers with (dashed line) and without (solid line) non-absorbing mirrors.

Chapter 7

Summary

In this thesis, the catastrophic optical damage (COD) effect in AlGaInP laser diodes was studied. Detailed investigation of the COD induced defects and a complete analysis of its dynamics using an innovative combination of concepts and analytical methods was demonstrated.

Microphotoluminescence (μPL) mapping, focused ion beam (FIB) microscopy, and deep-etching techniques were used to investigate the COD induced defects in Al-GaInP lasers. It was found by μPL mapping that those defects are highly nonradiative, starting from the output facet of the laser and propagating deep inside the cavity. Visible defects due to COD were only rarely identified in the Al_2O_3 anti-reflection coating on the output facet. FIB microscopy analysis demonstrated that the DLDs are composed of complex dislocation networks which are confined to the active region of the laser, containing the QW and partially the waveguide.

Spontaneous breakdown can be explained as a COD level degradation during operation, leading to similar defects on a smaller scale. The COD in special tapered lasers showed that the DLDs follow the direction of the light field, and not a certain crystal direction as it has been explained by some authors. After analyzing an IR emitter, it was found that the behavior of the COD effect in AlGaInP/InGaP lasers is very similar to AlGaAs/InGaAs lasers.

Facet temperature changes during COD were analyzed by means of micro-Raman (μR) spectroscopy and real-time thermal imaging. μR spectroscopy analysis showed that the facet temperature rises linearly with increasing optical output power, and exhibits a sudden drop after the COD event. Temperature profile measurements across the laser stripe of a nondegraded device demonstrated that the facet temperature is

proportional to the near-field intensity (NFI), and that COD occurs at the hot regions arising at the NFI peaks.

Furthermore, imaging the process of COD with a thermal infrared camera revealed the COD temperature dynamics. A pronounced temperature spike occurs in a time less than 2.3 ms duration at the location where the COD is seeded. A subsequent jump in bulk temperature was observed. These findings complemented the analysis performed by μR spectroscopy. The correlation with optical NFI gave evidence for the critical nature of the COD process driven by both the optical load at the facet and the thermal load due to bulk heating. This interplay between temperature and optical power was additionally analyzed by temperature-power analysis, which demonstrated that the COD level decreases linearly with increasing bulk temperature (T_{BULK}) at COD.

As a conclusion, it has been revealed by μR spectroscopy, real-time thermal imaging, and temperature-power analysis, that absorption of stimulated photons at the laser facet is the major source of facet heating, and that a critical facet temperature $T_{FCRIT} = T_{BULK} + const \times NFI$ must be reached in order for COD to occur.

Finally, the influence of design parameters on COD and possible solutions to improve the COD level in AlGaInP lasers were investigated. First, a comparison of different epitaxy and design parameters on COD demonstrated that lasers with a thick waveguide design tend to have a higher COD level compared to thin waveguide design lasers due to their smaller confinement factor. Moreover, it was shown that the COD level increases with increasing wavelength due to the fact that short-wavelengths lasers have shallower QWs, leading to increased carrier leakage and dissipated power, and eventually a lower COD performance. Second, the advantages and disadvantages of lasers with different resonator lengths, and their influence on COD were also analyzed. It was shown that lasers with longer resonators exhibit higher COD levels, however, on the cost of threshold current and slope efficiency. At last, the importance of facet passivation and pre-coating treatment processes and low-absorption facets design techniques for COD level improvement were introduced. Current-blocking near the facet regions reduced the temperature there and improved the COD performance by around 60%. Non-absorbing-mirror devices by QWI led to about 35 % improved COD level because of reduced photon absorption and nonradiative carrier recombination at the laser facets.

Bibliography

[1] M. Ikeda, Y. Mori, H. Sato, K. Kaneko, and N. Watanabe, Appl. Phys. Lett. 47, 1027 (1985)

[2] K. Kobayashi, S. Kawata, A. Gomyo, I. Hino, and T. Suzuki, Electron. Lett. 21, 931 (1985)

[3] S. Andersson-Engels and T. Trebst, BRIGHTER.EU Project e-Newsletter n°3, http://www.ist-brighter.eu (2006)

[4] M. D. Fairchild, "Color appearance modes", 2nd edition, Wiley series in Imaging Science and Technology, ISBN 0-470-01216-1 (2005)

[5] E. Kapon (ed.), "Semiconductor Lasers II, Materials and Structures", Academic Press, ISBN 0-12-397631-6 (1999)

[6] A. Moser and E.-E. Latta, J. Appl. Phys. 71, 4848 (1992)

[7] S. Arimoto, M. Yasuda, A. Shima, K. Kadoiwa, T. Kamizato, H. Watanabe, E. Omura, M. Aiga, K. Ikeda, and S. Mitsui, IEEE J. Quantum Electron. 29, 1874 (1993)

[8] A. McKee, C. McLean, G. Lullo, A. Bryce, R. De La Rue, J. Marsh, and C. Button, IEEE J. Quantum Electron. 33, 45 (1997)

[9] H. Horie, Y. Yamamoto, N. Arai, H. Ohta, IEEE Photon. Tech. Lett. 12, 13 (2000)

[10] F. Rinner, J. Rogg, M. T. Kelemen, M. Mikulla, G. Weimann, J. W. Tomm, E. Thamm, and R. Poprawe, J. Appl. Phys. 93, 1848 (2003)

[11] K. H. Park, J. K. Lee, D. H. Jang, H. S. Cho, C. S. Park, K. E. Pyun, J. Y. Jeong, S. Nahm, and J. Jeong, Appl. Phys. Lett. 73, 2567 (1998)

[12] R. E. Mallard and R. Clayton, Proc. SPIE 3004, 145 (1997)

[13] C. H. Henry, P. M. Petroff, R. A. Logan, and F. R. Meritt, J. Appl. Phys. 50, 3721 (1979)

[14] O. Ueda, K. Wakao, S. Komiya, A. Yamaguchi, S. Isozumi, and I. Umebu, J. Appl. Phys. 58, 3996 (1985)

[15] T. Fukushima, A. Furuya, Y. Kito, H. Sudo, M. Sugano, and T. Tanahashi, Elect. Comm. in Jap. 78, 11 (1995)

[16] G. B. Stringfellow (ed.) and M. G. Craford (ed.), "High-Brightness Light Emitting Diodes", Vol. 48, Academic Press, ISBN 0-12-752156-9 (1997)

[17] H. C. Casey, Jr. and M. B. Panish, "Heterostructure Lasers, Part B, Materials and Operating Characteristics", Academic Press, ISBN 0-12-1631028 (1978)

[18] A. Meney, A. Prins, A. Philips, J. Sly, E. O'Reilly, D. Dunstan, A. Adams, and A. Valster, IEEE J. Quantum Electron. 1, 697 (1995)

[19] K. Streubel, N. Linder, R. Wirth, and A. Jaeger, IEEE J. Quantum Electron 8, 321 (2002)

[20] C. M. Wolfe, N. Holonyak, Jr. and G. E. Stillman, "Physical properties of semiconductors", Prentice-Hall international editions, ISBN 0-13-669961-8 (1989)

[21] R. Diehl (ed.), "High-Power Diode Lasers Fundamentals, Technology, Applications", Springer-Verlag, ISBN 3-540-66693-1 (2000)

[22] C. Geng, "Spontane Mischkristallordnung in AlGaInP Laserstrukturen", Dissertation, University of Stuttgart, ISBN 3-8265-2653-8 (1997)

[23] B. I Miller, U. Koren, M. G. Young, and M. D. Chen, Appl. Phys. Lett. 58, 1952 (1991)

[24] A. Valster, C. J. van der Poel, M. N. Finke, M. J. B. Boermans, Electron. Lett. 28, 145 (1992)

[25] P. S. Zory Jr. (ed.), "Quantum Well Lasers", Academic Press, ISBN 0-12-781890 (1993)

[26] T. Iwamoto, K. Mori, M. Mizuta, and H. Kukimoto, J. Cryst. Growth 68, 27 (1984)

[27] W. W. Chow, K. D. Choquette, M. H. Crawford, K. L. Lear and G. R. Hadley, IEEE J. Quant. Electr. 33, 1810 (1997)

[28] R. Michalzik, "Advanced Optoelectronic Communication Systems", Script, Optoelectronic department, University of Ulm, Germany (2003)

[29] L. A. Coldren and S. W. Corzine, "Diode Lasers and Photonic Integrated circuits", Wiley series in microwave & optical engineering, ISBN 0-471-11875-3 (1995)

[30] K. Ikeda, S. Horiuchi, T. Tanaka, and W. Susaki, IEEE Trans. Electron Dev. ED-24, 1001 (1977)

[31] U. Strauß, W. W. Ruehle, H. H. Queisser, K. Nakano, and A. Ishibashi, J. Appl. Phys. 75, 8204 (1994)

[32] S. Adachi, J. Appl. Phys. 54, 1844 (1983)

[33] G. Hatakoshi, M. Suzuki, N. Motegi, M. Ishikawa, and Y. Uematsu, Transaction Electronics 71, 315 (1988)

[34] M. Fukuda, "Reliability and Degradation of Semiconductor Lasers and LEDs", Artech House, ISBN 0-89006-465-2 (1991)

[35] L. A. Johnson, "Laser Diode Burn-in and Reliability Testing", http://www.ilxlightwave.com

[36] F. R. Nash, "Estimating Device Reliability: Assessment of Credibility", Kluver Academic Publishers, ISBN 0-7923-9304-X (1993)

[37] P. Altieri-Weimar, "Efficiency and Reliability of AlGaInP LEDs", Dissertation, University of Ulm, Germany (2005)

[38] M. Okayasu and M. Fukuda, J. Appl. Phys. 72, 2119 (1992)

[39] A. Moser, E.-E. Latta, and D. J. Webb, Appl. Phys. Lett. 55, 1152 (1989)

[40] O. Ueda, Mat. Res. Soc. Symp. Proc. 184, 125 (1990)

[41] S. J. Sweeney, L. J. Lyons, and Lock D.A, IEEE J. Quantum Electron. 9, 1325 (2003)

[42] O. Ueda, "Reliability and Degradation of III-V Optical Devices", Artech house, ISBN 0-89006-652-3 (1996)

[43] C. W. Snyder, J. W. Lee, R. Hull, and R. A. Logan, Appl. Phys. Lett. 67, 488 (1995)

[44] F. Kappeler, K. Mettler, and K.-H. Zschauer, IEE Proc. 129, 256 (1982)

[45] H. Fujii, Y. Ueno, and K. Endo, Appl. Phys. Lett. 62, 17 (1993)

[46] S. Bull, J. W. Tomm, and E. Larkins, J. Mater. Sci.: Mater. Electron., DOI 10.1007/s10854-008-9577-5 (2008)

[47] M. J. Pelletier (ed.), "Analytical applications of Raman spectroscopy", Blackwell Science, ISBN 0-632-05305-4 (1999)

[48] H. Brugger and P. W. Epperlein, Appl. Phys. Lett. 56, 11 (1990)

[49] P. W. Epperlein, Appl. Phys. Lett. 60, 6 (1992)

[50] T. Q. Tien, F. Weik, J. W. Tomm, B. Sumpf, M. Zorn, U. Zeimer, and G. Erbert, Appl. Phys. Lett. 89, 181112 (2006)

[51] J. Jiménez, "Microprobe Characterization of Optoelectronic Materials (Opto-electronic properties of semiconductors and superlattices)", Taylor & Francis, ISBN 1-56032-941-6 (2002)

[52] R. Loudon, Adv. Phys. 13, 423 (1964)

[53] J. G. Grasselli and B. J. Bulkin (ed.), "Analytical Raman Spectroscopy", John Wiley and Sons, Inc., ISBN 0-471-51955-3 (1991)

[54] Asahi et al., J. Appl. Phys. 65, 5007 (1989)

[55] J. R. Marciante and P. Govind, IEEE Photon. Tech. Lett. 10, 54 (1998)

[56] C. H. Henry, IEEE J. Quantum Electron. 18, 259 (1982)

[57] G. C. Dente , IEEE J. Quantum Electron. 37, 1650 (2001)

[58] J. R. Marciante and G. P. Agrawal, IEEE J. Quantum Electron.32, 590 (1996)

[59] M. T. Kelemen, Fraunhofer Institut für Angewandte Festkörperphysik (IAF), Freiburg, Germany. Presentation at OSRAM Opto Semiconductor (2005)

[60] P. W. Epperlein, Jpn. J. Appl. Phys. 32, 5514 (1993)

[61] S. D. McDougall, O. P. Kowalski, C. J. Hamilton, F. Camacho, B. Qiu, M. Ke, R. M. De La Rue, and J. H. Marsh, IEEE J. Select. Top. Quantum Electron. 4, 636 (1998)

[62] C. J. Hamilton, O. P. Kowalski, K. McIlvaney, A. C. Bryce, J. H. Marsh and C. C. Button, Electron. Lett. 34, 665 (1998)

[63] R. W. Lambert, T. Ayling, A. F. Hendry, J. M. Carson, D. A. Barrow, S. McHendry, C. J. Scott, A. McKee, and W. Meredith, J. Lightwave Tech. 24, 956 (2006)

[64] S. K. Ghandhi, P. Kwan, K. N. Bhat, and J. M. Borrego, IEEE Electron Device Lett. 3, 48 (1982)

[65] C. Silfvenius, P. Blixt, C. Linström, and A. Feitisch, Laser Focus World 39, 69 (2003)

[66] S. Kamiyama, Y. Mori, Y. Takahashi, and K. Ohnaka, Appl. Phys. Lett. 58, 23 (1991)

[67] G. Beister, J. Maege, D. Gutsche, G. Erbert, J. Sebastian, K. Vogel, M. Weyers, and J. Würfl, Appl. Phys. Lett. 68, 18 (1996)

[68] P. Ressel and G. Erbert, "Verfahren zur Passivierung der Spiegelflächen von Optischen Halbleiterbauelementen", German patent DE 10221952 (2003)

[69] H. Naito, M. Kume, k. Hamada, H. Shimizu, and G. Kano, IEEE J. Quantum Electron. 25, 1495 (1989)

[70] M. Sagawa, K. Hiramoto, T. Toyonaka, K. Shinoda, and K. Uomi, Electron. Lett. 30, 1410 (1994)

[71] R. M. Lammert, M. L. Osowski, S. W. Oh, C. Panja, and J. E. Ungar, Electron. Lett. 42, 535 (2006)

[72] P. Yeh, "Optical Waves in Layered Media", John Wiley & Sons Inc., ISBN 0-471-82866-1 (1988)

[73] N. Chand and R. A. Hamm, "In-situ technique for cleaving crystals", United States Patent 5773318 (1998)

[74] N. Holonyak, Jr., IEEE J. Sel. Topics in Quantum Electron. 4, 584 (1998)

[75] E. J. Skogen, "Quantum Well Intermixing for Wavelength-Agile Photonic Integrated Circuits", Dissertation, University of California Santa Barbara, USA (2003)

[76] S. K. Si, D, H. Yeo, K. H. Yoon, and S. J. Kim, IEEE J. Sel. Topics in Quantum Electron. 4, 619 (1998)

[77] S. Charbonneau, E. Kotels, P. Poole, J. He, G. Aers, J. Haysom, M. Buchanan, Y. Feng, A. Delage, F. Yang, M. Davies, R. Goldberg, P. Piva, and I. Mitchell, IEEE J. Sel. Topics in Quantum Electron. 4, 772 (1998)

Marwan BOU SANAYEH

Date of Birth: 30 October 1978
Nationality: Lebanese

EDUCATION

June 2005-August 2008 **Doctor of Engineering (Dr.-Ing.)**
University of Duisburg-Essen, Duisburg, Germany
OSRAM Opto Semiconductors GmbH, Regensburg,
Germany

April 2002-January 2005 **Master of Science in Communications Technology**
Ulm University, Ulm, Germany

October 1996-August 2001 **Bachelor of Engineering in Electrical Engineering**
Notre Dame University, Zouk Mosbeh, Lebanon

EXPERIENCE

June 2005-July 2008 **R&D Engineer (including PhD thesis)**
OSRAM Opto Semiconductors GmbH, Regensburg,
Germany
Research in AlGaInP high-power laser diodes
including reliability and failure modes analy-
ses, and quantum well intermixing. Co-worker
in the European Projects BRIGHT.EU and
BRIGHTER.EU.

October 2003-May 2005 **Student Research Assistant (including MSc. thesis)**
Optoelectronics dept., Ulm University, Ulm,
Germany
Processing and characterization of 2-D flip-
chip bonded vertical cavity surface emitting
laser (VCSEL) arrays with built-in functional
redundancy for high-speed data communica-
tion. Work includes clean-room experience.

July 2002-February 2005 **Telecommunications Testing Engineer**
LogicaCMG GmbH & Co. KG, Ulm, Germany
Testing and debugging Nokia mobile phones
software. Creation of testcases, test execution
reports, and software error documentation.

PUBLICATIONS

M. Bou Sanayeh, P. Brick, W. Schmid, B. Mayer, M. Müller, M. Reufer, K. Streubel, M. Ziegler, J. W. Tomm, and G. Bacher, *"The physics of catastrophic optical damage in high-power AlGaInP laser diodes"*, Proc. SPIE 6997, 699703 (2008)

M. Ziegler, J. W. Tomm, T. Elsaesser, C. Matthiesen, **M. Bou Sanayeh**, and P. Brick, *"Real-time thermal imaging of catastrophic optical damage in red-emitting high-power diode lasers"*, Appl. Phys. Lett. 92, 103514 (2008)

M. Bou Sanayeh, P. Brick, B. Mayer, M. Müller, M. Reufer, W. Schmid, K. Streubel, S. Schwirzke-Schaaf, J.W. Tomm, A. Danilewsky, and G. Bacher, *"Defect investigation and temperature analysis of high-power AlGaInP laser diodes during catastrophic optical damage"*, J. Mater. Sci.: Mater. Electron., DOI 10.1007/s10854-007-9478-z (2007)

M. Bou Sanayeh, P. Brick, W. Schmid, B. Mayer, M. Müller, M. Reufer, K. Streubel, J. W. Tomm, and G. Bacher, *"Temperature-power dependence of catastrophic optical damage in AlGaInP laser diodes"*, Appl. Phys. Lett. 91, 041115 (2007)

M. Bou Sanayeh, A. Jaeger, W. Schmid, S. Tautz, P. Brick, K. Streubel, and G. Bacher, *"Investigation of dark line defects induced by catastrophic optical damage in broad-area AlGaInP laser diodes"*, Appl. Phys. Lett. 89, 101111 (2006)

CONFERENCES

M. Ziegler, J. W. Tomm, T. Elsaesser, C. Matthiesen, **M. Bou Sanayeh**, and P. Brick, *"Catastrophic Optical Damage in High-Power Diode Lasers Monitored by Real-Time Imaging"*, Poster, CLEO/QELS, San Jose, CA, USA, May 2008

M. Bou Sanayeh, P. Brick, W. Schmid, B. Mayer, M. Müller, M. Reufer, K. Streubel, M. Ziegler, J. W. Tomm, and G. Bacher, *"The physics of catastrophic optical damage in high-power AlGaInP laser diodes"*, Talk, SPIE Europe Photonics Europe, Strasbourg, France, April 2008

M. Bou Sanayeh, P. Brick, B. Mayer, M. Müller, M. Reufer, W. Schmid, M. Ziegler, J. W. Tomm, and G. Bacher, *"Influence of low-absorption laser facets on catastrophic optical damage in AlGaInP lasers"*, Talk, German Physical Society Spring Conference (DPG-Tagung), Berlin, Germany, February 2008

M. Bou Sanayeh, P. Brick, B. Mayer, M. Müller, M. Reufer, W. Schmid, K. Streubel, S. Schwirzke-Schaaf, J.W. Tomm, A. Danilewsky, and G. Bacher, *"Defect investigation and temperature analysis of high-power AlGaInP laser diodes during catastrophic optical damage"*, Talk**,** 12th Int. Conf. on Defects-Recognition, Imaging and Physics in Semiconductors (DRIP-XII), Berlin, Germany, September 2007

M. Bou Sanayeh, P. Brick, W. Schmid, B. Mayer, M. Müller, M. Reufer, K. Streubel, J. W. Tomm, and G. Bacher, *"Micro-Raman investigation of facet temperature during catastrophic optical damage in AlGaInP laser diodes"*, Talk, German Physical Society Spring Conference (DPG-Tagung), Regensburg, Germany, March 2007

M. Bou Sanayeh, A. Jaeger, W. Schmid, S. Tautz, P. Brick, K. Streubel, and G. Bacher, *"Study of dark line defects caused by catastrophic optical mirror damage in broad-area red-emitting high-power AlGaInP lasers"*, Talk, German Physical Society Spring Conference (DPG-Tagung), Dresden, Germany, March 2006

FURTHER PUBLICATIONS AND CONFERENCES

M. Ziegler, R. Pomraenke, M. Felger, J. W. Tomm, P. Vasa, C. Lienau, **M. Bou Sanayeh**, A. Gomez-Iglesias, M. Reufer, F. Bugge, and G. Erbert, *"Infrared emission from the substrate of GaAs-based semiconductor lasers"*, Appl. Phys. Lett. 93, 041101 (2008)

R. Bohdan, A. Bercha, W. Trzeciakowski, F. Dybała, and B. Piechal, **M. Bou Sanayeh**, M. Reufer and P. Brick, *"Yellow AlGaInP/InGaP laser diodes achieved by pressure and temperature tuning"*, J. Appl. Phys., to be published

J. M. G. Tijero, H. Odriozola, I. Esquivias, A. Martín-Mínguez, P. Brick, M. Reufer, **M. Bou Sanayeh**, A. Gomez-Iglesias, and N. Linder, *"Self-Consistent Modeling of Edge-Emitting GaInP/AlGaInP Red Lasers"*, Talk, 8th Int. Conf. on Numerical Simulation of Optoelectronic Devices (NUSOD '08), Nottingham, UK, September 2008

H. Roscher, **M. Bou Sanayeh**, S. B. Thapa, and R. Michalzik, *"VCSEL arrays with redundant pixel designs for 10 Gbit/s 2-D space-parallel multimode fiber transmission"*, Proc. ECOC 3, 687 (2005)

H. Roscher, **M. Bou Sanayeh**, S. B. Thapa, and R. Michalzik, *"VCSEL arrays with redundant pixel designs for 10 Gbit/s 2-D space-parallel multimode fiber transmission"*, Poster, 31st European Conference on Optical Communication (ECOC 2005), Glasgow, Scotland, UK, September 2005